UNIVERSITY OF CALIFORNIA,
IRVINE

# Electrostatic Interactions in Heterobimetallic Complexes and their Effect on Reduction Potentials, Electronic Structure, and Reactivity

DISSERTATION

submitted in partial satisfaction of the requirements
for the degree of

DOCTOR OF PHILOSOPHY

in Chemistry

by

Alexander H. Reath

Dissertation Committee:
Associate Professor Jenny Y. Yang, Chair
Professor A.S. Borovik
Distinguished Professor William J. Evans

2019

# DEDICATION

For my Family: Cassie, Mom, Dad, Sandy, Joe, Janey, Robin, Joey, and Luke

# TABLE OF CONTENTS

# LIST OF FIGURES

# LIST OF TABLES

# LIST OF SCHEMES

# ACKNOWLEDGMENTS

The work presented in this dissertation represents five years of my life, and is a witness to the struggles, achievements, and sacrifices that came with it. As proud as I am of what I have accomplished during this time, I owe all of this moment to the incredible people who have been with me along the way. Anybody who has had the privilege of pursuing doctoral research knows that it would not be possible without the mentorship and support of others, and quite frankly my entire support network would probably agree. To all of my friends, family, colleagues, and mentors: pat yourself on the back.

I would like to express my most sincere gratitude towards my PI, Jenny Yang, who gave me an incredible opportunity five years ago by welcoming me into her group. As I have grown under your guidance, you have somehow managed to simultaneously complete the tenure process, start a family, and cultivate an amazing research program. Your mentorship extends beyond the lab and is an inspiration to the next chapter of my life.

I would also like to thank my committee members, Professor Andy Borovik and Professor Bill Evans, who have always had an open door and provided a great deal of guidance over the years.

I have had the chance to work with so many talented colleagues in the Yang Lab over the past five years (Charlene, Annie, Steven, Juliet, Brian, Zach, Bianca, Drew, Caitlin, Jeff, Sarah, Tyler, Allie, Ian, Megan, and many more). I would specifically like to thank Kevin Kang, who has been a tremendous team member over the years. I am so thankful to have had the chance to work, learn, and share memories with all of you. As a formal submission to the UC Libraries Archives, I would like to use this platform to officially state that the Hollywood sign is, in fact, visible from Reines Hall.

Thank you to all of my friends, Bryan, Eric, Leslie, Mack, Kyle, Stan, Torin, Susy, and many more. Some of my best memories from the past five years are shared with all of you, from Palo Verde to Black Mountain to the Inglewood Forum. As bittersweet as it is to say goodbye, I know we will be in touch.

Kato, thank you for being a good boy.

Without a doubt, the hardest part of graduate school has been the time that I have missed with my family, but becoming a member of a new one has certainly been the best. To the Reaths and the Verbouts (Mom, Dad, Sandy, Joe, Grandpa, Grandma, Grand, Boomer, Janey, Robin, Joey, Luke, and beyond), I love you all and am so grateful to have had the love and support from all of you throughout my life. I am looking forward to making up for the memories I have missed.

Above all, there is one person that deserves to be singled out for the selflessness that they have shown over the past five years. Cassie, I can't begin to thank you enough for the sacrifices that you have made for me and the love that you have shown throughout this experience. You left everything behind to follow me to California, and have continued to show me every day how lucky I am to have you in my life. This has been a long, difficult journey for both of us, but we have made it here together. As this chapter closes and we move on to the next, I want to take a moment to appreciate the amazing memories we have made building our lives together over the past few years. I love you so much and can't wait to see where life takes us next.

# CURRICULUM VITAE

**Alexander H. Reath**

## EDUCATION

**University of California, Irvine**
**2019**
*Doctor of Philosophy*, Chemistry
**University of Minnesota, Twin Cities**
**2014**
*Bachelor of Science,* Chemistry

## RESEARCH EXPERIENCE

**Graduate Student Researcher**, University of California, Irvine **2014-2019**
Advisor: Prof. Jenny Y. Yang
Research Project: Heterobimetallic Complexes with Incorporated Redox Inactive Cations

**Undergraduate Student Researcher**, University of Minnesota, Twin Cities **2013-2014**
Advisor: Prof. Ian A. Tonks
Research Project: Transition Metal Complexes Featuring Metal-Metal Bonds for Multielectron Redox Catalysis

## PEER REVIEWED PUBLICATIONS

1. **Reath, A. H.**; Ziller, J. W.; Tsay, C.; Ryan, A. J.; Yang, J. Y. Redox Potential and Electronic Structure Effects of Proximal Nonredox Active Cations in Cobalt Schiff Base Complexes *Inorg. Chem.* **2017**, *56*, 3713.
2. Chantarojsiri, T.; **Reath, A. H.**; Yang, J. Y. Cationic Charges Leading to an Inverse Free-Energy Relationship for N−N Bond Formation by $Mn^{VI}$ Nitrides *Angewandte Chemie International Edition* **2018**, *57*, 14037.
3. Dunn, P. L.; **Reath, A. H.**; Clouston, L. J.; Young, V. G.; Tonks, I. A. Homo- and heteroleptic group 4 2-(diphenylphosphino)pyrrolide complexes: Synthesis, coordination chemistry and solution state dynamics *Polyhedron* **2014**, *84*, 111.

## LEADERSHIP AND OUTREACH

- Founding member and leader (2018) of the UCI Graduate Safety Team. Assisted in organizational development, securing an annual budget, and establishing partnerships within the Chemistry Department. Responsibilities as team leader included management of a team of six members to execute policies related to compliance, public relations, and educational outreach.
- Served as UCI Graduate Safety Fellow (2017-2018), fulfilling roles of technical consultation to the Department of Environmental Health and Safety, promotion of safety culture, and assistance in undergraduate safety training. Represented UCI at a

national conference on research safety, and completed coursework for UC-EH&S Professional Certification.
- Five years of participation in the LEAPS outreach program, promoting scientific research to middle school students.

**AWARDS**

- **Graduate Award for Departmental Service (2018):** Recognized for significant contributions to the safety culture of the University of California, Irvine Chemistry Department and leadership in the Graduate Safety Team.
- **Graduate Safety Fellowship (2017):** Awarded funding (1 year) for appointment to gain formal experience in research safety.
- **Undergraduate Research Opportunities Fellowship (2014):** Awarded stipend and materials funding for on semester of research.

**TEACHING EXPERIENCE**

- **CHEM 1LC:** Laboratory Teaching Assistant (Spring 2017, Summer 2018, Fall 2018)
- **CHEM 1LD:** Laboratory Teaching Assistant (Fall 2014)
- **CHEM 51LB:** Laboratory Teaching Assistant (Winter 2015)
- **CHEM 51LC:** Laboratory Teaching Assistant (Spring 2017)
- **CHEM 107L:** Laboratory Teaching Assistant (Winter 2017, Winter 2019)
- **CHEM 107L:** Head Teaching Assistant (Spring 2019)
- **CHEM 127:** Lecture Course Teaching Assistant (Winter 2016)

# ABSTRACT OF THE DISSERTATION

Electrostatic Interactions in Heterobimetallic Complexes and their Effect on Reduction Potentials, Electronic Structure, and Reactivity

By

Alexander H. Reath

Doctor of Philosophy in Chemistry

University of California, Irvine, 2019

Professor Jenny Y. Yang, Chair

The use of electrostatic interactions is a fundamental component of the the structure and function of biological enzymes, and has the potential to be a powerful tool in synthetic complexes as well. Electric fields generated by charged species have remarkable influence over electronic structure and intermolecular reactivity, and are capable of remarkable thermodynamic control in catalysis. Herein, a heterobimetallic platform consisting of a Schiff base binding site and an enchained crown ether ring is used to show a diverse range of effects that arise when a transition metal and a cation are placed in close proximity.

In Chapter 1, spectroscopic and electrochemical techniques are used to demonstrate the role of electrostatic interactions on a nearby cobalt center. These experiments demonstrate the use of a wide range of cationic metals to impart significant shifts on the reduction potentials of a proximal transition metal center. Additionally, the role of solvent and anion coordination in the screening of electrostatic interactions are established.

In Chapter 2, further studies are conducted with a nickel analogue of this heterobimetallic framework. Theoretical calculations are used to demonstrate the effect of electrostatics on the expanded molecular orbital manifold of metal Schiff base systems.

In Chapter 3, a manganese complex is used to demonstrate the role of electrostatic interactions on reactivity. Extensive studies are carried out on the kinetic and thermodynamic considerations for the N-N coupling of Mn(V) nitrides, which showed that cationic charge is capable of stabilizing activated nitride species against bimolecular reactivity. The effect of proximal cations on ammonia oxidation and p$K_a$ are also explored.

# INTRODUCTION

## 0.1 Electrostatic Interactions in Enzymes

The ability of enzymes to efficiently undergo difficult chemical transformations is a remarkable natural phenomenon, and understanding how these biological catalysts function is a crucial step towards harnessing their reactivity. It is becoming increasingly accepted that the role of electrostatic interactions is a predominant feature in the structure and function of enzymatic processes.[1-3] The complex electrostatic architecture of enzymes is intricately designed to use solvent interactions,[4-10] hydrogen bonding networks,[11-15] and Lewis acidic metals[16-18] that stabilize transition states and gently guide catalysis by avoiding high and low energy intermediates. Instances where the reactivity can be shut on and off by the presence or absence of electrostatic elements demonstrates the influence of these forces in governing the thermodynamics of enzymatic activity.[16-17, 19-20] The universality of electrostatic interactions in the function of enzymes offers an opportunity for further scientific study, and could provide important insights into the design of synthetic complexes.

The $Mn_4CaO_5$ cluster in the oxygen-evolving complex (OEC) of the photosystem II enzyme (PSII) is widely known for its role in biological water oxidation. The discovery of the $Mn_4CaO_5$ core of the active site by X-ray crystallography[21-22] has led to many studies investigating the role of this ion in the enzyme's activity. Several functions of $Ca^{2+}$ have been proposed, including facilitation of electron tranfer,[23-24] promotion of substrate binding,[25] and structural modification of the cubane active site.[26] Studies in which $Ca^{2+}$ is

replaced with other metal ions have shown that only $Sr^{2+}$ is able to approach similar activity.[27-29] The development of synthetic manganese oxido cubane complexes by Agapie that closely mimicked the active site of PSII allowed for more detailed studies into the structure function relationship, which led to the discovery that substitution of $Sr^{2+}$ results in an identical reduction potential of the cluster when compared to $Ca^{2+}$.[30-31] Other metals led to significant changes in reduction potential, a possible indication of the importance of redox mediation by the presence of the appropriate ion. Findings by Borovik showed that $Ca^{2+}$ and $Sr^{2+}$ metal ions in heterobimetallic manganese complexes greatly assisted in the facilitation of electron transfer in the reduction of dioxygen.[32-33] The modulation of reduction potentials was again attributed as an important role of these ions, and the authors

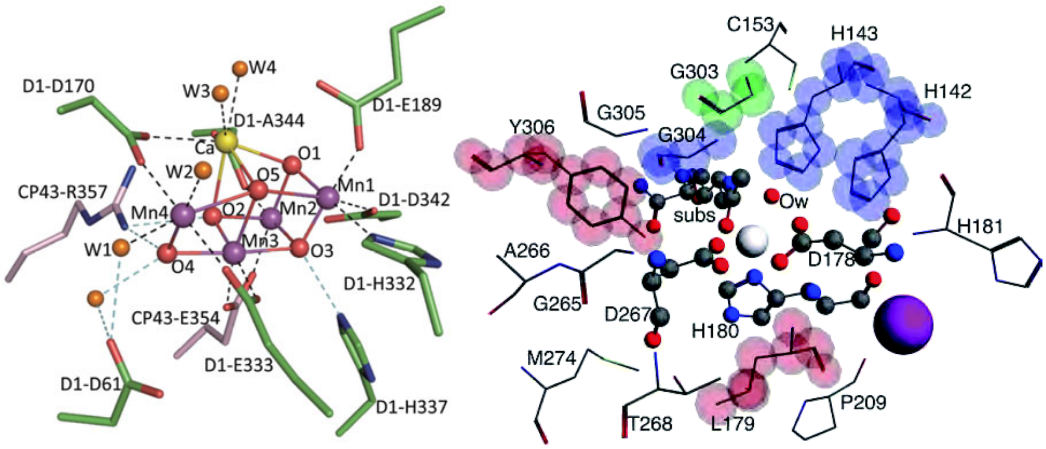


**Figure 0.1 Left:** $Mn_4CaO_5$ cluster and its ligand environment, with Manganese (purple spheres), calcium (yellow sphere), oxygen (red spheres), oxygen (orange spheres), and surrounding residues; Reproduced from ref. 22 with permission from Springer Nature. **Right:** The 3–7 Å size model systems for HDAC8 from nuclear configuration 2, with zinc (white sphere); potassium (purple sphere), oxygen (red spheres), nitrogen (blue spheres), substrate (subs), and surrounding residues. Reproduced from ref. 37 with permission from the Royal Society of Chemistry.

also highlighted the observation that Lewis acidity alone did not account for the behavior of these complexes.

A noteworthy case study in the importance of electrostatic interactions in enzymatic activity is in the role of potassium in the activation and inhibition of reactivity in Histone Deacetylase 8 (HDAC8), which plays an important role in post-translational modification during the biosynthesis of proteins.[34] The zinc active site of this enzyme incorporates a bound water molecule that acts as a nucleophile to facilitate amide bond cleavage with its target substrate.[19-20] Crystallographic studies revealed the presence of $K^+$ at a distal metal binding site at a distance of 7 Å from $Zn^{2+}$.[35-36] Simulated studies showed that $K^+$ has a crucial role in substrate binding and transition state stabilization during several mechanistic steps, and the absence of the cation resulted in deactivation of the enzyme.[20] The remote location of $K^+$ precludes its direct interaction with substrate or the $Zn^{2+}$ active site, which poses the question of how exactly this ion participates in the catalytic cycle. Quantitative mapping of the electrostatic potential around the active site revealed that the location of the $K^+$ cofactor is precisely placed to provide the necessary charge density for substrate binding and electron transfer to occur.[37] These findings provide evidence for the careful consideration of electrostatic preorganization in the evolution of protein architecture.

**0.2 Electric Fields Directing Chemical Reactivity**

There are a wide number of possible applications of electrostatic interactions towards chemical reactivity, and their powerful potential as a synthetic tool is becoming increasingly recognized.[38-39] The use of electrostatic fields to direct substrate binding,

stabilize transition states, and activate chemical bonds would vast implications in synthetic chemistry, but historically very few examples exist outside of theoretical discussion.[38] However, the past decade has seen a renaissance in this field, and electrostatic interactions have been utilized for a diverse range of purposes.

The generation of electrostatic fields on surfaces has led to a number of interesting findings in recent years. Charged electrode surfaces can produce large electrostatic fields in the double layer without participating in faradaic processes, which has been used to increase chemoselectivity of surface-bound Rh porphyrin catalysts.[40] Nanostructured gold and palladium electrodes are able to concentrate alkali cations in the double layer during electrocatalysis, leading to major enhancements in $CO_2$ reduction.[41] Electric fields in zeolite nanopores[6] can be produced either by the application of a potential or incorporation of charged species, leading to positive effects on reactivity such as the stabilization of high energy intermediates[42] and increases in product selectivity.[43] A number of studies using STM tips has shown that oriented external electrostatic fields can be used to initiate chemical reactions,[44] such as the isomerization of azobenzene[45] and alkoxyamine cleavage.[46] A fascinating example of recent work in this area demonstrated the acceleration of single molecule Diels Alder reactions by directing electron transfer from the dienophile to the diene with electric fields,[47] providing experimental confirmation of previous theoretical predictions.[48] These results highlight a powerful application of electrostatic fields in chemical reactivity: that field alignment with the direction of charge movement in a transition state can lower the barrier to electron transfer.

The emergence of electrostatic interactions in molecular reactivity has also proved their utility as a means of promoting desirable outcomes in synthesis and catalysis and have been applied to widely known transformations such as palladium cross coupling,[49] Wittig rearrangement,[50] and Friedel-Crafts hydroxyacylation.[51] One of the most established uses of electrostatics is in the promotion of stereoselectivity.[50-61] Molecules containing a net dipole will respond to an electric field by aligning in the same direction, and the installation of charged functional groups or metal ions can impart internal fields to exploit this phenomenon. This effect is particularly applicable to fluorine chemistry in pharmaceutical development, where enantioselectivity is vital to the activity of bioactive molecules. The polarity of C–F bonds are highly polarized, and the use of electrostatic interactions to promote enantioselectivity has been demonstrated by Hoveyda[55] and Rovis.[57, 62] Various uses of electrostatic functionalities have been employed in transition metal catalysis as well.[49, 61, 63-64] Smith has demonstrated the use of weak interactions between bipyridine ligands and substrate to direct regioselectivity in the ortho-borylation of phenols.[61] Similar regioselectivity has been shown by Kanan in gold-catalyzed hydroarylations, this time through the use of strong ion pairing rather than substrate or catalyst functionalities.[64]

### 0.3 Crown Ether Appended Bimetallic Complexes

The synthesis and development of crown ethers and similar macrocycles for metal ion chelation is a rich field of chemistry, and a vast number of variations of these compounds have been reported.[65-66] Naturally, inorganic chemists have been inspired by these

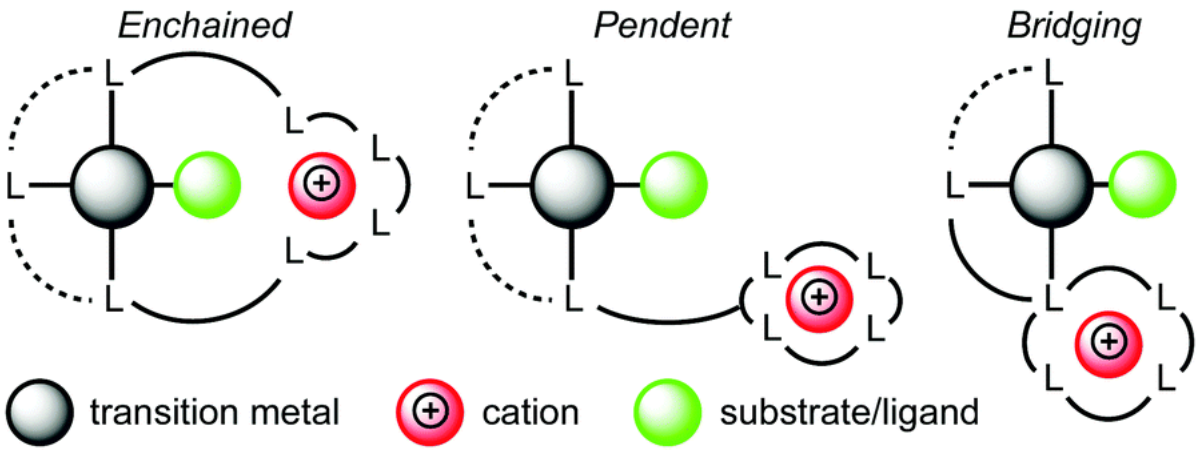


**Figure 0.2:** Schematic representation of different metalla-crown ether designs; Reproduced from ref. 67 with permission from the Royal Society of Chemistry.

compounds to develop transition metal ligand frameworks with incorporated macrocyclic functionalities to house metal cations. A review by Miller classifies these bimetallic complexes into three groups: enchained, pendant, and bridging (Figure 0.2).[67] Enchained crown complexes[68-79] feature binding sites for both the transition metal and the cation within the same macrocycle, often within close proximity. Tethered complexes[80-85] feature crown ether groups appended to the framework by a linkage and tend to be highly flexible. In the bridging class of compounds,[86-91] a donor atom is shared between the transition metal and cation encapsulated by the crown ether. The installation of crown ethers and similar macrocycles has been applied to a diverse range of transition metal ligands, including porphyrins,[92-96] salens,[97-100] pincers,[88, 101-103] and bipyridines.[104-109] The utility of crown ether functionalities has been demonstrated in a number of ways. Lewis acid-assisted activation, in which cooperative binding occurs between the encapsulated cation and a transition metal, has been shown to increase reactivity towards polarized substrates such as

carbonyl[67-68] and acyl groups.[68-69, 80, 85] Cation-substrate interactions have also been used to direct substrates towards transition metals to increase selectivity, demonstrated by Ito in the allylation of carbanions and β-diketones.[110-111] A particularly creative approach to crown ether utility has been pioneered by Miller by using substoichiometric equivalents of cations to induce hemilability of transition metal donor atoms in bridging bimetallic complexes.[88, 112-113] These interactions have been shown to tune the thermodynamic stability of catalytic intermediates by introducing competitive binding of the crown ether ring. Occasional examples of the use of crown ethers to shift reduction potentials of transition metals have been observed historically,[114-115] but this methodology is becoming more popular in recent years.[103, 116] The use of macrocyclic crown ethers in metal complexes is not limited to the selected cases described here; other applications include conformational control[117] of ligand binding and modification of solubility properties[77]

### 0.4 Research Goals

The research described in this dissertation is an investigation into the nature of electrostatic interactions in inorganic complexes, and aims to understand how transition metal electronics and fundamental reactivity are affected by the presence of a proximal cation. The complexes used in these studies share a common framework, an enchained heterobimetallic salen-type ligand (salen = *N,N*-bis(salicylidene)ethylenediamine) with an enclosed crown ether substituent analogous to 18-crown-6 (Scheme 0.1). The synthesis of this ligand scaffold was developed previously by Reinhoudt, whose work focused primarily on structural studies and the incorporation of neutral hosts with nickel complexes.[70-71, 100]

Although a few examples of electrochemical and spectroscopic characterization are shown in this previous work, an in-depth analysis of these complexes, particularly with an expanded scope of metals, provided an opportunity for further study.

Of particular interest was the application of proximal cations as a means of tuning the reduction potential of transition metal ions. The ability to adjust the reduction potential of a transition metal is an important synthetic handle in the design of catalysts, especially in the field of electrocatalysis. Typically, reduction potentials are modulated by appending electron-donating or -withdrawing groups onto a ligand. Disadvantages to this approach include the addition of steric bulk, solubility changes, and undesirable changes to the ligand field of a transition metal. The use of electrostatics offers an alternative method to control reduction potentials that can avoid or significantly diminish these side-effects. In the few previous observations of reduction potential shifts using cations (outlined in **0.1** and **0.2**) have primarily focused on Lewis acidity, i.e. electronic modification through chemical

**Scheme 0.1:**

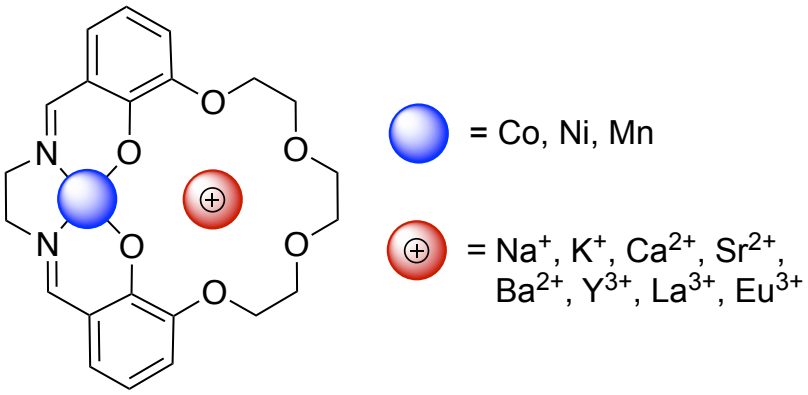

bonds. The consideration of electrostatic interactions provides a broader context for cation effects on transition metal contexts that provides new insight into this type of modification.

By better understanding the nature of electrostatic interactions on a transition metal, this knowledge can then be applied towards reactivity of metal salens. These complexes are well studied and offer a rich platform for reactivity studies;[118] examples included in this work are, C-H oxidation, dioxygen binding and reduction, and nitride activation and protonation. The motivation for studying cation-promoted electrostatic effects on the reactivity of salen compounds is to provide a powerful means of altering their reactivity with the hopes of inspiring further applications of this methodology in the fields of inorganic chemistry, electrocatalysis, and chemical synthesis.

Characterization of the described complexes was carried out using UV-Vis spectroscopy, infrared spectroscopy, mass spectrometry, nuclear magnetic resonance spectroscopy, elemental analysis, X-ray diffractometry, and electroanalytical methods.

## 0.5 References


1. Warshel, A., *Journal of Biological Chemistry* **1998,** *273* (42), 27035-27038.

2. Warshel, A.; Sharma, P. K.; Kato, M.; Xiang, Y.; Liu, H.; Olsson, M. H. M., *Chem. Rev.* **2006,** *106* (8), 3210-3235.

3. Isaksen, G. V.; Hopmann, K. H.; Åqvist, J.; Brandsdal, B. O., *Biochem.* **2016,** *55* (14), 2153-2162.

4. Štrajbl, M.; Shurki, A.; Kato, M.; Warshel, A., *J. Am. Chem. Soc.* **2003,** *125* (34), 10228-10237.

5. Fuxreiter, M.; Mones, L., *Current Opinion in Chemical Biology* **2014,** *21*, 34-41.

6. Gilson, M. K.; Honig, B. H., *Nature* **1987,** *330* (6143), 84-86.

7. Warwicker, J., *Journal of Theoretical Biology* **1986,** *121* (2), 199-210.

8. Sigala, P. A.; Fafarman, A. T.; Bogard, P. E.; Boxer, S. G.; Herschlag, D., *J. Am. Chem. Soc.* **2007,** *129* (40), 12104-12105.

9. Sun, D. P.; Liao, D. I.; Remington, S. J., *Proc. Natl. Acad. Sci.* **1989,** *86* (14), 5361.

10. Warshel, A., *Acc. Chem. Res.* **1981,** *14* (9), 284-290.

11. Kumar, R.; Peterson, K.; Misini Ignjatović, M.; Leffler, H.; Ryde, U.; Nilsson, U. J.; Logan, D. T., *Org. Biomol. Chem.* **2019,** *17* (5), 1081-1089.

12. Karlin, K. D., *Science* **1993,** *261* (5122), 701.

13. Denisov, I. G.; Makris, T. M.; Sligar, S. G.; Schlichting, I., *Chem. Rev.* **2005,** *105* (6), 2253-2278.

14. Fontecilla-Camps, J. C.; Volbeda, A.; Cavazza, C.; Nicolet, Y., *Chem. Rev.* **2007,** *107* (10), 4273-4303.

15. Gerber, N. C.; Sligar, S. G., *J. Am. Chem. Soc.* **1992,** *114* (22), 8742-8743.

16. Nechay, M. R.; Gallup, N. M.; Morgenstern, A.; Smith, Q. A.; Eberhart, M. E.; Alexandrova, A. N., *The Journal of Physical Chemistry B* **2016,** *120* (26), 5884-5895.

17. Valdez, C. E.; Smith, Q. A.; Nechay, M. R.; Alexandrova, A. N., *Acc. Chem. Res.* **2014,** *47* (10), 3110-3117.

18. Gamiz-Hernandez, A. P.; Kieseritzky, G.; Ishikita, H.; Knapp, E. W., *Journal of Chemical Theory and Computation* **2011,** *7* (3), 742-752.

19. Corminboeuf, C.; Hu, P.; Tuckerman, M. E.; Zhang, Y., *J. Am. Chem. Soc.* **2006,** *128* (14), 4530-4531.

20. Wu, R.; Wang, S.; Zhou, N.; Cao, Z.; Zhang, Y., *J. Am. Chem. Soc.* **2010,** *132* (27), 9471-9479.

21. Ferreira, K. N.; Iverson, T. M.; Maghlaoui, K.; Barber, J.; Iwata, S., *Science* **2004,** *303* (5665), 1831-1838.

22. Umena, Y.; Kawakami, K.; Shen, J.-R.; Kamiya, N., *Nature* **2011,** *473* (7345), 55-60.

23. Riggs-Gelasco, P. J.; Mei, R.; Ghanotakis, D. F.; Yocum, C. F.; Penner-Hahn, J. E., *J. Am. Chem. Soc.* **1996,** *118* (10), 2400-2410.

24. Yocum, C. F., *Coord. Chem. Rev.* **2008,** *252* (3–4), 296-305.

25. Cox, N.; Rapatskiy, L.; Su, J.-H.; Pantazis, D. A.; Sugiura, M.; Kulik, L.; Dorlet, P.; Rutherford, A. W.; Neese, F.; Boussac, A.; Lubitz, W.; Messinger, J., *J. Am. Chem. Soc.* **2011,** *133* (10), 3635-3648.

26. Pushkar, Y.; Yano, J.; Sauer, K.; Boussac, A.; Yachandra, V. K., *Proc. Natl. Acad. Sci.* **2008,** *105* (6), 1879-1884.

27. Ghanotakis, D. F.; Babcock, G. T.; Yocum, C. F., *FEBS Letters* **1984,** *167* (1), 127-130.

28. Lee, C.-I.; Lakshmi, K. V.; Brudvig, G. W., *Biochem.* **2007,** *46* (11), 3211-3223.

29. Vrettos, J. S.; Stone, D. A.; Brudvig, G. W., *Biochem.* **2001,** *40* (26), 7937-7945.

30. Tsui, E. Y.; Agapie, T., *Proc. Natl. Acad. Sci.* **2013,** *110* (25), 10084-10088.

31. Tsui, E. Y.; Tran, R.; Yano, J.; Agapie, T., *Nat. Chem.* **2013,** *5* (4), 293-299.

32. Park, Y. J.; Cook, S. A.; Sickerman, N. S.; Sano, Y.; Ziller, J. W.; Borovik, A. S., *Chem. Sci.* **2013,** *4* (2), 717-726.

33. Park, Y. J.; Ziller, J. W.; Borovik, A. S., *J. Am. Chem. Soc.* **2011,** *133* (24), 9258-9261.

34. Drazic, A.; Myklebust, L. M.; Ree, R.; Arnesen, T., *Biochimica et Biophysica Acta (BBA) - Proteins and Proteomics* **2016,** *1864* (10), 1372-1401.

35. Vannini, A.; Volpari, C.; Gallinari, P.; Jones, P.; Mattu, M.; Carfí, A.; De Francesco, R.; Steinkühler, C.; Di Marco, S., *EMBO reports* **2007,** *8* (9), 879-884.

36. Somoza, J. R.; Skene, R. J.; Katz, B. A.; Mol, C.; Ho, J. D.; Jennings, A. J.; Luong, C.; Arvai, A.; Buggy, J. J.; Chi, E.; Tang, J.; Sang, B.-C.; Verner, E.; Wynands, R.; Leahy, E. M.; Dougan, D. R.; Snell, G.; Navre, M.; Knuth, M. W.; Swanson, R. V.; McRee, D. E.; Tari, L. W., *Structure* **2004,** *12* (7), 1325-1334.

37. Morgenstern, A.; Jaszai, M.; Eberhart, M. E.; Alexandrova, A. N., *Chem. Sci.* **2017,** *8* (7), 5010-5018.

38. Ciampi, S.; Darwish, N.; Aitken, H. M.; Díez-Pérez, I.; Coote, M. L., *Chem. Soc. Rev.* **2018,** *47* (14), 5146-5164.

39. Shaik, S.; Ramanan, R.; Danovich, D.; Mandal, D., *Chem. Soc. Rev.* **2018,** *47* (14), 5125-5145.

40. Gorin, C. F.; Beh, E. S.; Bui, Q. M.; Dick, G. R.; Kanan, M. W., *J. Am. Chem. Soc.* **2013,** *135* (30), 11257-11265.

41. Liu, M.; Pang, Y.; Zhang, B.; De Luna, P.; Voznyy, O.; Xu, J.; Zheng, X.; Dinh, C. T.; Fan, F.; Cao, C.; de Arquer, F. P. G.; Safaei, T. S.; Mepham, A.; Klinkova, A.; Kumacheva, E.; Filleter, T.; Sinton, D.; Kelley, S. O.; Sargent, E. H., *Nature* **2016,** *537*, 382.

42. Blatter, F.; Sun, H.; Vasenkov, S.; Frei, H., *Catalysis Today* **1998,** *41* (4), 297-309.

43. Gorin, C. F.; Beh, E. S.; Kanan, M. W., *J. Am. Chem. Soc.* **2012,** *134* (1), 186-189.

44. Shaik, S.; Mandal, D.; Ramanan, R., *Nature Chemistry* **2016,** *8*, 1091.

45. Alemani, M.; Peters, M. V.; Hecht, S.; Rieder, K.-H.; Moresco, F.; Grill, L., *J. Am. Chem. Soc.* **2006,** *128* (45), 14446-14447.

46. Zhang, L.; Laborda, E.; Darwish, N.; Noble, B. B.; Tyrell, J. H.; Pluczyk, S.; Le Brun, A. P.; Wallace, G. G.; Gonzalez, J.; Coote, M. L.; Ciampi, S., *J. Am. Chem. Soc.* **2018,** *140* (2), 766-774.

47. Aragonès, A. C.; Haworth, N. L.; Darwish, N.; Ciampi, S.; Bloomfield, N. J.; Wallace, G. G.; Diez-Perez, I.; Coote, M. L., *Nature* **2016,** *531*, 88.

48. Meir, R.; Chen, H.; Lai, W.; Shaik, S., *ChemPhysChem* **2010,** *11* (1), 301-310.

49. Chan, A. L.; Estrada, J.; Kefalidis, C. E.; Lavallo, V., *Organometallics* **2016,** *35* (19), 3257-3260.

50. Kennedy, C. R.; Guidera, J. A.; Jacobsen, E. N., *ACS Central Science* **2016,** *2* (6), 416-423.

51. Holland, M. C.; Paul, S.; Schweizer, W. B.; Bergander, K.; Mück-Lichtenfeld, C.; Lakhdar, S.; Mayr, H.; Gilmour, R., *Angew. Chem. Int. Ed.* **2013,** *52* (31), 7967-7971.

52. Seguin, T. J.; Wheeler, S. E., *Angew. Chem. Int. Ed.* **2016,** *55* (51), 15889-15893.

53. Seguin, T. J.; Wheeler, S. E., *ACS Catal.* **2016,** *6* (4), 2681-2688.

54. Nguyen, Q. N. N.; Lodewyk, M. W.; Bezer, S.; Gagné, M. R.; Waters, M. L.; Tantillo, D. J., *ACS Catal.* **2015,** *5* (3), 1617-1622.

55. Lee, K.; Silverio, D. L.; Torker, S.; Robbins, D. W.; Haeffner, F.; van der Mei, F. W.; Hoveyda, A. H., *Nat. Chem.* **2016,** *8* (8), 768-777.

56. Doney, A. C.; Rooks, B. J.; Lu, T.; Wheeler, S. E., *ACS Catal.* **2016,** *6* (11), 7948-7955.

57. DiRocco, D. A.; Noey, E. L.; Houk, K. N.; Rovis, T., *Angew. Chem. Int. Ed.* **2012,** *51* (10), 2391-2394.

58. Xiao, G.; Cintron-Rosado, G. A.; Glazier, D. A.; Xi, B.-m.; Liu, C.; Liu, P.; Tang, W., *J. Am. Chem. Soc.* **2017,** *139* (12), 4346-4349.

59. Maji, R.; Wheeler, S. E., *J. Am. Chem. Soc.* **2017**.

60. Lyngvi, E.; Bode, J. W.; Schoenebeck, F., *Chem. Sci.* **2012,** *3* (7), 2346-2350.

61. Chattopadhyay, B.; Dannatt, J. E.; Andujar-De Sanctis, I. L.; Gore, K. A.; Maleczka, R. E.; Singleton, D. A.; Smith, M. R., *J. Am. Chem. Soc.* **2017,** *139* (23), 7864-7871.

62. Um, J. M.; DiRocco, D. A.; Noey, E. L.; Rovis, T.; Houk, K. N., *J. Am. Chem. Soc.* **2011,** *133* (29), 11249-11254.

63. Lu, C. C.; Peters, J. C., *J. Am. Chem. Soc.* **2002,** *124* (19), 5272-5273.

64. Lau, V. M.; Pfalzgraff, W. C.; Markland, T. E.; Kanan, M. W., *J. Am. Chem. Soc.* **2017,** *139* (11), 4035-4041.

65. Izatt, R. M.; Bradshaw, J. S.; Nielsen, S. A.; Lamb, J. D.; Christensen, J. J.; Sen, D., *Chem. Rev.* **1985,** *85* (4), 271-339.

66. Izatt, R. M.; Bradshaw, J. S.; Pawlak, K.; Bruening, R. L.; Tarbet, B. J., *Chem. Rev.* **1992,** *92* (6), 1261-1354.

67. Yoo, C.; Dodge, H. M.; Miller, A. J. M., *Chem. Commun.* **2019,** *55* (35), 5047-5059.

68. Powell, J.; Kuksis, A.; May, C. J.; Nyburg, S. C.; Smith, S. J., *J. Am. Chem. Soc.* **1981,** *103* (19), 5941-5943.

69. Powell, J.; Gregg, M.; Kuksis, A.; Meindl, P., *J. Am. Chem. Soc.* **1983,** *105* (4), 1064-1065.

70. Van Staveren, C. J.; Fenton, D. E.; Reinhoudt, D. N.; Van Eerden, J.; Harkema, S., *J. Am. Chem. Soc.* **1987,** *109* (11), 3456-3458.

71. van Staveren, C. J.; Reinhoudt, D. N.; van Eerden, J.; Harkema, S., *J. Chem. Soc., Chem. Commun.* **1987,** (13), 974-977.

72. van Veggel, F. C. J. M.; Bos, M.; Harkema, S.; Verboom, W.; Reinhoudt, D. N., *Angew. Chem. Int. Ed.* **1989,** *28* (6), 746-748.

73. Van Veggel, F. C. J. M.; Harkema, S.; Bos, M.; Verboom, W.; Woolthuis, G. K.; Reinhoudt, D. N., *J. Org. Chem.* **1989,** *54* (10), 2351-2359.

74. Van Veggel, F. C. J. M.; Harkema, S.; Bos, M.; Verboom, W.; Van Staveren, C. J.; Gerritsma, G. J.; Reinhoudt, D. N., *Inorg. Chem.* **1989,** *28* (6), 1133-1148.

75. Puntener, K.; Hellman, M. D.; Kuester, E.; Hegedus, L. S., *J. Org. Chem.* **2000,** *65* (24), 8301-8306.

76. Habata, Y.; Ikeda, M.; Sah, A. K.; Noto, K.; Kuwahara, S., *Inorg. Chem.* **2013,** *52* (20), 11697-11699.

77. Balch, A. L.; Rowley, S. P., *J. Am. Chem. Soc.* **1990,** *112* (16), 6139-6140.

78. Balch, A. L.; Neve, F.; Olmstead, M. M., *Inorg. Chem.* **1991,** *30* (18), 3395-3402.

79. Yuan, W.-B.; Wang, H.-Y.; Du, J.-F.; Chen, S.-W.; Zhang, Q., *Acta Crystallogr. Sect. E: Struct. Rep. Online* **2006,** *62* (12), m3504-m3505.

80. McLain, S. J., *J. Am. Chem. Soc.* **1983,** *105* (20), 6355-6357.

81. McLain, S. J., *Inorg. Chem.* **1986,** *25* (18), 3124-3127.

82. Okano, T.; Yamamoto, M.; Noguchi, T.; Konishi, H.; Kiji, J., *Chem. Lett.* **1982,** *11* (7), 977-980.

83. Okano, T.; Iwahara, M.; Suzuki, T.; Konishi, H.; Kiji, J., *Chem. Lett.* **1986,** *15* (9), 1467-1470.

84. Landis, C. R.; Sawyer, R. A.; Somsook, E., *Organometallics* **2000,** *19* (6), 994-1002.

85. Hazari, A.; Labinger, J. A.; Bercaw, J. E., *Angew. Chem. Int. Ed.* **2012,** *51* (33), 8268-8271.

86. Esteban-Gómez, D.; Ferreirós, R.; Fernández-Martínez, S.; Avecilla, F.; Platas-Iglesias, C.; de Blas, A.; Rodríguez-Blas, T., *Inorg. Chem.* **2005,** *44* (15), 5428-5436.

87. Esteban-Gómez, D.; Enríquez-Pérez, T.; Ferreirós-Martínez, R.; Mato-Iglesias, M.; Platas-Iglesias, C.; de Blas, A.; Rodríguez-Blas, T., *Eur. J. Inorg. Chem.* **2010,** *2010* (31), 5027-5034.

88. Miller, A. J. M., *Dalton Trans.* **2017,** *46* (36), 11987-12000.

89. Cai, Z.; Xiao, D.; Do, L. H., *J. Am. Chem. Soc.* **2015,** *137* (49), 15501-15510.

90. Cai, Z.; Do, L. H., *Organometallics* **2017,** *36* (24), 4691-4698.

91. Cai, Z.; Do, L. H., *Organometallics* **2018,** *37* (21), 3874-3882.

92. Moreira, L.; Calbo, J.; Aragó, J.; Illescas, B. M.; Nierengarten, I.; Delavaux-Nicot, B.; Ortí, E.; Martín, N.; Nierengarten, J.-F., *J. Am. Chem. Soc.* **2016,** *138* (47), 15359-15367.

93. Dürr, K.; Macpherson, B. P.; Warratz, R.; Hampel, F.; Tuczek, F.; Helmreich, M.; Jux, N.; Ivanović-Burmazović, I., *J. Am. Chem. Soc.* **2007,** *129* (14), 4217-4228.

94. Pognon, G.; Wytko, J. A.; Weiss, J., *Org. Lett.* **2007,** *9* (5), 785-788.

95. Jokic, D.; Asfari, Z.; Weiss, J., *Org. Lett.* **2002,** *4* (13), 2129-2132.

96. Thanabal, V.; Krishnan, V., *J. Am. Chem. Soc.* **1982,** *104* (13), 3643-3650.

97. Mäkelä, T.; Minkkinen, M.-E.; Rissanen, K., *Inorg. Chem.* **2016,** *55* (3), 1339-1346.

98. Coucouvanis, D., *Inorg. Chem.* **1998,** *37* (10), 2328-2329.

99. Rosa, D. T.; Young, V. G.; Coucouvanis, D., *Inorg. Chem.* **1998,** *37* (20), 5042-5043.

100. Van Staveren, C. J.; Van Eerden, J.; Van Veggel, F. C. J. M.; Harkema, S.; Reinhoudt, D. N., *J. Am. Chem. Soc.* **1988,** *110* (15), 4994-5008.

101. Delgado, M.; Ziegler, J. M.; Seda, T.; Zakharov, L. N.; Gilbertson, J. D., *Inorg. Chem.* **2016,** *55* (2), 555-557.

102. Burns, K. T.; Marks, W. R.; Cheung, P. M.; Seda, T.; Zakharov, L. N.; Gilbertson, J. D., *Inorg. Chem.* **2018,** *57* (16), 9601-9610.

103. Cheung, P. M.; Burns, K. T.; Kwon, Y. M.; Deshaye, M. Y.; Aguayo, K. J.; Oswald, V. F.; Seda, T.; Zakharov, L. N.; Kowalczyk, T.; Gilbertson, J. D., *J. Am. Chem. Soc.* **2018,** *140* (49), 17040-17050.

104. Yam, V. W.-W.; Lee, V. W.-M.; Ke, F.; Siu, K.-W. M., *Inorg. Chem.* **1997,** *36* (10), 2124-2129.

105. Charbonnière, L. J.; Ziessel, R. F.; Sams, C. A.; Harriman, A., *Inorg. Chem.* **2003,** *42* (11), 3466-3474.

106. McFarland, S. A.; Magde, D.; Finney, N. S., *Inorg. Chem.* **2005,** *44* (11), 4066-4076.

107. Liu, W.; Chen, Y.; Wang, R.; Zhou, X.-H.; Zuo, J.-L.; You, X.-Z., *Organometallics* **2008,** *27* (13), 2990-2997.

108. Suzaki, Y.; Shimada, K.; Chihara, E.; Saito, T.; Tsuchido, Y.; Osakada, K., *Org. Lett.* **2011,** *13* (15), 3774-3777.

109. Li, M.-J.; Chu, B. W.-K.; Zhu, N.; Yam, V. W.-W., *Inorg. Chem.* **2007,** *46* (3), 720-733.

110. Sawamura, M.; Nagata, H.; Sakamoto, H.; Ito, Y., *J. Am. Chem. Soc.* **1992,** *114* (7), 2586-2592.

111. Sawamura, M.; Nakayama, Y.; Tang, W.-M.; Ito, Y., *J. Org. Chem.* **1996,** *61* (26), 9090-9096.

112. Kita, M. R.; Miller, A. J. M., *Angew. Chem. Int. Ed.* **2017,** *56* (20), 5498-5502.

113. Smith, J. B.; Kerr, S. H.; White, P. S.; Miller, A. J. M., *Organometallics* **2017,** *36* (16), 3094-3103.

114. Beer, P. D., Transition Metal and Organic Redox-Active Macrocycles Designed to Electrochemically Recognize Charged and Neutral Guest Species. In *Advances in Inorganic Chemistry*, Sykes, A. G., Ed. Academic Press: 1992; Vol. 39, pp 79-157.

115. van Veggel, F. C. J. M.; Verboom, W.; Reinhoudt, D. N.; Bos, M., *Recueil des Travaux Chimiques des Pays-Bas* **1990,** *109* (10), 515-517.

116. Kumar, A.; Lionetti, D.; Day, V. W.; Blakemore, J. D., *Chem. Eur. J.* **2018,** *24* (1), 141-149.

117. Vaquero, M.; Rovira, L.; Vidal-Ferran, A., *Chem. Commun.* **2016,** *52* (74), 11038-11051.

118. Cozzi, P. G., *Chem. Soc. Rev.* **2004,** *33* (7), 410-421.

# CHAPTER 1

# ELECTROSTATIC EFFECTS ON THE ELECTRONIC STRUCTURE AND REDOX POTENTIALS OF COBALT SCHIFF BASE COMPLEXES BY REDOX INACTIVE CATIONS

Portions of this chapter have been published: Reath, A. H.; Ziller, J. W.; Tsay, C.; Ryan, A. J.; Yang, J. Y., *Inorg. Chem.* **2017,** *56* (6), 3713-3718. 

## 1.1 Motivation and Specific Aims

Redox inactive Lewis acidic cations are thought to facilitate the reactivity of metalloenzymes and their synthetic analogues by tuning the redox potential and electronic structure of the redox active site.[1-3] Electrostatic interactions, as opposed to inductive electronic effects through chemical bonds, are believed to play a predominant role.[6]

To explore and quantify electrostatic interactions in synthetic complexes, the synthesis and characterization of a series of tetradentate Schiff base ligands appended with a crown-like cavity incorporating a series of alkali and alkaline Lewis acidic cations (**1M**, M = Na(OTf), K(OTf), $Ca(OTf)_2$, $Sr(OTf)_2$, $Ba(OTf)_2$, $Y(OTf)_3$, $La(OTf)_3$, $Eu(OTf)_3$) and their corresponding $Co^{II}$ complexes (**2Co$^{II}$M**) are reported. Cyclic voltammetry of the **2Co$^{II}$M** complexes shows that the $Co^{II/I}$ reduction potentials are shifted positive by approximately 130 mV in DMF, 150 mV in THF, and 170 mV in propylene carbonate per unit of cationic charge compared to Co(salen–OMe) (salen–OMe = *N*,*N*'-bis(3-methoxysalicylidene)-1,2-diaminoethane), which lacks a proximal cation and serves as a control for inductive ligands effects. The $Co^{II/I}$ redox potentials also correlate with the ionic radius[7] and Lewis acidity of the encapsulated metal,[4] although exceptions are observed in some cases. Electronic absorption and infrared spectra indicate the Lewis acid cations have a minor effect on the electronic structure of the $Co^{II}$ ion, which suggests the shifts in redox potential are primarily a result of electrostatic effects due to the cationic charge.

## 1.2 Background

Non-redox active Lewis acidic metal cations play a key role in a diverse set of biological and synthetic transition metal complexes that mediate redox activity. In biological systems, the

$Ca^{2+}$ ion found in the oxygen evolution complex (OEC) in Photosystem II is critical for water oxidation activity.[10-19] In synthetic transition metal complexes, the presence of Lewis acidic metals are known to promote C-H oxidation,[21] oxygen atom transfer,[22-30] olefin hydrogenation,[35] and oxygen reduction[36] reactions, as well as facilitate electron transfer reactions.[37-39]

One of the proposed roles that proximal redox inactive metal cations play in promoting reactivity is by tuning the redox potential of the reaction site. Redox tuning by incorporation of redox inactive cations has been reported in several synthetic systems including mono-[4d,40] and multi-metallic manganese[41-44] and triiron[45] clusters incorporating Lewis acid cations through oxo-bridges. Additionally, pendant crown ethers encapsulating alkali or alkaline earth metals have been appended onto molybdenum,[46] ferrocene,[47-49] and iron pyridinediimine[50] complexes. The shifts in the reversible redox potential denote a change in the absolute energy of the molecular orbital participating in electron transfer. This investigation explores how the Lewis acid cations engender this change. An inductive effect due to a modification of the ligand field would result in changes to the electronic structure (or relative energy of molecular orbitals) of the redox active cation. In contrast, an electrostatic effect would uniformly shift the molecular orbitals on the redox active metal due to the electric field potential of the proximal cation.

To elucidate the source of the change in redox potential due to adjacent Lewis acidic cations, we synthesized a series of cobalt(II) Schiff base complexes with an appended crown functionality containing a series of alkali, alkaline earth metal, and rare earth cations, shown as **2Co$^{II}$M** in Chart 1.1, (M = Na(OTf), K(OTf), $Ca(OTf)_2$, $Sr(OTf)_2$, $Ba(OTf)_2$, $Y(OTf)_3$, $La(OTf)_3$, and $Eu(OTf)_3$). These compounds are well suited to investigate the nature of

**Chart 1.1:**

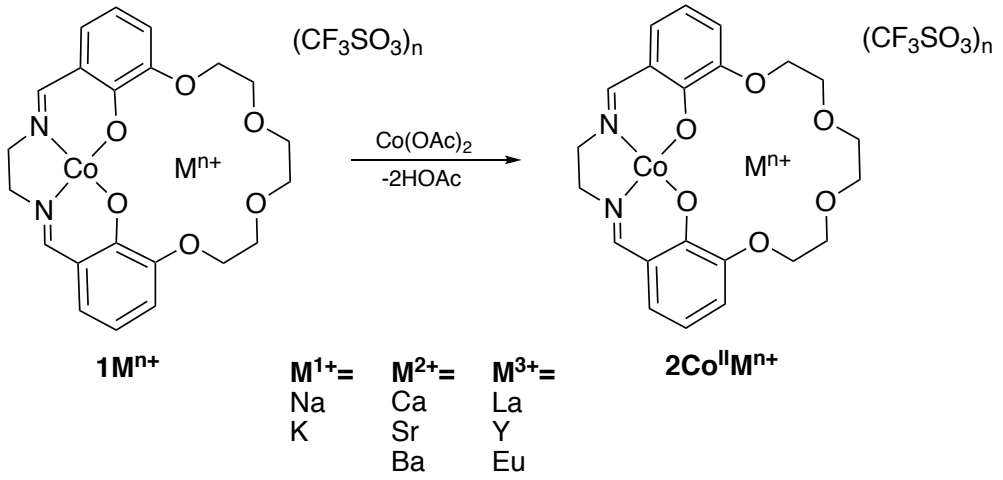


electrostatic interactions in transition metal complexes. The ligand provides a cavity similar in size to 18-crown-6, and can enclose a variety of ions with minimal effect on the coordination geometry of the $Co^{II}$ ion. Within this framework, the $Co^{II/I}$ couple is reversible, allowing a direct handle on changes in redox potential. The similar ligand environments permit facile comparisons in electronic structure of the $Co^{II}$ ions due to the Lewis acid. The localization of the redox event at a single metal center instead of a cluster permits a more accurate calculation of an electrostatic effect. The shared phenoxide ligand between the $Co^{II}$ and Lewis acid cation is also relevant to the interaction between Mn and $Ca^{2+}$ in the OEC. Additionally, redox inactive metal cations are known to play a role in synthetic water oxidation catalysts.[51-54]

## 1.3 Heterobimetallic Complexes with Group I/II Cations

### 1.3.1 Synthesis and Characterization

The Schiff base ligands **1M** contain an alkali or alkaline earth metal cation in an appended ether pocket. Using a modified literature procedure,[55] **1Ba(OTF)$_2$** was synthesized by

templating an ether linked dialdehyde with $Ba(OTf)_2$, followed by condensation with ethylenediamine. **1Na(OTf)**, **1K(OTf)**, **1Ca(OTf)$_2$**, and **1Sr(OTf)$_2$** were synthesized in a similar fashion using the appropriate metal triflate salt and purified by recrystallization. The synthesis of the trivalent **1M** ($Y(OTf)_3$, $La(OTf)_3$, and $Eu(OTf)_3$) metalloligands required the use of an alternate procedure due to synthetic incompatibilities these strong Lewis acids with the dialdehyde precursor in the templating step. These complexes were synthesized via **1Ba(OTf)$_2$** followed by removal of $Ba(OTf)_2$ with guanidine sulfate and addition of the desired triflate salt.[55-56] The **1M** series was characterized by high-resolution mass spectrometry (HRMS) and $^1H$ and $^{13}C$ NMR spectroscopy, which are shown in the (Figures 1.9-1.21). There is a linear relationship between the size of the non-redox active cation[7] and chemical shift of the phenolic protons in the $^1H$ NMR spectra for the $M^+$ and $M^{2+}$ cations, illustrated in Figure 1.22, however this trend does not hold for the trivalent **1La(OTf)$_3$**, **1Y(OTf)$_3$**, or **1Eu(OTf)$_3$**.

The ionic radius[7] of the templating alkali or alkaline earth cation has a significant effect on the synthetic accessibility of the **1M** ligand series. **1K(OTf)** is synthesized in the highest yield, while the yields for the other reported ligands decrease with larger or smaller cation sizes. The use of even smaller cations ($Li^+$ or $Mg^{2+}$) as a template did not result in the desired product. For ions too large to fit in the crown ether cavity (ionic radii >150 pm)[7], such as $Rb^+$ and $Cs^+$, mass spectrometry suggests the formation of aggregates, presumably in stacked, sandwich-like structures with the metal ions coordinated between crown ether macrocycles (see Figure 1.32 for MS from the reaction with Cs(OTf)). Sandwich complexes of this type have been observed for similar complexes containing crown ether structures and large cations.[57]

The $Co^{II}$ complexes **$2Co^{II}M$** (where M = Na(OTf), K(OTf), $Ca(OTf)_2$, $Sr(OTf)_2$, $Ba(OTf)_2$) were synthesized by refluxing the corresponding **1M** ligand with one equivalent of $Co(OAc)_2$ in methanol, followed by removal of solvent and acetic acid *in vacuo*. The identities of the compounds were confirmed using mass spectrometry and single crystal X-ray diffraction analysis, and the purities by elemental analysis. Co(salen–OMe) (salen–OMe = *N*,*N*'-bis(3-methoxysalicylidene)-1,2-diaminoethane) was prepared for comparison with the **$2Co^{II}M$** complexes. Salen–OMe (*N*,*N*′-ethylenebis(3-methoxysalicylimine) was synthesized according to a literature procedure,[58] and metallation with $Co(OAc)_2$ was based on a preparation of Co(*N*,*N*′-ethylenebis(3-methoxysalicylimine)).[59]

### 1.3.2 Solid State Structures

Single crystals suitable for X-ray diffraction were grown by diffusion of diethyl ether into methanol solutions of the respective compounds. The solid state structures for the **$2Co^{II}M$** triflate salts and Co(salen–OMe) are shown in Figure 1.1 The X-ray crystallographic data for **$2Co^{II}Na(OTf)$** and **$2Co^{II}K(OTf)$** had significant disorder. Higher quality structures of the analogous tetrafluoroborate salts for **$2Co^{II}Na(BF_4)$** and **$2Co^{II}K(BF_4)$** are provided in the Figures 1.33 and 1.34. In all of the heterobimetallic complexes, the counteranion(s) are bound to the M cation. In the case of **$2Co^{II}Ba(OTf)_2$**, a molecule of methanol is coordinated to the $Ba^{2+}$ cation along with two triflate anions, which form a symmetric bridge to another **$2Co^{II}Ba(OTf)_2$** complex. The mass spectrum only has a peak consistent with the monomer, suggesting the dimer only exists in the solid state. As opposed to the rest of the series, which maintains a 4-coordinate

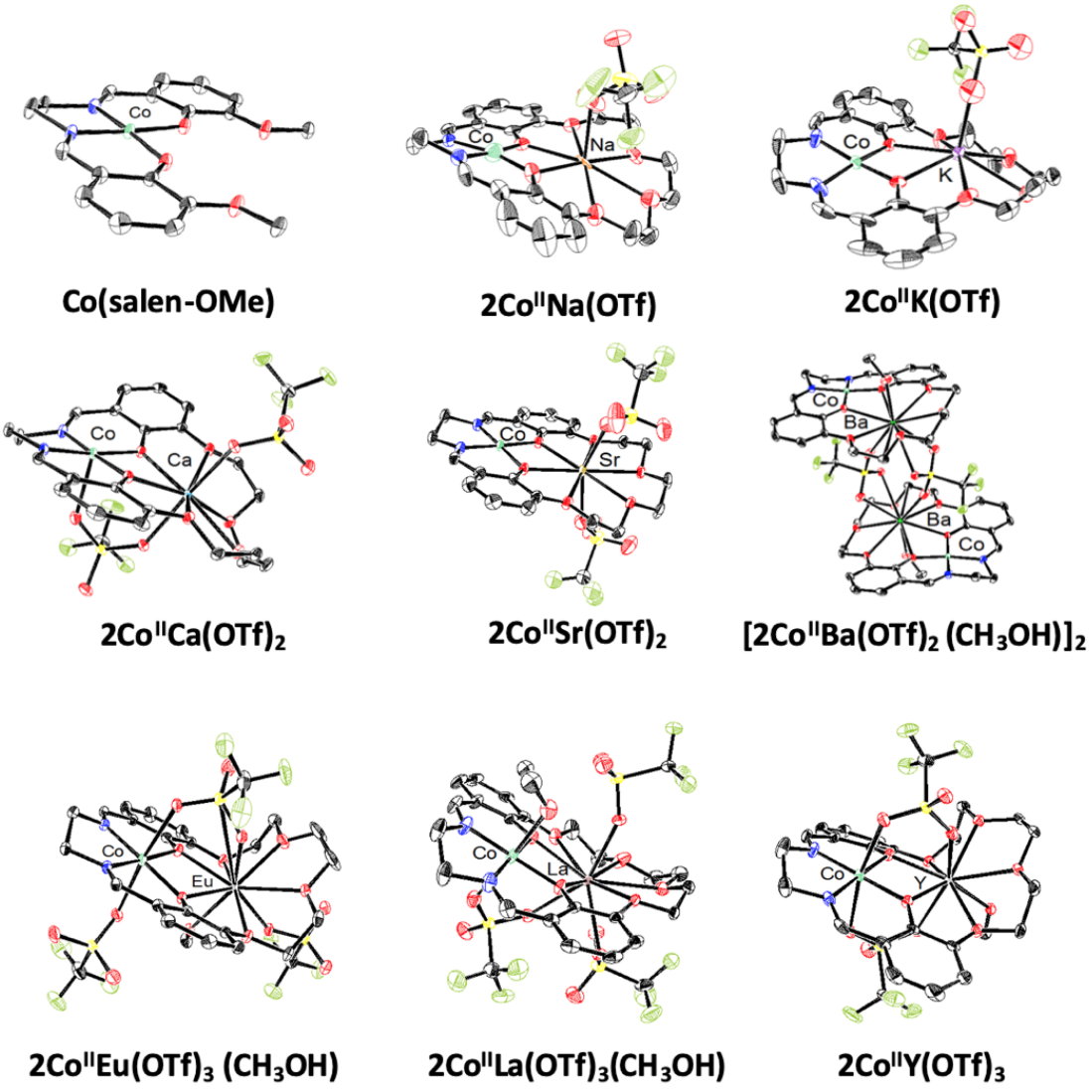


**Figure 1.1:** Solid state structures of Co(salen−OMe), **2Co$^{II}$Na(OTf)**, **2Co$^{II}$K(OTf)**, **2Co$^{II}$Ca(OTf)$_2$**, **2CoSr$^{II}$ (OTf)$_2$**, and **2Co$^{II}$Ba(OTf)$_2$**. Thermal ellipsoids are drawn to 50% probability. Hydrogen atoms and outersphere anions and solvent molecules have been omitted for clarity. For Co(salen−OMe) and **2Co$^{II}$Sr(OTf)$_2$**, only one molecule of two in the asymmetric unit cell is shown. For **2Co$^{II}$K(OTf)**, **2Co$^{II}$Na(OTf)**, and **2Co$^{II}$Sr(OTf)$_2$**, only the major position of a disordered system is displayed.

**Table 1.1:** Selected crystallographic data for **2Co$^{II}$M**. $\tau_4$ refers to the geometry index for four coordinate species, where 0 is ideal square planar and 1 is ideal tetrahedral geometries. $\tau_5$ refers to the geometry index for five coordinate species, where 0 is ideal square pyramidal and 1 is ideal trigonal bipyramidal

| Complex | Co···M(Å) | Geometry index, Co(II) ion |
|---|---|---|
| **Co(salen–OMe)** | -- | $\tau_4$ = 0.0303 |
| **2Co$^{II}$K(OTf)** | 3.6694(1) | $\tau_4$ = 0.1148 |
| **2Co$^{II}$Na(OTf)** | 3.338(5) | $\tau_4$ = 0.0295 |
| **2Co$^{II}$Ba(OTf)$_2$** | 3.7045(2) | $\tau_4$ = 0.1113 |
| **2Co$^{II}$Sr(OTf)$_2$** | 3.6078(4) | $\tau_4$ = 0.0622 |
| **2Co$^{II}$Ca(OTf)$_2$** | 3.3578(4) | $\tau_5$ = 0.0748 |
| **2Co$^{II}$Y(OTf)$_3$** | 3.3153(3) | -- |
| **2Co$^{II}$La(OTf)$_3$** | 3.4509(4) | -- |
| **2Co$^{II}$Eu(OTf)$_3$** | 3.5666(6) | -- |

geometry around the Co center, **2Co$^{II}$Ca(OTf)$_2$** features an axially coordinated triflate anion, and the trivalent **2Co$^{II}$Y(OTf)$_3$**, **2Co$^{II}$La(OTf)$_3$**, and **2Co$^{II}$Eu(OTf)$_3$** contain a combination of two axial triflates or methanol ligands. Selected crystallographic data is presented in Table 1.1

### 1.3.3 Electrostatic Influence on Reduction Potential

The shift in reduction potential enacted by the cation was measured relative to Co(salen-OMe), which served as an acceptable control compound due to the due to the similar inductive effects of the methoxy functional group to the crown ether moiety of the **2Co$^{II}$M** complexes. In dimethylformamide, Co(salen–OMe) displays a reversible reduction at -1.72 V versus ferrocene/ferrocenium (Figure 1.2, top, black trace), consistent with literature values for a Co$^{II/I}$ redox couple.[60] The Co$^{II/I}$ couples of **2Co$^{II}$M** are also reversible and display an anodic shift (more positive reduction potential) relative to Co(salen-OMe). The Co$^{III/II}$ couples, while also

accessible by voltammetric methods, displayed poor electron transfer kinetics in the **2Co$^{II}$M** species, which made precise measurements of these potentials difficult. Titrations of **2Co$^{II}$Na(OTf)**, **2Co$^{II}$Ca(OTf)$_2$,** and **2Co$^{II}$Ba(OTf)$_2$** with an excess of the corresponding metal triflate salt indicate that equilibrium effects due to cation dissociation do not have a significant role in the observed reduction potential shifts (Figures 1.23-1.25).

A correlation can be established between the shift in the $Co^{II/I}$ reduction potential and the Lewis acidity of the encapsulated ion (Table 1.6),[4] similar to the effect observed by metalloclusters incorporating redox inactive cations.[41-45] Previous studies incorporating alkali and alkaline earth metal cations into Schiff base complexes with Cu, Ni, and Zn display anodic shifts of similar magnitudes in the reduction potential.[61-63] In these studies, changes in reduction potential were attributed to inductive effects from the Lewis acid,[64-65] in which the electron

| Complex | p$K_a$ of $M(OH_2)(aq.)$[4] | Ionic radius of M, 6-coordinate (Å)[7] |
|---|---|---|
| **2Co$^{II}$K(OTf)** | 16.25[a] | 1.38 |
| **2Co$^{II}$Na(OTf)** | 14.77[b] | 1.02 |
| **2Co$^{II}$Ba(OTf)$_2$** | 13.36[b] | 1.35 |
| **2Co$^{II}$Sr(OTf)$_2$** | 13.18[b] | 1.18 |
| **2Co$^{II}$Ca(OTf)$_2$** | 12.60[b] | 1.00 |
| **2Co$^{II}$Y(OTf)$_3$** | 9.10[c] | 1.04 |
| **2Co$^{II}$La(OTf)$_3$** | 10.1[c] | 1.032 |
| **2Co$^{II}$Eu(OTf)$_3$** | 8.03[c] ($Eu^{3+}$) | 0.947 |

**Table 1.2:** Left: Lewis acidity values for the corresponding M species in **2Co$^{II}$M**, measured as the p$K_a$ of the metal hydroxide salt.[4] [a]Measured electrometrically in cells containing Ag/AgCl with hydrogen electrodes. [b]Calculated through vapor pressure measurements of an aqueous solution. [c]Measured from pH changes during titrations using glass electrodes. Right: Ionic radii of relevant metal ions in **2Co$^{II}$M**.[7]

density of the transition metal is affected in a through-bond fashion via the molecular orbital manifold of its ligand framework. However, notable examples exist in which differences in Lewis acidity does not lead to a change in reduction potential of a nearby transition metal, including **2Co$^{II}$K(OTf)** and **2Co$^{II}$Na(OTf)** in this work and between $Ca^{2+}$ and $Sr^{2+}$ in Mn metalloclusters.[41-42]

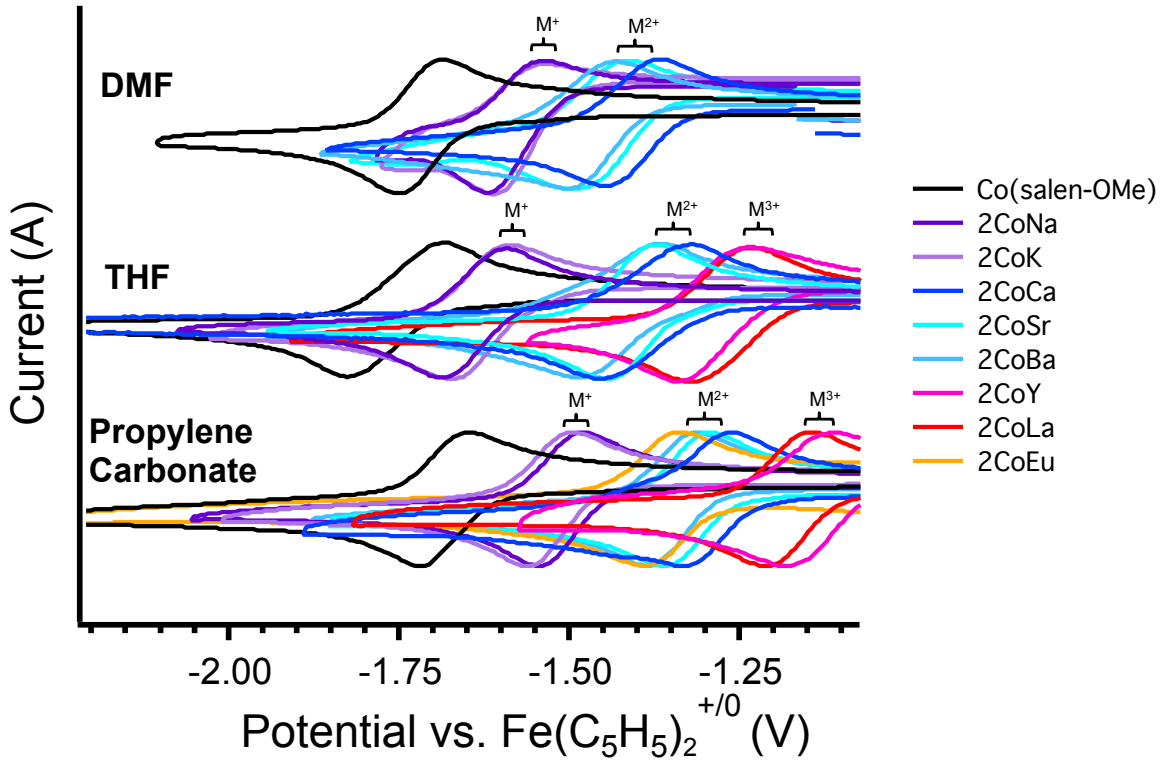


**Figure 1.2:** Cyclic voltammograms of the reversible $Co^{II/I}$ redox couples of Co(salen−OMe) and **2CoM** (M = Na(OTf), K(OTf), $Ca(OTf)_2$, $Sr(OTf)_2$, $Ba(OTf)_2$, $Y(OTf)_3$, $La(OTf)_3$, $Eu(OTf)_2$) in DMF (top), THF (middle), and propylene carbonate at 100 mV/s under an $N_2$ atmosphere in 0.1 M $TBAPF_6$ as a supporting electrolyte. Current values have been normalized for better visual comparison. The $Eu^{III/II}$ couple of **2CoEu(OTf)$_3$** can be observed at 0.845 V in propylene carbonate.

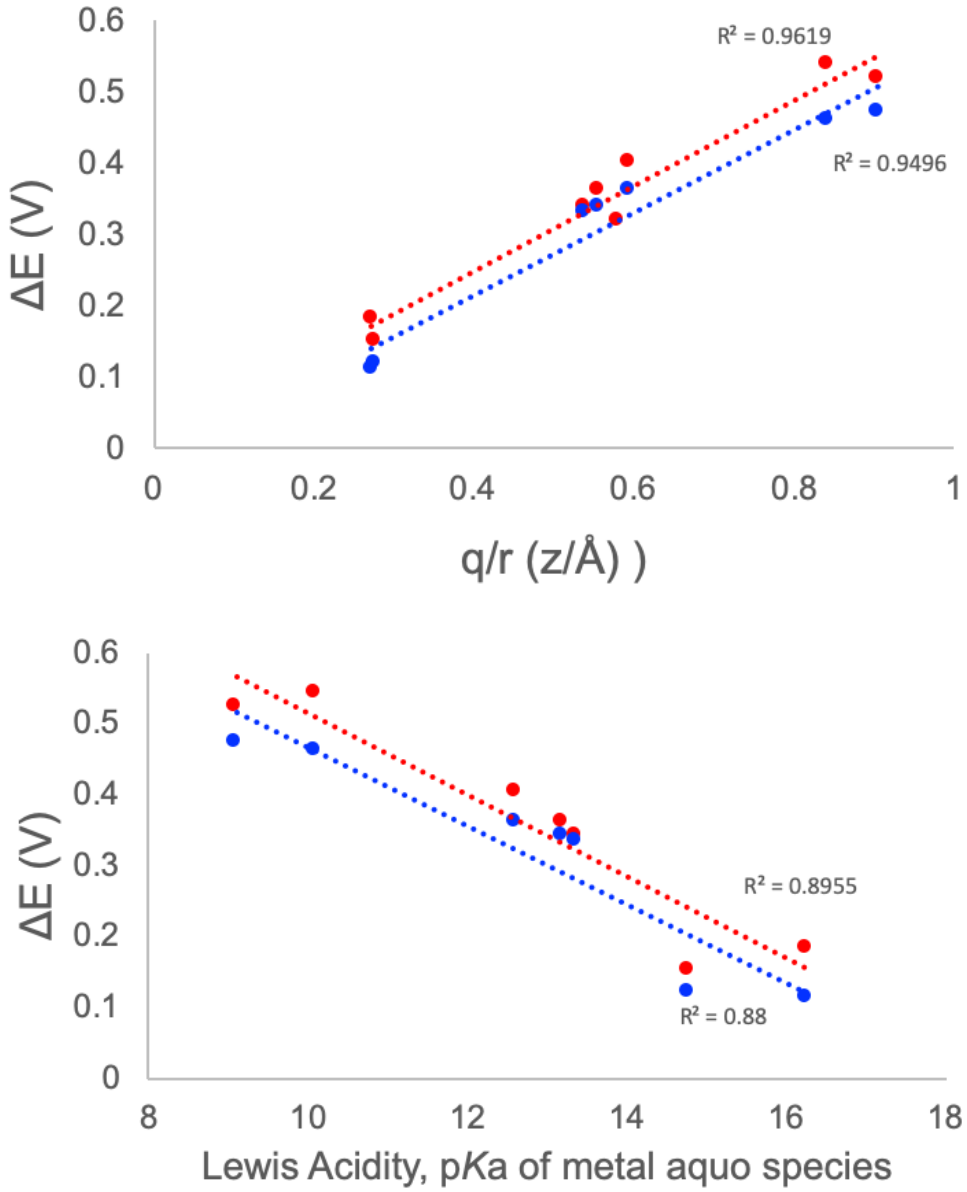


**Figure 1.3:** Top: Shift in $Co^{II/I}$ reduction potential versus the charge of the encapsulated cation (in elementary charge) divided by the Co–M distance in angstroms. This relationship should be linear according to classical electrostatics (Eq. 1). Bottom: Shift in $Co^{II/I}$ reduction potential versus the Lewis acidity of the encapsulated metal. See Table 1.6 for more information on the Lewis acidity measurements.

**Table 1.3:** Compiled electrochemical data from cyclic voltammetric measurements of **2Co$^{II}$M**.
[a]Europium acts as an $M^{2+}$ ion on the $Co^{II/I}$ reduction potential of **2CoEu(OTf)$_3$** due to the $Eu^{III/II}$ reduction at -0.85 V.
[b]Gutmann Donor Numbers determined through thermodynamic calculations based on NMR shifts of Lewis acids.[5] A larger donor indicates a stronger coordination ability towards Lewis acids. [5, 8]
[c]Coordination power measured on the basis of 10Dq values for $Ni^{II}$ ions and are established by the logarithmic coordinating ability relative to acetonitrile, where a larger value indicates stronger binding).[9]
[d] $a^{TM}$ determine through a structural database search of solvent-bound transition metals and calculated using the equation $a^{TM} = \log(c+s)/u$, where c = coordinated solvent, s = semi-coordinated solvent, and u = uncoordinated solvent.[20]
[e] $a^{La}$ determined through identical means as $a^{TM}$ using lanthanide complexes.[20]

| | **DMF** | | **THF** | | **Propylene Carbonate** | |
|---|---|---|---|---|---|---|
| Complex | $E_{1/2}$ $Co^{II/I}$ (V) | ΔE (V) | $E_{1/2}$ $Co^{II/I}$ (V) | ΔE (V) | $E_{1/2}$ $Co^{II/I}$ (V) | ΔE (V) |
| **Co(salen–OMe)** | -1.71 | -- | -1.75 | -- | -1.69 | -- |
| **2Co$^{II}$K(OTf)** | -1.58 | 0.13 | -1.64 | 0.11 | -1.54 | 0.18 |
| **2Co$^{II}$Na(OTf)** | -1.58 | 0.13 | -1.63 | 0.12 | -1.51 | 0.15 |
| **2Co$^{II}$Ba(OTf)$_2$** | -1.48 | 0.23 | -1.42 | 0.33 | -1.35 | 0.34 |
| **2Co$^{II}$Sr(OTf)$_2$** | -1.44 | 0.27 | -1.41 | 0.34 | -1.33 | 0.36 |
| **2Co$^{II}$Ca(OTf)$_2$** | -1.41 | 0.30 | -1.39 | 0.36 | -1.29 | 0.40 |
| **2Co$^{II}$Y(OTf)$_3$** | -- | -- | -1.29 | 0.46 | -1.15 | 0.54 |
| **2Co$^{II}$La(OTf)$_3$** | -- | -- | -1.28 | 0.47 | -1.17 | 0.52 |
| **2Co$^{II}$Eu(OTf)$_3$**[(a)] | -- | -- | -- | -- | -1.37 | 0.32 |
| Solvent Dielectric Constant[31-34] | 39.9 | | 8.2 | | 64.9 | |
| Gutmann Donor Number[(b)] (kcal/mol) | 26.6 | | 20.0[5] | | 15.1 | |
| Coordination power[(c)] | 0.72 | | -- | | -0.77 | |
| $a^{TM}$[(d)] | -0.2 | | -0.3 | | -- | |
| $a^{La}$[(e)] | 0.8 | | 0.4 | | -- | |

One explanation for the anodic shifts in redox potential is through an electric field potential imposed by the non-redox active cation. An electrostatic effect has been cited as the source of redox potential shifts in other heterobimetallic complexes.[47-49, 66-67] On a macroscopic scale, the electric field potential (ΔE, in V) enacted by a point charge $q$ (C) is described by Eq 1, where $r$ is the distance from the point charge to a reference and ϵ is the dielectric constant between them.

$$\Delta E = \frac{q}{4\pi\epsilon r} \qquad \text{(Eq 1)}$$

Using this relationship, the expected shift in reduction potential experienced by **2Co$^{II}$M** should be a function of the charge of M (1.602 x $10^{-9}$ C per unit of charge) and the Co–M distance. The distance $r$ can be approximated sing the crystallographic metal-metal distance, assuming the solid-state data is an accurate representation of the solvated complex. An electrostatic interaction would explain the identical redox potentials observed for **2Co$^{II}$K** and **2Co$^{II}$Na**. Although there is a difference in Lewis acidity between the monocations,[4, 63] the distance between $Co^{II}$ and $K^+$ or $Na^+$ is nearly the same, resulting in essentially the same electrostatic potential on $Co^{II}$ (Table 1.2). The redox potentials of the dications trends with the Lewis acidity[4] of M, but the Lewis acidity is also directly related to the ionic radii of M[7] (and therefore Co–M distance). The latter is reflected in changes in r due to the size of M. An electrostatic effect has been cited as the source of redox potential shifts in other heterobimetallic complexes.[47-49, 66-67] A further assumption is that the dielectric constant, $\epsilon$ is accurately represented by the solvent dielectric.

In order to better understand the role of solvent effects on the interaction between the Lewis acid cation and transition metal center, the reduction potentials of the **2Co$^{II}$M** complexes were measured in dimethylformamide (DMF), tetrahydrofuran (THF), and propylene carbonate (PC). The dielectric constant for these three solvents are 39.9, 8.2, and 64.9, respectively (Table 1.2). If the dielectric between the cation and redox-active metal were accurately represented by the solvent dielectric, the largest potential shifts would be expected in THF (poor charge screening), followed by DMF and PC.

In dimethylformamide, the anodic shift of the $Co^{II/I}$ reduction potential relative to Co(salen-OMe) is 130 mV for the monocationic complexes ((M = Na(OTf), K(OTf))and 230-300 mV for the dicationic complexes (M = $Ca(OTf)_2$, $Sr(OTf)_2$, $Ba(OTf)_2$) averaging 130 mV per unit of charge on M. Reduction potentials for the trivalent **2Co$^{II}$La(OTf)$_3$**, **2Co$^{II}$Y(OTf)$_3$**, or **2Co$^{II}$Eu(OTf)$_3$** were unable to be measured accurately in dimethylformamide due to solvent incompatibilities, possibly due to the presence of dimethylamine, a known thermal decomposition product of DMF that can coordinate with lanthanides.[68-70] In THF, the magnitude of the shift in reduction potential is notably larger, and although the monocationic **2Co$^{II}$Na(OTf)** and **2Co$^{II}$K (OTf)** undergo reduction at more negative potentials than expected, the average $\Delta E_{1/2}$ increases by 150 mV per unit of charge of M. In propylene carbonate, the average shift in the $Co^{II/I}$ reduction potential is even further augmented to 170 mV per unit of charge on M. **2Co$^{II}$Eu(OTf)$_3$** is noteworthy due to the accessible reduction potential of $Eu^{III/II}$, which occurs at more positive potentials than the $Co^{II/I}$ couple; consequently, its interaction with the cobalt reduction is as a dication. Cyclic voltammetry experiments of **2Co$^{II}$Eu(OTf)$_3$** and **1Eu(OTf)$_3$**

show that the reduction potential of the $Eu^{III/II}$ couple is not affected by the presence of cobalt (Figure 1.27)

The observed magnitude of the reduction potential shift does not support the conclusion that solvent dielectric constant is primarily responsible for electrostatic screening between Co and the encapsulated cation (Table 1.2). Solvent dielectric constants are a macroscopic measurement indicative of the long-range screening of charge due to solvent molecule

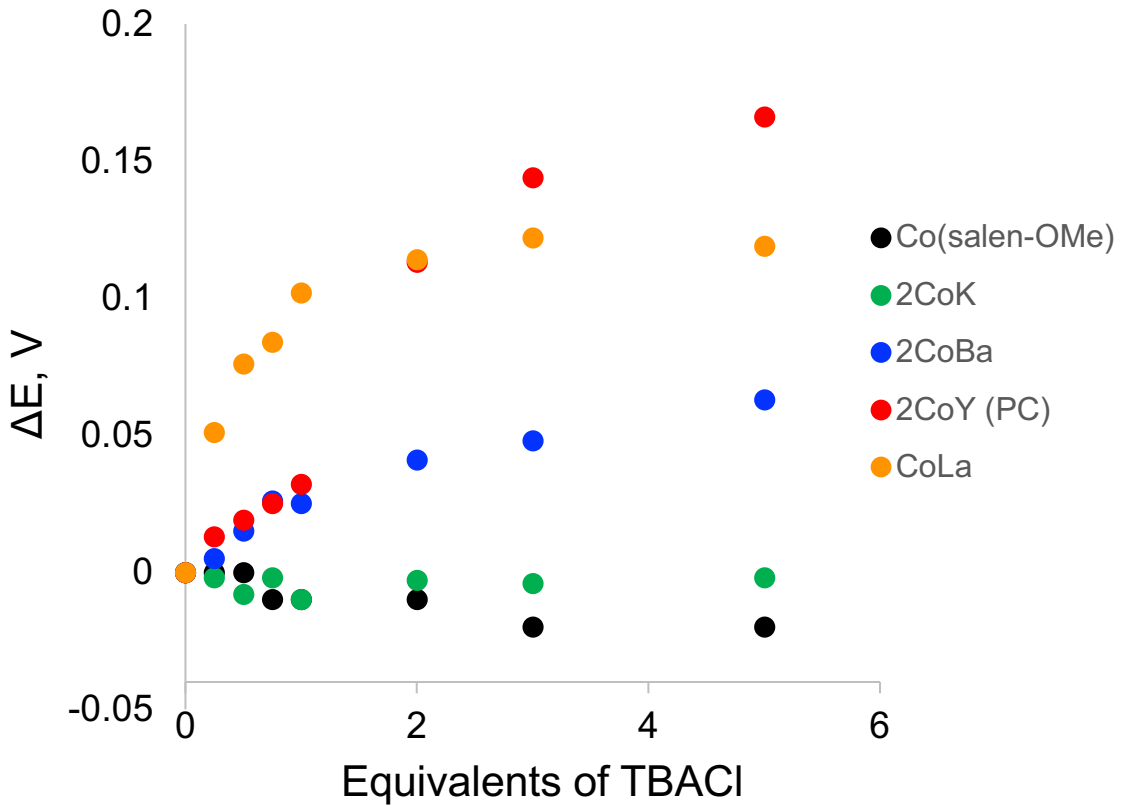


**Figure 1.4:** Electrochemical data from the titration of tetrabutylammonium chloride with various **$Co^{II}M$** complexes. Cyclic voltammetry was conducted in dimethylformamide unless otherwise noted at 100 mV/s. Y-axis represents change in $Co^{II/I}$ reduction potential versus measurement at 0 equivalents TBACl. Individual titrations are shown in Figures 1.27-1.31.

rearrangements; consequently, the same phenomena are likely not directly applicable to the angstrom-scale distances involved in the calculation of the electric potential in this case.

Instead, the degree of electrostatic screening is more closely correlated with the coordination ability of the solvent. Considering the interaction between a solvated metal complex and the surrounding solvent sphere, a more coordinating environment should result in a larger degree of electric charge screening due to polarization of the nearby solvent molecules. Because solvent can interact with either the Co or M species in **2Co$^{II}$M**, both metals must be considered. Although solvents differ in their relative coordination strength depending on the acceptor (e.g. transition metals or a Lewis acid cation),[20] the most relevant benchmarks (Table 1.2) indicate that DMF is the most highly coordinating solvent in all cases, and that THF is more coordinating than PC to main group Lewis acids. These findings appear to indicate that solvent donor ability is primarily responsible for electric potential screening in the short-range electrostatic interaction between Co and M.

In addition to solvent interactions, the role of anion coordination in the mediation of electrostatic potentials in the **2Co$^{II}$M** series was also of interest. Chloride anions were expected to have a significant effect due to their high affinity for group I/II metals and lanthanides.[71] Subsequent experiments were conducted by titrating equivalents of tetrabutylammonium chloride into a solution of **2Co$^{II}$M** (M = K(OTf), Ba(OTf$_2$) La(OTf)$_3$, Y(OTf)$_3$) and Co(salen-OMe) containing a 100-fold excess of tetrabutylammonium hexafluorophosphate supporting electrolyte (Figures 1.4 and 1.27-1.31). Compared to Co(salen-OMe), the effect of chloride equivalents results in an increasingly large negative shift in reduction potentials with increasing

charge ($K^+ < Ba^{2+} < La^{3+}$). As mentioned above, **$2Co^{II}M^{3+}$** do not have ideal electrochemical behavior in DMF, which is noted in consideration of the **$2Co^{II}La^{3+}$** data in Figures 1.4 and 1.30. To provide supporting evidence of the chloride interaction with the trivalent species, the analogous titration of **$2Co^{II}Y^{3+}$** in PC is also displayed. These results of these experiments demonstrate that the presence of the more coordinating chloride anions[20] contribute to the quenching of the electrostatic potential effects observed by the $Co^{II}$ center. The nature of the interaction of the chloride anion cannot be stated conclusively. One explanation is that the presence of this hard anionic species in close proximity to either metal is in direct opposition to the positive electrostatic field generated by M. Another possibility is that the chloride anion interacts directly with cobalt, which would alter the metal geometry and change the frontier molecular orbital energies. UV-vis spectroscopy shows changes to the electronic transitions of **$2Co^{II}La(OTf)_3$** upon addition of tetrabutylammonium chloride (Figure 1.36), but no changes are observed for $Co^{II}$(salen-OMe) (Figure 1.35). The changes observed for **$2Co^{II}La(OTf)_3$** could indicate chloride binding at the cobalt center, but the lack of any effects on the reduction potential or electronic spectra of $Co^{II}$(salen-OMe) indicates that this interaction is enabled by the presence of the cation. Crystallization of the product of the reaction of tetrabutylammonium chloride with **$2Co^{II}La(OTf)_3$** have not yielded data of sufficient quality for determining identity.

### 1.3.4 Electronic and Infrared Spectroscopy

In order to learn more about the effects of M on the electronic structure of the $Co^{II}$ center, the compounds were examined by electronic absorption and infrared spectroscopy. The electronic absorption spectra in dimethylformamide are shown in Figure 1.5 and Table 1.3. The

absorption spectrum of Co(salen–OMe) exhibits $\pi \rightarrow \pi^*$ and $d \rightarrow \pi^*$ (MLCT) transitions[72-73] at 360 nm and 415 nm, respectively. The $\pi \rightarrow \pi^*$ band is partially obscured in **2Co$^{II}$M**, but a slight red shift (≤ 15 nm) is observed for dicationic **2Co$^{II}$Ca(OTf)$_2$**, **2Co$^{II}$Sr(OTf)$_2$**, and **2Co$^{II}$Ba(OTf)$_2$**. The molar absorptivity for the $d \rightarrow \pi^*$ charge transfer band in **2Co$^{II}$K(OTf)** and **2Co$^{II}$Na(OTf)** is comparable to Co(salen–OMe) for this transition, while for **2Co$^{II}$Ca(OTf)$_2$, 2Co$^{II}$Ba(OTf)$_2$**, and **2Co$^{II}$Sr(OTf)$_2$** it has significantly lowered absorptivity. Co(salen–OMe) also has an absorption at 480 nm; this peak is likely obscured in the **2Co$^{II}$M** spectra by more intense neighboring absorptions. However, the second $d \rightarrow d$ transition at 555 nm for Co(salen–OMe) is present in **2Co$^{II}$M**, with a minor red shift of 10 nm and 25 nm for the monocationic versus dicatonic complexes, respectively. Although the changes in the absorption spectra indicate M has some

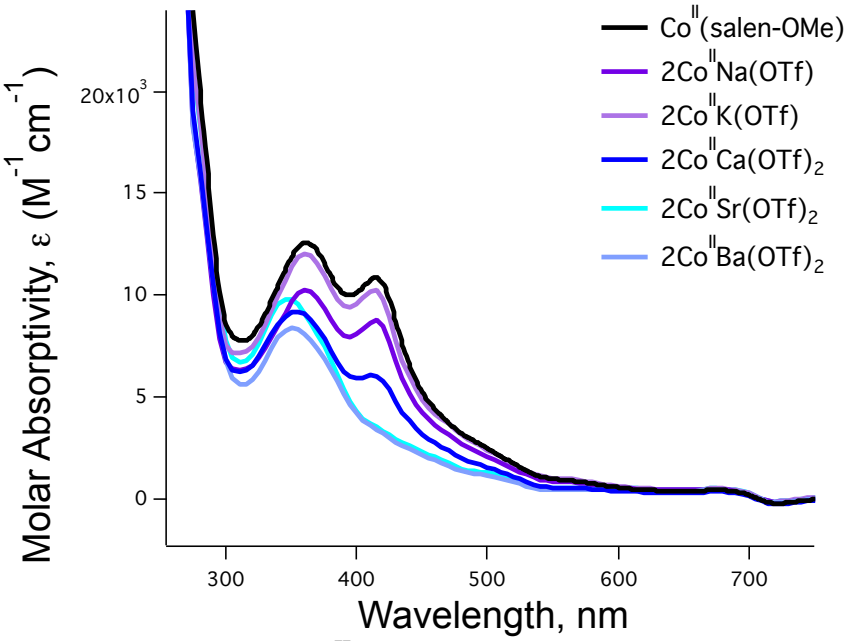


**Figure 1.5:** UV-Vis spectra of **2Co$^{II}$M** complexes in dimethylformamide. The trivalent species **2Co$^{II}$Y(OTf)$_3$**, **2Co$^{II}$La(OTf)$_3$**, and **2Co$^{II}$Eu(OTf)$_3$** were not measured due to previously observed solvent incompatibilities in DMF.

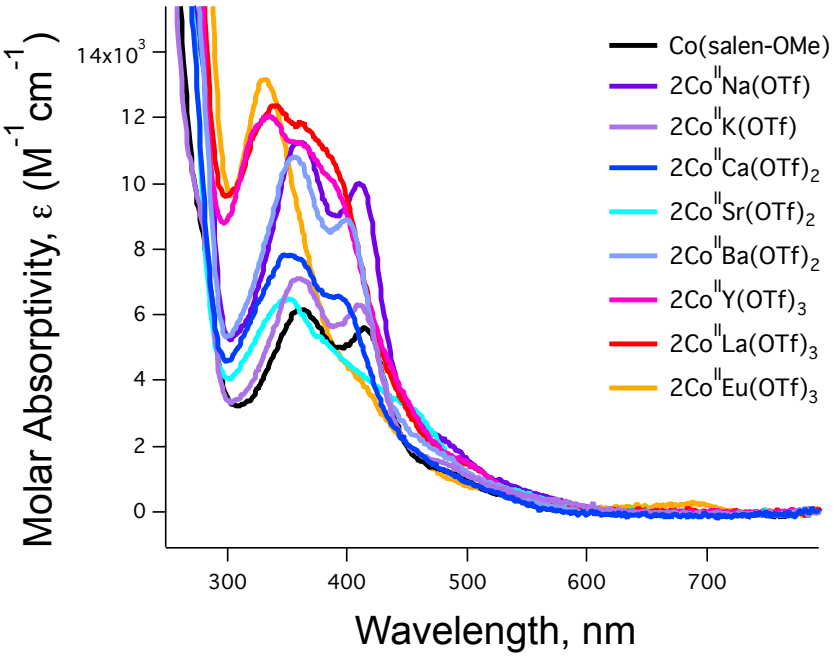


**Figure 1.6:** UV-Vis spectra of **2Co$^{II}$M** complexes in propylene carbonate.

influence on the ligand field around the Co$^{II}$ ion, the overall effect appears minimal compared to the changes in redox potential.

In propylene carbonate (Figure 1.6 and Table 1.4), the trivalent species (M = La(OTf)$_3$, Y(OTf)$_3$, and Eu(OTf)$_3$) were also able to be examined. While the mono- and dicationic **2Co$^{II}$M** again display similar behavior in PC as observed in DMF, the **Co$^{II}$M$^{3+}$** absorptions deviate from the rest of the series. The $\pi \rightarrow \pi^*$ transitions of the trivalent species exhibit a blue shift of approximately 20 nm relative to the rest of the series. Similarly, the $d \rightarrow \pi^*$ transition also shift to higher energies by approximately 30 nm. The $d \rightarrow d$ transitions for the monocationic complexes display a blue shift of approximately 10 nm, similar to those observed in DMF. However, the dicationic species shift to higher energies by nearly 35-40 nm, and the tricationic variants shift by 45-55 nm. In the electrochemical studies described in section **1.3.3**, it was shown that DMF

has a significant inhibiting effect on the electrostatic interactions between Co and M. These results could be indicative of a similar phenomenon regarding perturbations to the electronic structure of the **2Co$^{II}$M** complexes. The trivalent species in particular show significant changes in the absorption energies of the ligand-based transitions, which is likely indicative of interactions between the encapsulated cation and the extended pi system of the Schiff base ligand framework.

**Table 1.4:** UV-Vis data for **2Co$^{II}$M** complexes in dimethylformamide. The trivalent species **2Co$^{II}$Y(OTf)$_3$**, **2Co$^{II}$La(OTf)$_3$**, and **2Co$^{II}$Eu(OTf)$_3$** were not measured due to previously observed solvent incompatibilities in dimethylformamide.

| Complex | $\lambda_{d\rightarrow d}$, DMF, nm ($\varepsilon$, $M^{-1}cm^{-1}$) | $\lambda_{\pi\rightarrow\pi^*}$, DMF, nm ($\varepsilon$, $M^{-1}cm^{-1}$) | $\lambda_{d\rightarrow\pi^*}$, DMF, nm ($\varepsilon$, $M^{-1}cm^{-1}$) |
|---|---|---|---|
| **Co(salen–OMe)** | 555 (790) | 362 (12571) | 415 (10863) |
| **2Co$^{II}$K(OTf)** | 545 (767) | 360 (12064) | 415 (10251) |
| **2Co$^{II}$Na(OTf)** | 545 (634) | 360 (10233) | 415 (8758) |
| **2Co$^{II}$Ba(OTf)$_2$** | 530 (979) | 350 (8389) | -- |
| **2Co$^{II}$Sr(OTf)$_2$** | 530 (1012) | 345 (9808) | -- |
| **2Co$^{II}$Ca(OTf)$_2$** | 530 (881) | 355 (9198) | 415 (6045) |

**Table 1.5:** UV-Vis data for **2Co$^{II}$M** complexes in propylene carbonate.

| Complex | $\lambda_{d\rightarrow d}$, PC, nm ($\varepsilon$, $M^{-1}cm^{-1}$) | $\lambda_{\pi\rightarrow\pi^*}$, PC, nm ($\varepsilon$, $M^{-1}cm^{-1}$) | $\lambda_{d\rightarrow\pi^*}$, PC, nm ($\varepsilon$, $M^{-1}cm^{-1}$) |
|---|---|---|---|
| **Co(salen–OMe)** | 560 (274) | 362 (6158) | 415 (5585) |
| **2Co$^{II}$K(OTf)** | 552 (698) | 361 (7123) | 411 (6280) |
| **2Co$^{II}$Na(OTf)** | 550 (558) | 362(11247) | 411 (10006) |
| **2Co$^{II}$Ba(OTf)$_2$** | 524 (793) | 355 (10830) | 401 (8901) |
| **2Co$^{II}$Sr(OTf)$_2$** | 525 (801) | 349 (6474) | -- |
| **2Co$^{II}$Ca(OTf)$_2$** | 521 (649) | 351 (7773) | 393 (6536) |
| **2Co$^{II}$Y(OTf)$_3$** | 505 (1396) | 361 (12105)<br>336 (12027) | 361 (11256) |
| **2Co$^{II}$La(OTf)$_3$** | 505 (1397) | 362 (11852)<br>342 (12358) | 383 (10907) |
| **2Co$^{II}$Eu(OTf)$_3$** | 517 (683) | 332(13166) | -- |

The solid-state infrared spectra of **2Co$^{II}$M** were taken to compare the electronic environments of the cobalt center. The vibrational frequency of the imine C=N bond for **2Co$^{II}$M** increases slightly with the Lewis acid strength of M (Figure 1.7 and Table 1.5) and is correlated with the Co$^{II/I}$ reduction potential (Figure 1.8). The cause of the dependence of the C=N stretching frequency on reduction potential could be due to pi-backbonding interactions as well as a vibrational Stark effect generated by the electrostatic field.[74]

**Table 1.6:** Infrared frequencies of the C=N stretch for **2Co$^{II}$M** complexes.

| Complex | ν(C=N) (cm$^{-1}$) |
|---|---|
| **Co(salen–OMe)** | 1535 |
| **2Co$^{II}$K(OTf)** | 1544 |
| **2Co$^{II}$Na(OTf)** | 1546 |
| **2Co$^{II}$Ba(OTf)$_2$** | 1548 |
| **2Co$^{II}$Sr(OTf)$_2$** | 1552 |
| **2Co$^{II}$Ca(OTf)$_2$** | 1557 |
| **2Co$^{II}$Y(OTf)$_3$** | 1565 |
| **2Co$^{II}$La(OTf)$_3$** | 1560 |
| **2Co$^{II}$Eu(OTf)$_3$** | 1561 |

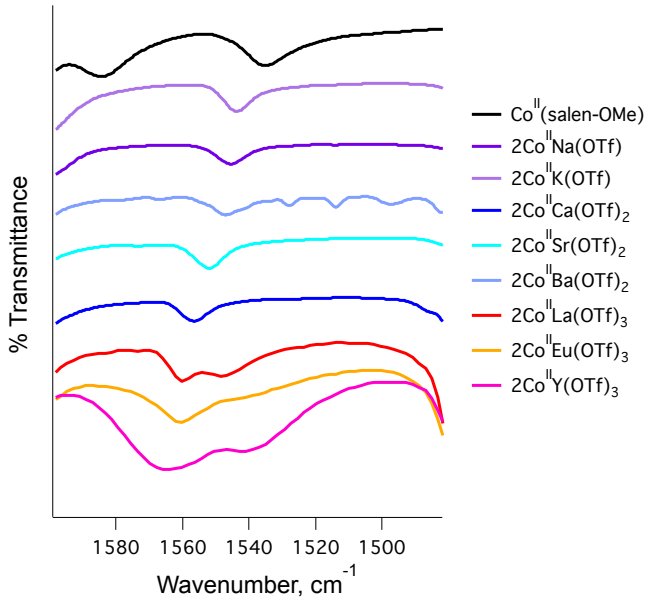


**Figure 1.7:** Overlaid infrared spectra of the C=N stretching frequency of **2Co$^{II}$M** complexes.

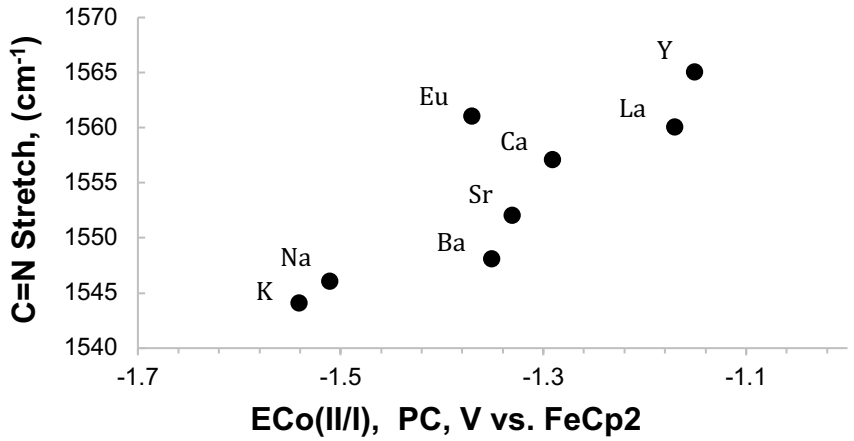


**Figure 1.8:** Infrared frequency of the C=N stretch vs. reduction potential of **2Co$^{II}$M** complexes in propylene carbonate. Due to the $Eu^{III/II}$ reduction, the IR frequency of **2Co$^{II}$Eu(OTf)$_3$** aligns with the trivalent species while its reduction potential aligns with the divalent species.

## 1.4 Conclusions

Based on the spectroscopic studies and calculated electrostatic effect of the alkali and alkaline earth metal cations, the anodic shift in the redox potential in **2Co$^{II}$M** compared to Co(salen–OMe) can largely be attributed to an electrostatic field potential. An inductive effect through the shared phenoxide ligand appears to play a smaller role. Evidence that solvent and anion interactions play an inhibiting role similar to long-range solvent dielectric screening provides further understanding of the behavior of electrostatic fields within molecular complexes.

These results highlight how cations can contribute to tuning the potential of redox-active centers through the parameters of distance and charge. Redox potentials of synthetic transition metal complexes are most commonly tuned by incorporating electron donating or withdrawing functionalities into the ligand. As a result, changes in the free energy for electron transfer are coupled to changes in the electron density of the redox active site. This study indicates cations in

the secondary coordination sphere can adjust the redox potential without significantly affecting the electronic structure at the redox active site. The decoupling of free energy and electronic structure points to their utility in mediating redox reactivity. Additionally, this work demonstrates that the use of electrostatic interactions can provide a means of modulating reduction potentials without changing steric bulk or solubility properties.

### 1.5 Experimental Details

**General Considerations:** For synthesis containing air and moisture sensitive reagents or products, manipulations were carried out in a glovebox or using standard Schlenk techniques under an inert atmosphere of nitrogen. Unless otherwise noted, all experiments were carried out at room temperature (21-24 °C). All solvents used were degassed by sparging with argon and dried by passing through columns of neutral alumina or molecular sieves. Deuterated acetonitrile was purchased from Cambridge Isotopes Laboratories, Inc. and was degassed and stored over activated 3 Å molecular sieves prior to use. Reagents were purchased from commercial vendors and used without further purification unless otherwise noted. 3,3'-(((ethane-1,2-diylbis(oxy))bis(ethane-2,1-diyl))bis(oxy))bis(2-hydroxybenzaldehyde) was synthesized according to a literature preparation[55] with the following modification. The crude product was purified by silica gel column chromatography using a ratio of ethyl acetate to hexanes of 1:1 that progressed to a ratio of 2:1.

**Physical Methods:** NMR spectra were taken on a 500 MHz Bruker Avance GN500 ($^{1}$H) with a BBO probe or on a 500 MHz Bruker DRX500 spectrometer fitted with a TCI cryoprobe ($^{13}$C) at 20 °C. Electrospray ionization mass spectrometry was performed using an ESI LC-TOF

Micromass LCT 3 mass spectrometer. Elemental analysis was taken on a PerkinElmer 2400 Series II CHNS elemental analyzer. Infrared (IR) absorption measurements were taken as thin films or compressed solids on a Thermo Scientific Nicolet iS5 spectrophotometer with an iD5 ATR attachment. UV-Vis spectra were collected in dimethylformamide solution using an Agilent Technologies Cary 60 UV−Vis.

**X-ray Crystallography.** X-ray diffraction studies were carried out at the UCI Department of Chemistry X-ray Crystallography Facility on a Bruker SMART APEX II diffractometer. Data was collected at 88 or 133 K using Mo Kα radiation (λ = 0.71073 Å). A full sphere of data was collected for each crystal structure. The APEX2[75] program suite was used to determine unit-cell parameters and to collect data. The raw frame data were processed and absorption corrected using the SAINT[76] and SADABS[77] or TWINABS[78] programs, respectively, to yield the reflection data files. Structures were solved by direct methods using SHELXS and refined against $F^2$ on all data by full-matrix least squares with SHELXTL. All non-hydrogen atoms were refined anisotropically other than the exceptions described below. For all compounds except for **2Co$^{II}$Ca(OTf)$_2$** and **2Co$^{II}$Ba(OTf)$_2$**, hydrogen atoms were placed at geometrically calculated positions and refined using a riding model, and their isotropic displacement parameters were fixed at 1.2 (1.5 for methyl groups) times the Ueq of the atoms to which they are bonded. For **2Co$^{II}$Ca(OTf)$_2$** and **2Co$^{II}$Ba(OTf)$_2$**, hydrogen atoms were located in the difference map and their positions and displacement parameters were refined freely. Additional refinement details for individual structures are described below.

Refinement details for **2Co$^{II}$Na(OTf)**: This structure exhibited whole-molecule disorder and was refined as a two-component disorder using partial site-occupancy factors. The thermal parameters of one nitrogen atom in the major part (N2) necessitated isotropic refinement. The entire triflate anion was also disordered and was also refined as a two-component disorder using partial site-occupancy factors on a separate free variable. CheckCIF reports one level B alert (PLAT201_ALERT_2_B) due to the isotropic displacement parameters for N2. As mentioned above, this atom is part of a disordered molecule and required isotropic refinement.

Refinement details for **2Co$^{II}$Na(BF$_4$)**: This structure was refined as a two-component twin. Two atoms (C19 and C20) were disordered and were refined as a two-component disorder using partial site-occupancy factors. CheckCIF reports one level B alert (PLAT410_ALERT_2_B) due to a short intramolecular H-H contact between H18B (on C18) and H19D (on C19). This is likely due to the fact that two sets of hydrogen positions were calculated for C19 while only one set was calculated for the nearby C18.

Refinement details for **2Co$^{II}$K(OTf)**: This structure contained a significantly disordered triflate anion bound to the potassium center, which was refined over two conformations ($\eta^1$ and $\eta^2$) using partial site-occupancy factors and an idealized fragment geometry (FRAG). The thermal parameters of the triflate anion were refined isotropically. Free refinement of the triflate geometry and/or anisotropic refinement of its ellipsoids did not materially change any bond lengths or angles of interest. CheckCIF reports three level B alerts: DIFMX01_ALERT_2_B and PLAT097_ALERT_2_B due to large residual electron density near the disordered triflate and PLAT201_ALERT_2_B due to the isotropic displacement parameters for the disordered triflate

anion. As mentioned above, the triflate anion was highly disordered and already modeled over two conformation; it was not deemed appropriate to model any further disorder.

Refinement details for **$2Co^{II}K(BF_4)$**: This structure has three molecules in the asymmetric unit, one of which features a disordered tetrafluoroborate anion bound to the potassium center. The fluorine atoms of the disordered $BF_4$ were refined as a two-component disorder using partial site-occupancy factors and its thermal parameters were refined isotropically. CheckCIF reports one level B alert (PLAT201_ALERT_2_B) due to the isotropic displacement parameters for the aforementioned disordered fluorine atoms.

Refinement details for **$2Co^{II}Sr(OTf)_2$**: This structure contained two disordered triflate anions, each bound to one strontium center. The fluorine atoms of each disordered $OTf^-$ anion were refined as two-component disorders using partial site-occupancy factors on separate free variables, and their thermal parameters were refined isotropically. CheckCIF reports two level B alerts: PLAT201_ALERT_2_B due to the isotropic displacement parameters for the aforementioned disordered fluorine atoms, and PLAT971_ALERT_2_B due to a residual electron density peak of 2.77 e-/$Å^3$ 0.86 Å from the strontium center.

Refinement details for **$2Co^{II}Ba(OTf)_2$**: CheckCIF reports one level B alert (PLAT391_ALERT_3_B) due to an unusual H-C-H angle on a methyl moiety (119° instead of 109° on C24). This is likely due to the hydrogen atom positions being found in the difference map and refined freely.

Refinement details for Co(salen-OMe): CheckCIF reports one level B alert (PLAT112_ALERT_2_B) due to ADDSYM detecting a possible new *C2* symmetry element; this was determined to be the result of pseudosymmetry.

Refinement details for **2Co$^{II}$Y(OTf)$_3$**: CheckCIF reports no alerts for level B or higher. The structure was solved by direct methods and refined on $F^2$ by full-matrix least-squares techniques. The analytical scattering factors[79] for neutral atoms were used throughout the analysis. Hydrogen atom H(7) was located from a difference-Fourier map and refined (x,y,z) with d(O-H) = 0.85Å. The remaining hydrogen atoms were included using a riding model. There was one molecule of methanol solvent present. The solvent was disordered and included using multiple components with partial site-occupancy-factors.

Refinement details for **2Co$^{II}$Eu(OTf)$_3$**: CheckCIF reports no alerts for level B or higher. The structure was solved by direct methods and refined on $F^2$ by full-matrix least-squares techniques. The analytical scattering factors[5] for neutral atoms were used throughout the analysis. Hydrogen atom H(7) was located from a difference-Fourier map and refined (x,y,z and $U_{iso}$) with d(O-H) = 0.85Å. The remaining hydrogen atoms were included using a riding model. There was one-half molecule of diethyl ether solvent present. Several atoms were disordered and included using multiple components with partial site-occupancy-factors.

Refinement details for **2Co$^{II}$La(OTf)$_3$**: CheckCIF reports no alerts for level B or higher. The structure was solved by direct methods and refined on $F^2$ by full-matrix least-squares techniques. The analytical scattering factors[5] for neutral atoms were used throughout the analysis. Hydrogen atom H(7) was located from a difference-Fourier map and refined (x,y,z

and $U_{iso}$) with d(O-H) = 0.85Å. The remaining hydrogen atoms were included using a riding model. There was one-half molecule of diethyl ether solvent present. The solvent was disordered about an inversion center and refined with equivalent anisotropic displacement parameters. Atoms O(17), C(27), C(28), C(29) and C(30) were included with site-occupancy-factors = 0.50. Carbon atom C(23) was disordered and included using multiple components with partial site-occupancy-factors.

**Electrochemical procedures:** All measurements were performed on a Pine Wavedriver 10 bipotentiostat with a 2 mm diameter glassy carbon disc working electrode, a glassy carbon counter electrode, and a $Ag/Ag^+$ psuedoreference electrode separated from the bulk solution by a Vicor frit. Potentials were referenced to a ferrocene internal standard at 0 V, and all experiments were performed in dry, degassed DMF, PC, or THF at a concentration of 5 mM analyte and 0.5 M tetrabutylammonium hexafluorophosphate and at a 100 mV/s scan rate unless otherwise noted.

**Synthetic Procedures:**

**Scheme 1.1:** Synthesis of **1M** complexes

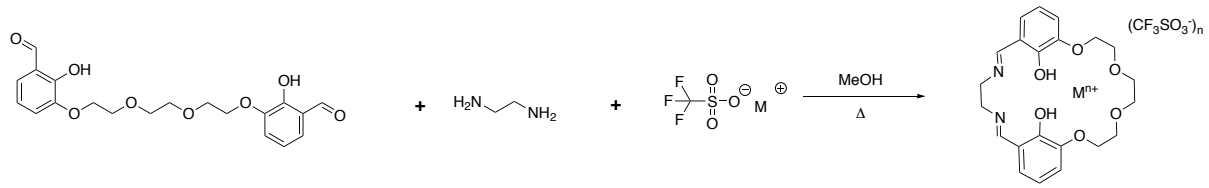


**Method 1a Synthesis of 1M (M= $Na^+$, $K^+$, $Ca^{2+}$. $Sr^{2+}$, $Ba^{2+}$):** This procedure is based on the literature procedure[55] for Ba(18-crown-6-salen)$(CF_3SO_3)_2$ (**1Ba(OTf)$_2$**). 1 equivalent of 3,3'-(((ethane-1,2-diylbis(oxy))bis(ethane-2,1-diyl))bis(oxy))bis(2-hydroxybenzaldehyde) was added to 1 equivalent of the respective M triflate salt in refluxing methanol and stirred until dissolved.

5 mM ethylene diamine in methanol was slowly added to the reaction mixture via syringe pump over 2-4 hours using an addition funnel, forming a bright yellow product. Solvent and any excess ethylene diamine were removed *in vacuo* to give a yellow solid. The crude product was taken up in a minimal amount of methanol and filtered through a glass microfiber filter. Diethyl ether was layered over the methanol solution. The pure product precipitated as yellow crystals, and was isolated by filtration and washing with diethyl ether.

**1Na(OTf)** was synthesized using method 1a with 3,3'-(((ethane-1,2-diylbis(oxy))bis(ethane-2,1-diyl))bis(oxy))bis(2-hydroxybenzaldehyde) (0.379 g, 0.916 mmol), ethylene diamine (0.055 g, 0.92 mmol) and Na($CF_3SO_3$) (0.158 g, 0.918 mmol) to give 0.390 g of product (67% yield). ESI mass spectrometry: [**1Na-**($CF_3SO_3$)]$^+$: calculated m/z: 437.1689. Found: 437.1682.$^1$H NMR (500 MHz, $CD_3CN$) δ 14.89 (s, 2H), 8.57 (s, 2H), 7.03 (m, 4H), 6.77 (m, 2H), 4.15 (m, 4H), 3.92 (s, 4H), 3.87 (s, 4H), 3.76 (s, 4H). $^{13}$C NMR (500 MHz, $CD_3CN$) δ 166.65, 156.91, 148.18, 123.93, 116.47, 114.86, 69.89, 68.66, 67.09, 55.38.

**1K(OTf)** was synthesized using method 1a with 3,3'-(((ethane-1,2-diylbis(oxy))bis(ethane-2,1-diyl))bis(oxy))bis(2-hydroxybenzaldehyde) (0.340 g, 0.870 mmol), ethylene diamine (0.052 g, 0.87 mmol, 1 eq.) and K($CF_3SO_3$) (0.163 g, 0.870 mmol) to give 0.451 g of product (79% yield). ESI mass spectrometry: [**2CoK(OTf)-**($CF_3SO_3$)]$^+$: calculated m/z: 453.1428. Found: 453.1414. $^1$H NMR (500 MHz, $CD_3CN$) δ 15.23 (s, 2H), 8.58 (s, 2H), 7.02 (m, 4H), 6.77 (m, 2H), 4.18 (m, 4H), 3.90 (s, 4H), 3.88 (s, 4H), 3.76 (s, 4H). $^{13}$C NMR (500 MHz, $CD_3CN$) δ 166.85, 156.61, 148.15, 123.63, 116.50, 113.83, 70.41, 69.10, 66.82, 55.66.

**1Ca(OTf)$_2$** was synthesized using method 1a with 3,3'-(((ethane-1,2-diylbis(oxy))bis(ethane-2,1-diyl))bis(oxy))bis(2-hydroxybenzaldehyde) (0.309 g, 0.792 mmol), ethylene diamine (0.048 mg, 0.800 mmol), and $Ca(CF_3SO_3)_2$ (0.267 g, 0.792 mmol) to give 0.402 g of product (yield 53%). ESI mass spectrometry: Calculated m/z for [**1Ca-**$(CF_3SO_3)]^+$: 603.0937. Found: 603.0939. $^1$H NMR (500 MHz, $CD_3CN$) δ 14.96(s, 2H), 8.55 (s, 2H), 7.15 (d, 2H), 7.09 (d, 2H), 6.68 (m, 2H), 4.30 (s, 4H), 4.06 (s, 4H), 4.00 (m, 8H). $^{13}$C NMR (500 MHz, $CD_3CN$) δ 168.32, 126.06, 117.92, 114.77, 69.63, 68.70, 67.90, 51.74.

**1Sr(OTf)$_2$** was synthesized using method 1a with 3,3'-(((ethane-1,2-diylbis(oxy))bis(ethane-2,1-diyl))bis(oxy))bis(2-hydroxybenzaldehyde) (0.073 g, 0.19 mmol), ethylene diamine (.012 g, 0.20 mmol), and $Sr(CF_3SO_3)_2$ (0.072 g, 0.19 mmol). Yield: 0.110 g, 73%. ESI mass spectrometry: Calculated m/z for [**1Sr**-H-$(CF_3SO_3)_2]^+$: 501.0771. Found: 501.0791. $^1$H NMR (500 MHz, $CD_3CN$) δ 15.18 (s, 2H), 8.55 (s, 2H), 7.09 (m, 4H), 6.70 (m, 2H), 4.29 (d, 4H), 4.07 (d, 4H), 3.99 (s, 4H), 3.95 (s, 4H). $^{13}$C NMR (500 MHz, $CD_3CN$) δ 168.02, 125.04, 122. 01, 119.47, 115.09, 70.28, 68.92, 66.57, 52.73.

**1Ba(OTf)$_2$** was synthesized using a literature procedure.[55] ESI mass spectrometry: Calculated m/z for [**1Ba**-H-$(CF_3SO_3)_2]^+$: 551.0767. Found: 551.0851. $^1$H NMR (500 MHz, $CD_3CN$) δ 15.39 (s, 2H), 8.56 (s, 2H), 7.07 (m, 4H), 6.68 (m, 2H), 4.28 (d, 4H), 4.01 (d, 8H), 3.89 (s, 4H). $^{13}$C NMR (500 MHz, $CD_3CN$) δ 168.12, 163.13, 149.38, 125.07, 115.05, 70.57, 69.55, 66.76, 52.62.

**Method 1b. Synthesis of $M^{3+}$(18-crown-6-salen) (M = Y(OTf)$_3$, La(OTf)$_3$, Eu(OTf)$_3$):** In a dealkalized 500 mL flask, Ba(18-crown-6-salen)$(OTf)_2$ (685 mg, .755 mmol) was added to 80 mL $CHCl_3$ to form a yellow suspension. Next, guanidine sulfate (435 mg, 4.02 mmol) was added to

80 mL nanopure $H_2O$. The mixture was stirred extremely vigorously for one hour, and the organic layer was separated, quickly dried with $Mg(SO_4)$, and filtered. Solvent was removed *in vacuo* to leave a yellow, foamy semisolid, which is subsequently dissolved in a minimal amount of hot $CHCl_3$, and a hot MeOH solution of $M^{3+}(OTf)_3$ is quickly added. This solution is stirred for approximately 30 minutes, during which the reaction mixture changes from cloudy yellow to clear yellow. Solvent is then removed *in vacuo*, and the yellow solid is then crystallized by layering diethyl ether onto a saturated methanol solution. Dealkalation of glassware was carried out by washing with 1 M $HNO_3$ followed by copious rinsing with nanopure water.

**1Y(OTf)$_3$:** Yield: 45% ESI mass spectrometry: Calculated m/z for **1Y:** 800.9890. Found: 800.9878. $^1$H NMR (500 MHz, $CD_3CN$) δ 13.58 (s, 1H), 8.62 (d, *J* = 13.97 Hz, 2H), 7.40 (dd, *J* = 1.36, 7.82, 4H), 7.25(dd, *J* = 1.36, 8.14, 2H), 6.77 (t, *J* =7.97, 2H), 4.63 (m, 4H), 4.10 (m, 8H), 3.96 (m, 4H).

**1Eu(OTf)$_3$:** Yield: 55% ESI mass spectrometry: Calculated m/z for **1Eu:** 865.0042 Found: 865.0016.

**1La(OTf)$_3$:** Yield: 52% ESI mass spectrometry: Calculated m/z for **1La:** 850.9895. Found: 850.9883. $^1$H NMR (500 MHz, $CD_3CN$) δ 13.50 (s, 1H), 8.59 (dd, *J* = 1.30, 13.77, 2H), 7.19 (dd, *J* = 1.33, 8.14, 2H), 6.77 (t, *J* = 7.97, 2H), 4.48 (m, 4H), 4.27 (m, 4H), 4.19 (s, 4H), 4.07 (d, *J* = 5.90).

**Method 1.2. General procedure for synthesis of 2Co$^{II}$M:** In an inert atmosphere glovebox, 1 equivalent of **1M** (M = Na(OTf), K(OTf), $Ca(OTf)_2$, $Sr(OTf)_2$, $Ba(OTf)_2$, $Y(OTf)_3$, $La(OTf)_3$, $Eu(OTf)_3$) was dissolved in refluxing methanol. 1 equivalent of $Co(OAc)_2$ was added dropwise

in a concentrated methanol solution over several minutes, and the reaction was refluxed for ten minutes. The crude red product was isolated under reduced pressure at 80 °C, re-dissolved in methanol, and passed through a glass microfiber filter. Vapor diffusion of diethyl ether into the methanol solution precipitated the product as deep red crystals, which were isolated by filtration and washed with diethyl ether.

**$2Co^{II}Na(OTf)$** was synthesized using method 1.2 with **1Na(OTf)** (0.092 g, 0.16 mmol) and $Co(OAc)_2$ (0.028 g, 0.16 mmol) to give 0.091 g product (90% yield). ESI mass spectrometry: Calculated m/z for (**2CoNa(OTf)-$CF_3SO_3$]**$^+$: 494.0. Found: 494.1 Analytical calculation for $C_{23}H_{24}NaCoF_3O_9N_2S$: C, 42.93; H, 3.76; N, 4.35. Found: C, 43.08; H, 3.46; N, 4.26.

**$2Co^{II}K(OTf)$** was synthesized using method 1.2 with **1K(OTf)** (0.220 g, 0.333 mmol) and $Co(OAc)_2$ (0.059 g, 0.33 mmol) to give the 0.195 g (89% yield). ESI mass spectrometry: Calculated m/z for **2CoK(OTf)** •$(CH_3OH)^+$: 542.1. Found: 542.0. Analytical calculation for $C_{23}H_{24}KCoF_3O_9N_2S$: C, 41.88; H, 3.67; N, 4.25. Found: C, 41.61; H, 3.36; N, 4.21.

**$2Co^{II}Ca(OTf)_2$** was synthesized using method 2 with **$1Ca(OTf)_2$** (0.059 g, 0.078 mmol) and $Co(OAc)_2$ (0.014 g, 0.078 mmol) to give 0.056 g product (89% yield). ESI mass spectrometry: Calculated m/z for **2CoCa•**$(C_2H_3O_2)^+$: 719.03. Found 718.96. Analytical calculation for $C_{24}H_{24}CaCoF_6O_{12}N_2S_2$: C, 35.61; H, 2.99; N, 3.46. Found: C, 35.30; H, 2.83; N, 3.40.

**$2Co^{II}Sr(OTf)_2$** was synthesized using method 2 with **$1Sr(OTf)_2$** (0.020 g, 0.025 mmol) and $Co(OAc)_2$ (0.006 g, 0.03 mmol) to give 0.018 g product (80% yield). ESI mass spectrometry: calculated m/z for **2CoSr**$^+$: 707.954. Found: 707.953. Analytical calculation for $C_{24}H_{24}SrCoF_6O_{12}N_2S_2$: C, 33.63; H, 2.82; N, 3.27. Found: C, 33.37; H, 2.64; N, 3.24.

**2Co$^{II}$Ba(OTf)$_2$** was synthesized using method 2 with **1Ba(OTf)$_2$** (0.180 g, 0.20 mmol) and $Co(OAc)_2$ (0.035 g, 0.20 mmol) to give 0.156 g product (88% yield). ESI mass spectrometry: calculated m/z for **2CoBa**$^+$ : 758.0. Found: 757.9. Analytical calculation for $C_{24}H_{24}BaCoF_6O_{12}N_2S_2$: C, 31.79; H, 2.67; N, 3.0. Found: C, 31.95; H, 2.83; N, 3.05.

**2Co$^{II}$Y(OTf)$_3$** was synthesized using method 2 with **1Y(OTf)$_3$** (24.7 mg, 0.026 mmol) and $Co(OAc)_2$ (4.6 mg, 0.026 mmol) to give 22 mg product (84% yield). Analytical calculation for $C_{25}H_{24}YCoF_9O_{15}N_2S_3$: C, 29.80; H 2.40; N, 2.78. Found: C, 30.03; H, 2.90; N, 2.58.

**2Co$^{II}$Eu(OTf)$_3$** was synthesized using method 2 with **1Eu(OTf)$_3$** (36.0 mg, 0.036 mmol) and $Co(OAc)_2$ (6.3 mg, 0.036 mmol) to give 30.1 mg product (80% yield). Analytical calculation for $C_{25}H_{24}EuCoF_9O_{15}N_2S_3$: C, 28.05; H 2.26; N, 2.62. Found: C, 28.46; H, 2.74; N, 2.51.

**2Co$^{II}$La(OTf)$_3$** was synthesized using method 2 with **1La(OTf)$_3$** (70.2 mg, 0.070 mmol) and $Co(OAc)_2$ (12.4 mg, 0.070 mmol) to give 68 mg product (91% yield). Analytical calculation for $C_{25}H_{24}LaCoF_9O_{15}N_2S_3$: C, 28.40; H 2.29; N, 2.65. Found: C, 29.33; H, 3.27; N, 2.41.

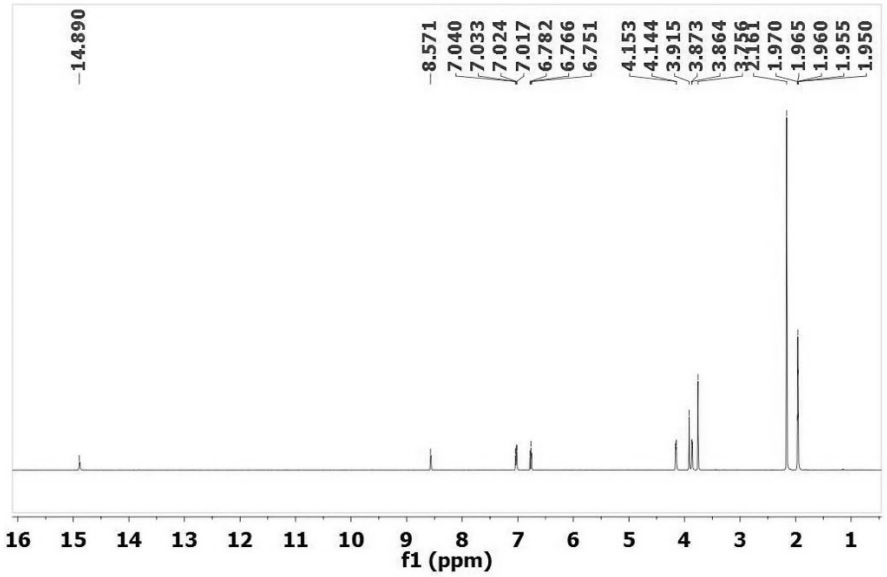


**Figure 1.9:** $^{1}H$ NMR spectra of **1Na(OTf)** in $CD_3CN$.

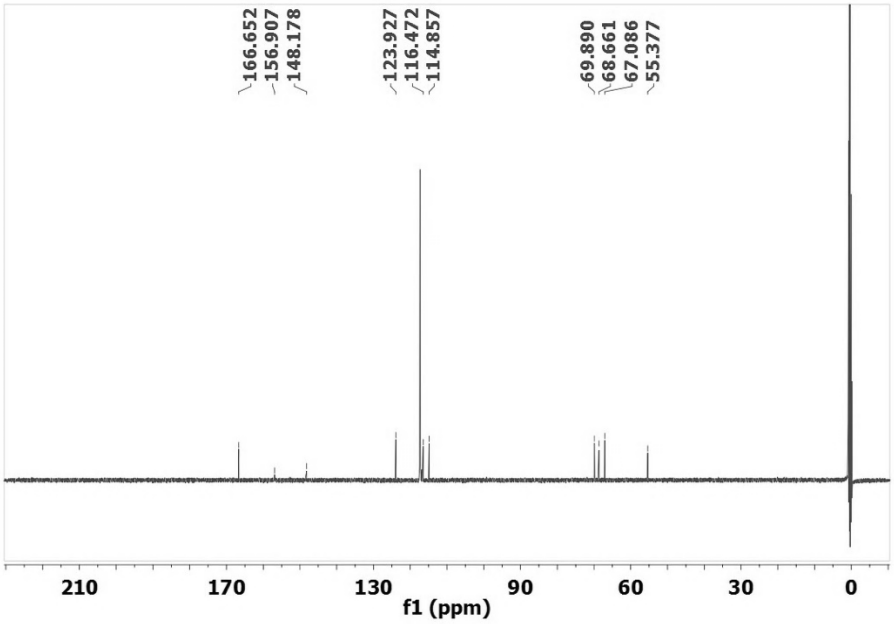


**Figure 1.10:** $^{13}C$ NMR spectrum of **1Na(OTf)** in $CD_3CN$.

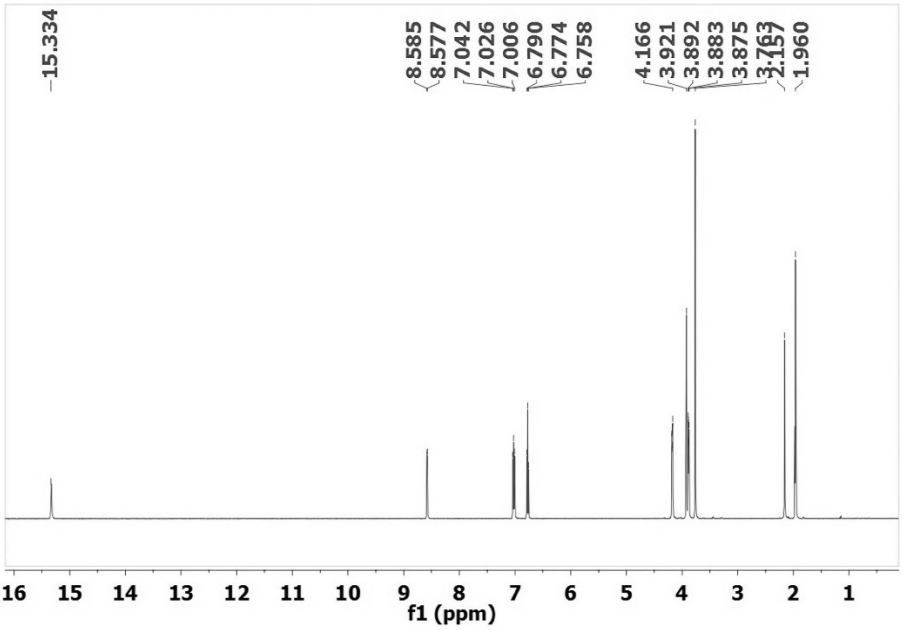


**Figure 1.11:** $^{1}$H NMR spectra of **1K(OTf)** in $CD_3CN$.

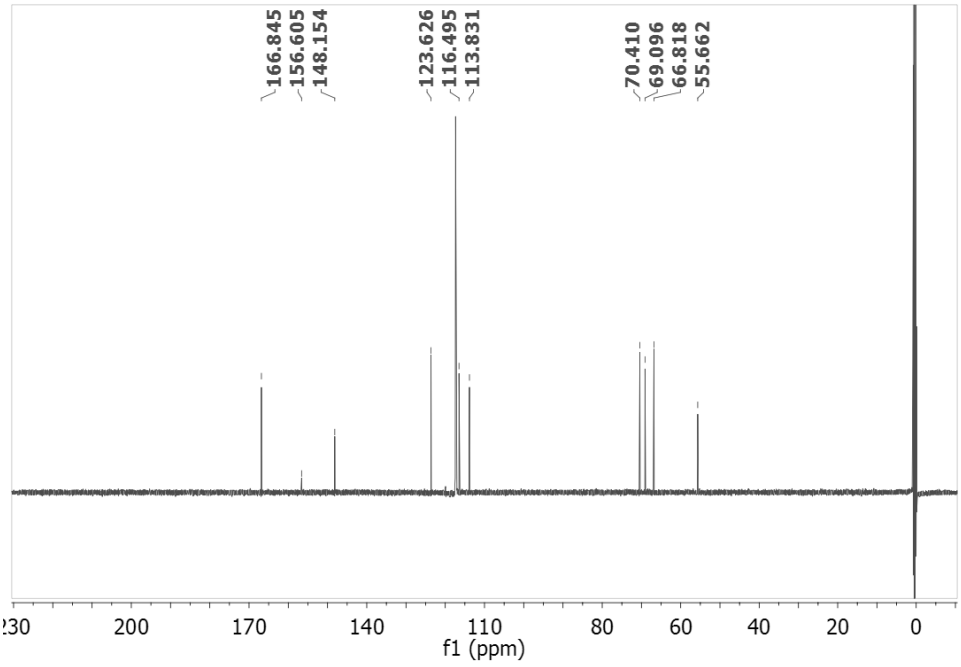


**Figure 1.12:** $^{13}$C NMR spectrum of **1K(OTf)** in $CD_3CN$.

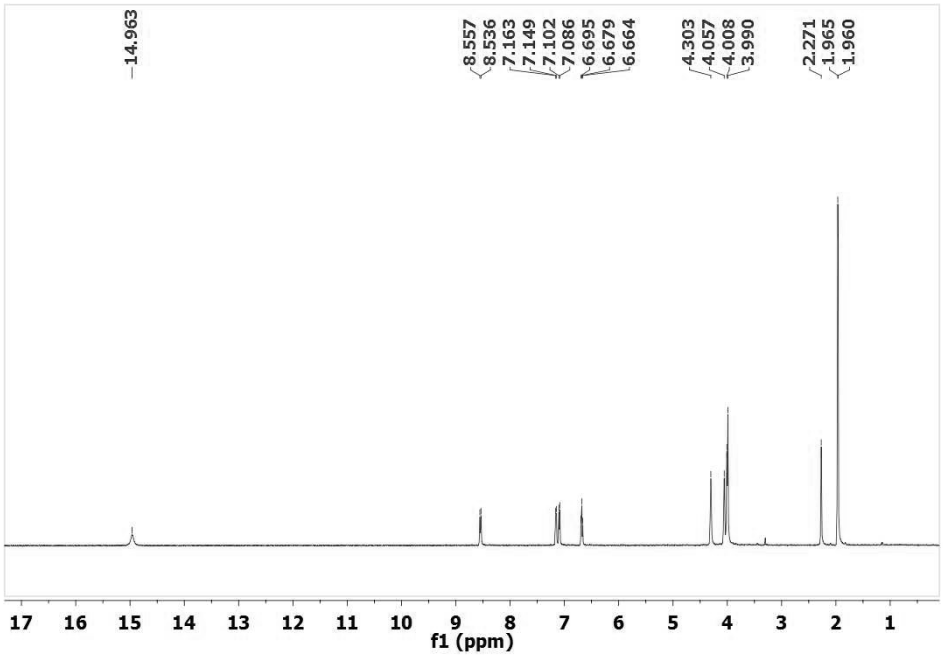


**Figure 1.13:** $^{1}$H NMR spectra of **1Ca(OTf)$_2$** in $CD_3CN$.

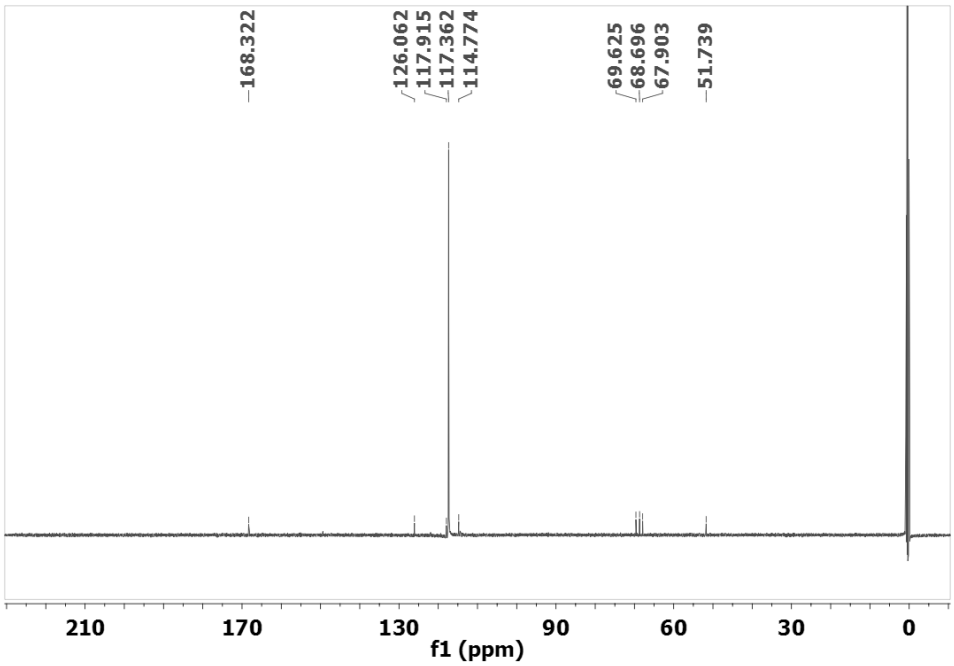


**Figure 1.14:** $^{13}$C NMR spectrum of **1Ca(OTf)$_2$** in $CD_3CN$

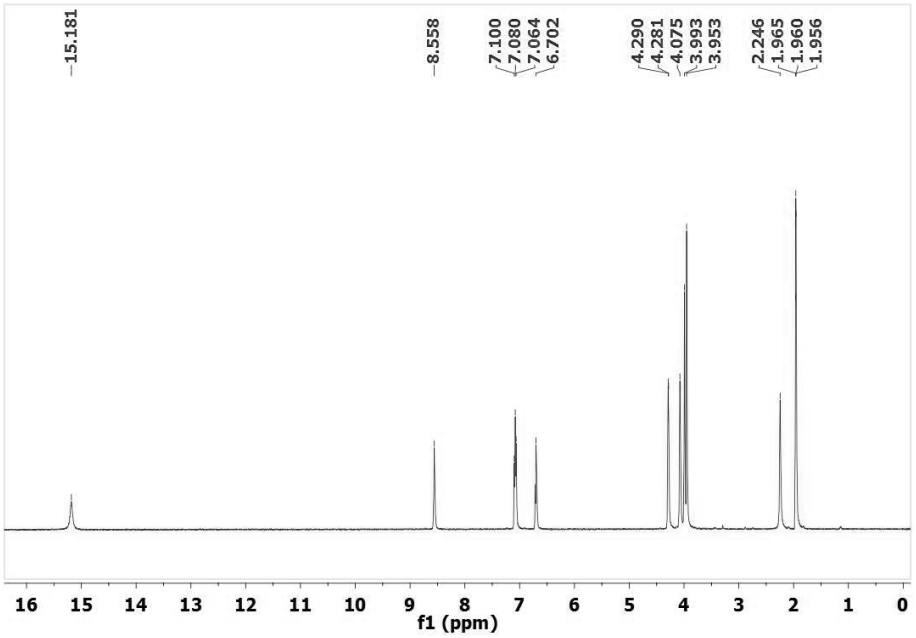


**Figure 1.15:** $^{1}$H NMR spectra of **1Sr(OTf)$_2$** in $CD_3CN$.

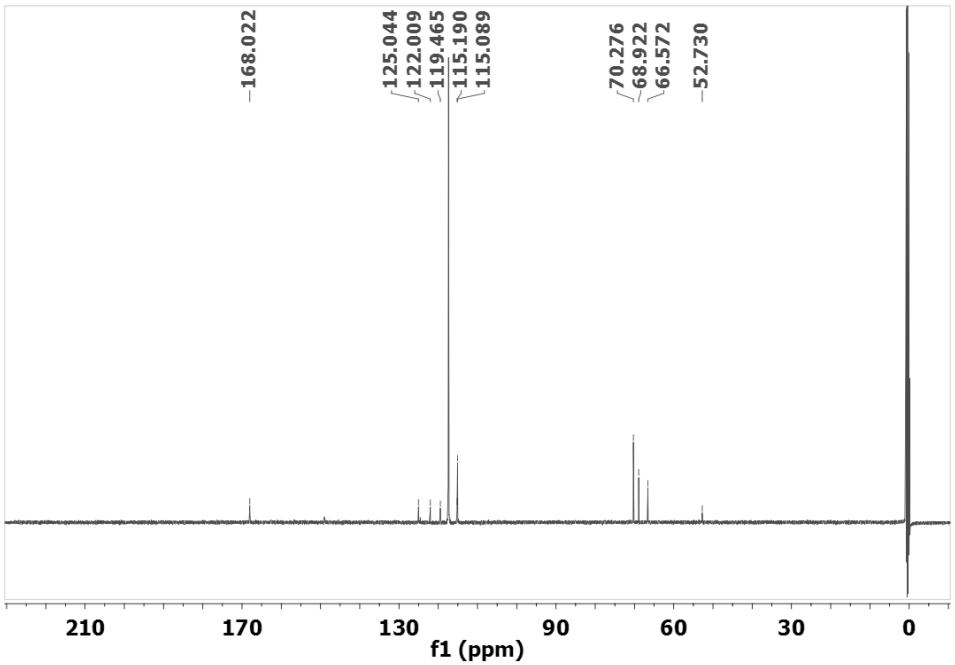


**Figure 1.16:** $^{13}$C NMR spectrum of **1Sr(OTf)$_2$** in $CD_3CN$.

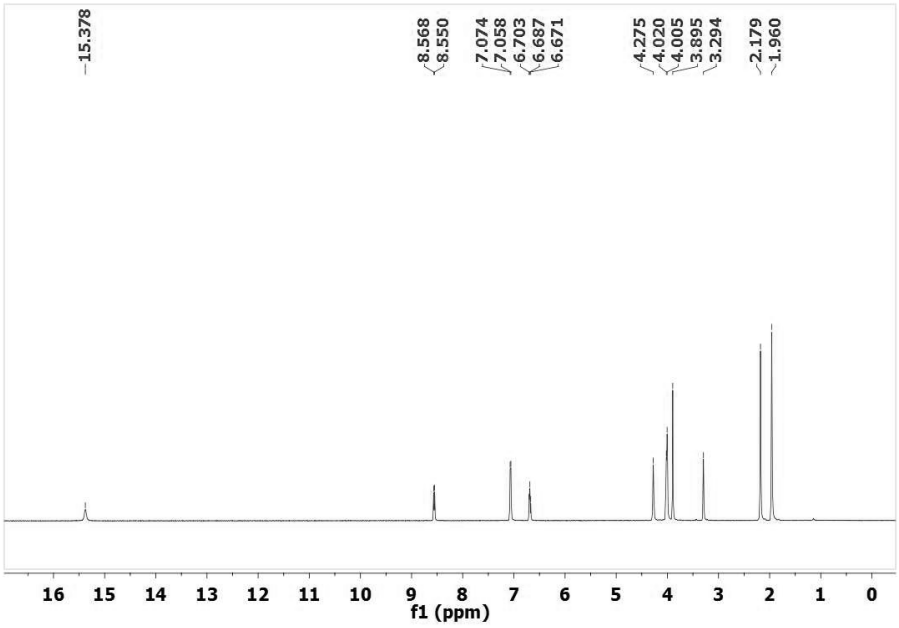


**Figure 1.17:** $^{1}$H NMR spectra of **1Ba(OTf)$_2$** in $CD_3CN$.

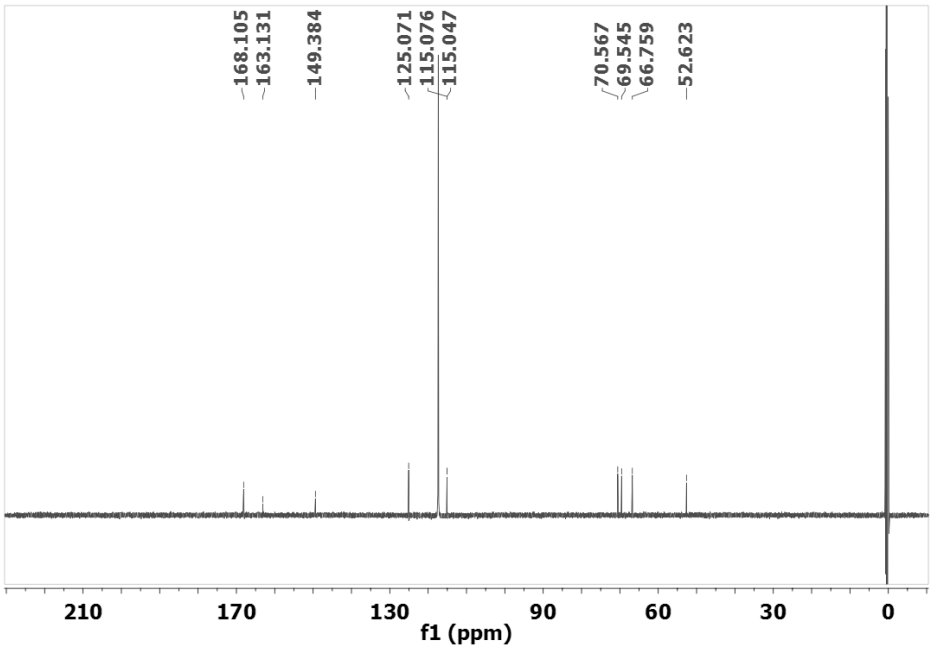


**Figure 1.18:** $^{13}$C NMR spectrum of **1Ba(OTf)$_2$** in $CD_3CN$.

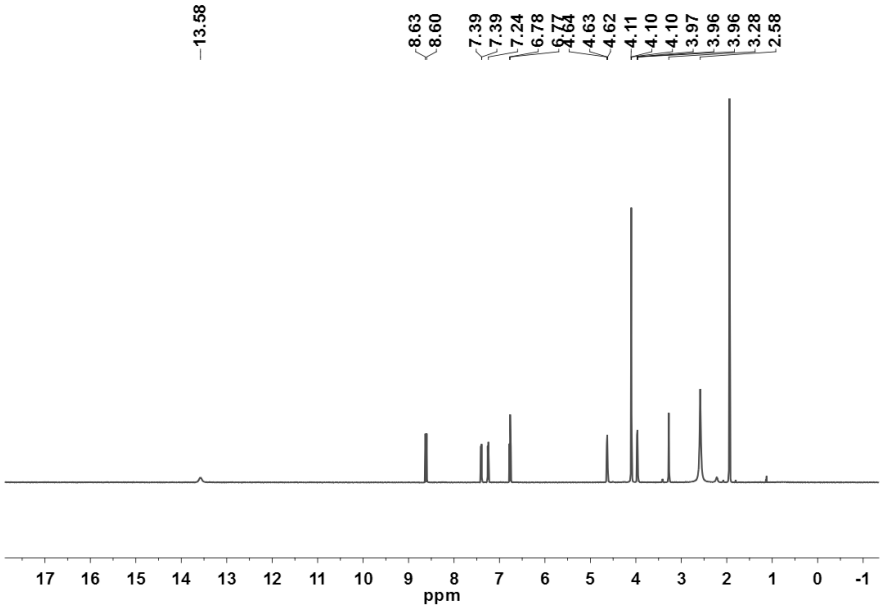


**Figure 1.19:** $^{1}$H NMR spectra of **1Y(OTf)$_3$** in $CD_3CN$.

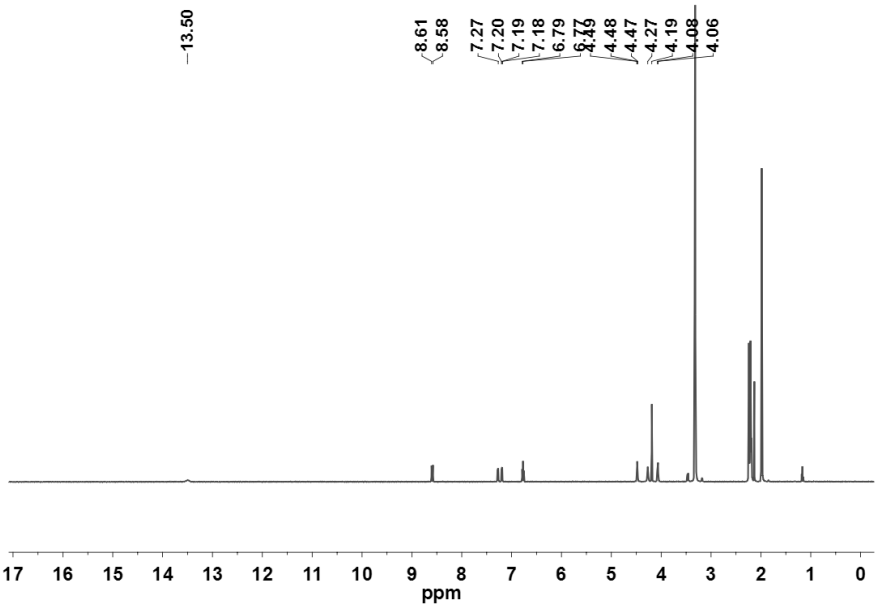


**Figure 1.20:** $^{1}$H NMR spectra of **1La(OTf)$_3$** in $CD_3CN$.

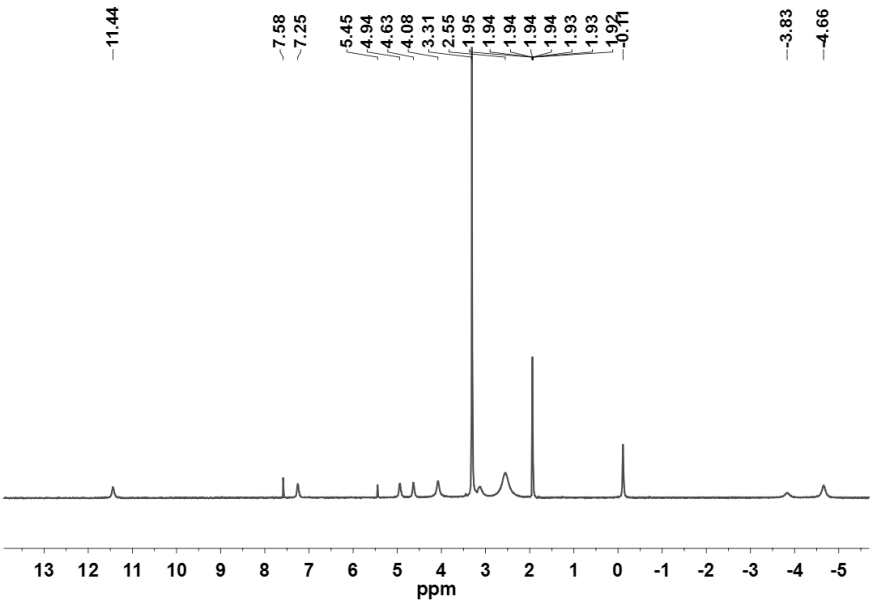


**Figure 1.21:** $^{1}$H NMR spectra of **1Eu(OTf)$_3$** in $CD_3CN$.

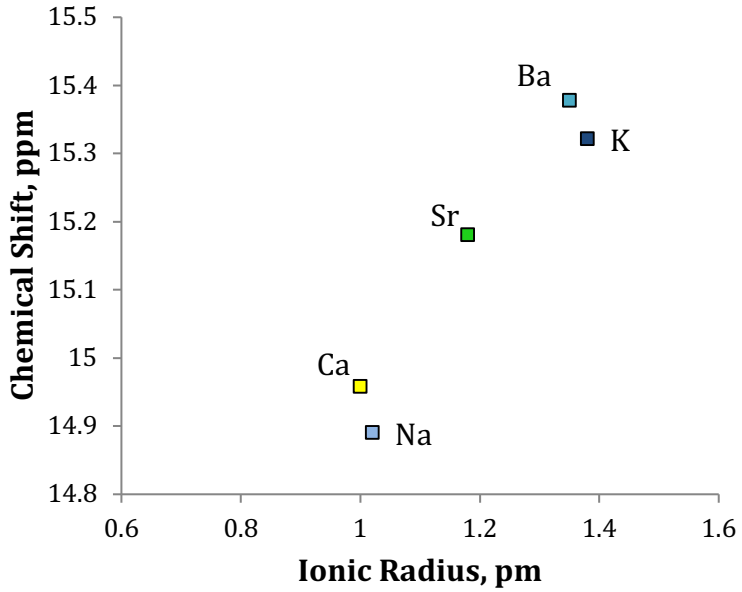


**Figure 1.22:** Effect of ionic radius of the occupied cation on the chemical shift of the phenolic protons in the **1M** complexes

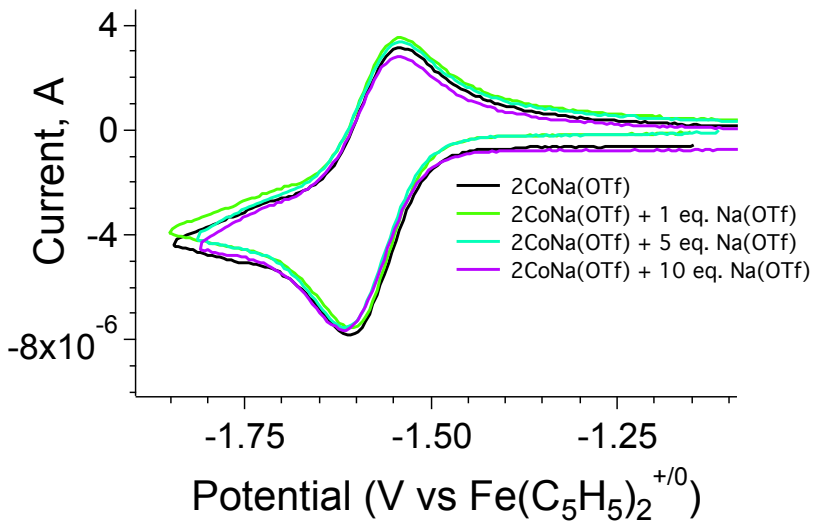


**Figure 1.23:** Cyclic voltammograms from the titration of **2CoNa(OTf)** with excess Na(OTf) at a scan rate of 250 mV/s.

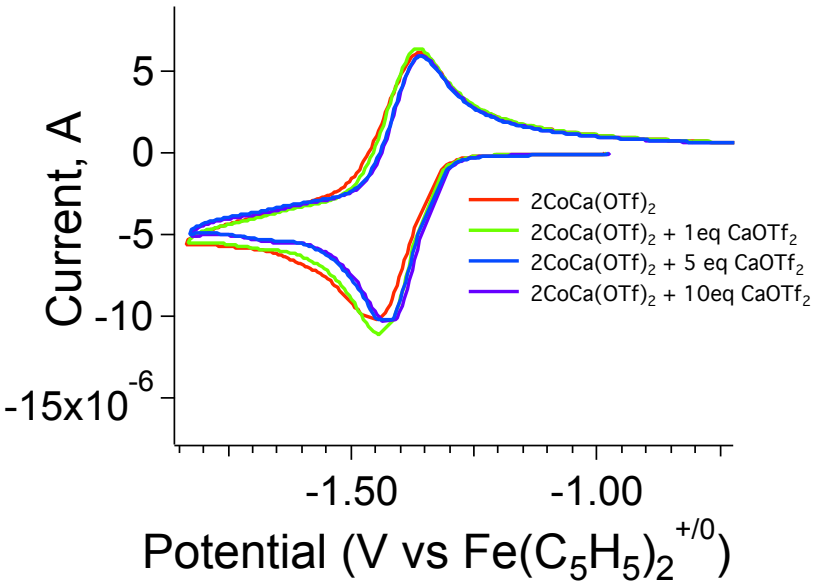


**Figure 1.24:** Cyclic voltammograms from the titration of **2CoCa(OTf)**$_2$ with excess Ca(OTf)$_2$ at a scan rate of 250 mV/s.

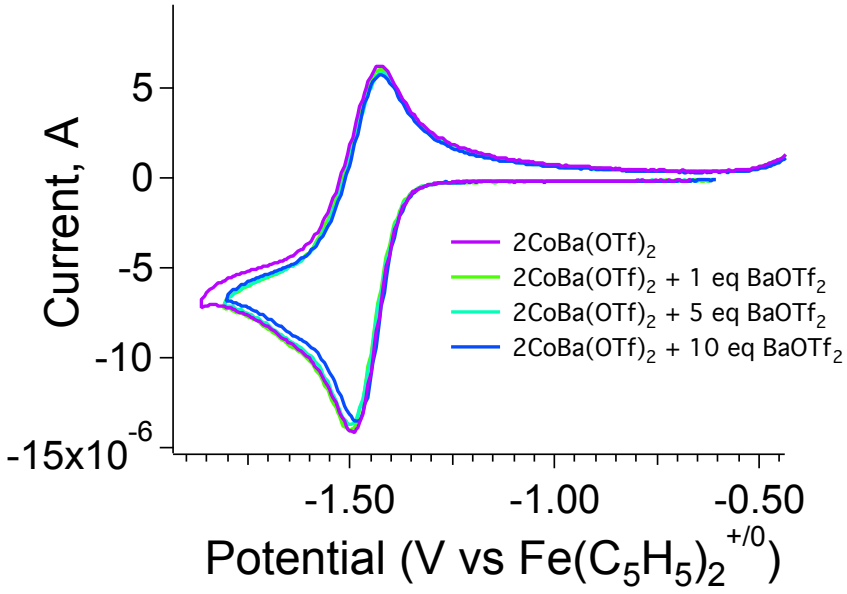


**Figure 1.25:** Cyclic voltammograms from the titration of **2CoBa(OTf)$_2$** with excess Ba(OTf)$_2$ at a scan rate of 250 mV/s.

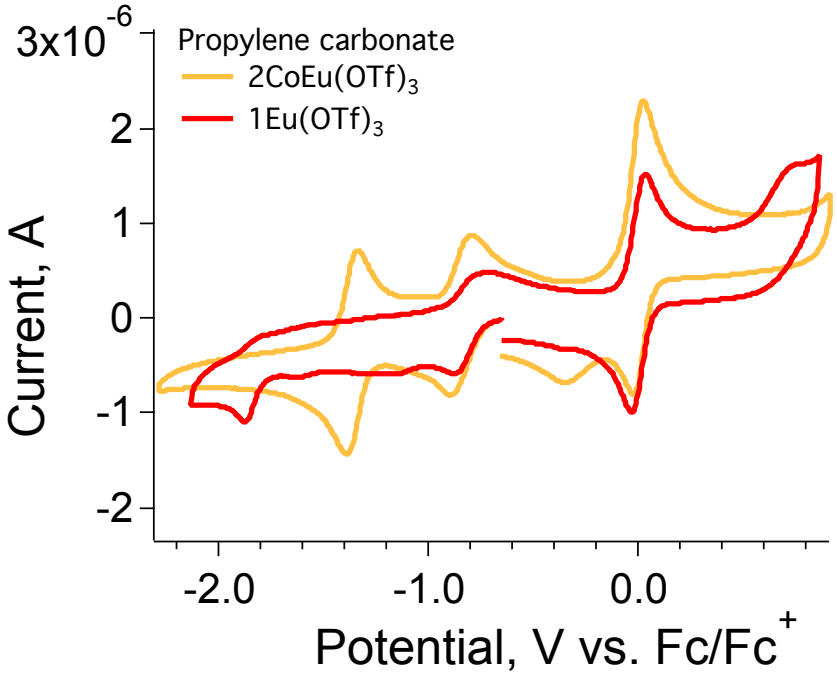


**Figure 1.26:** Cyclic voltammograms of **1Eu(OTf)$_3$** and **2Co$^{II}$Eu(OTf)$_3$** in propylene carbonate.

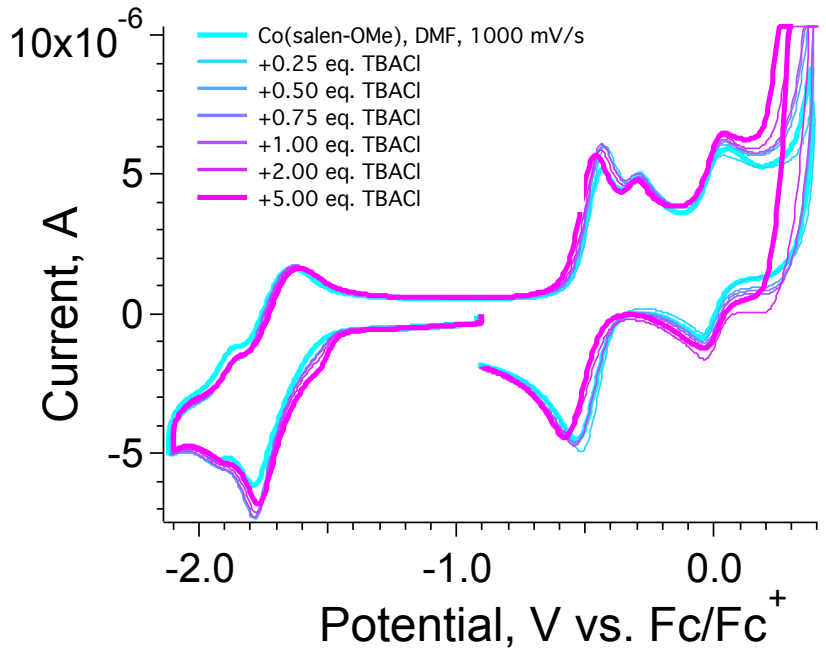


**Figure 1.27:** Cyclic voltammograms from the titration of Co(salen-OMe) with tetrabutylammonium chloride in dimethylformamide.

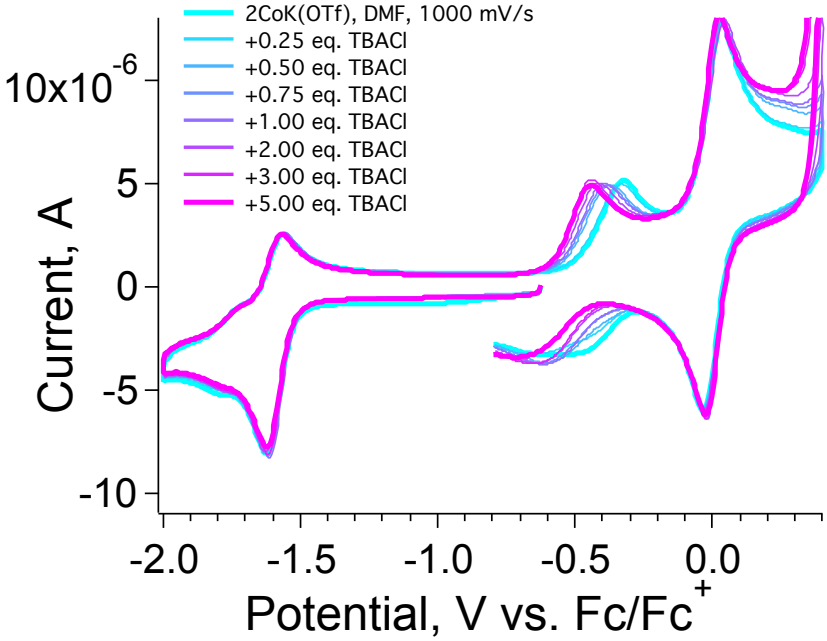


**Figure 1.28:** Cyclic voltammograms from the titration of **2CoK(OTf)** with tetrabutylammonium chloride in dimethylformamide.

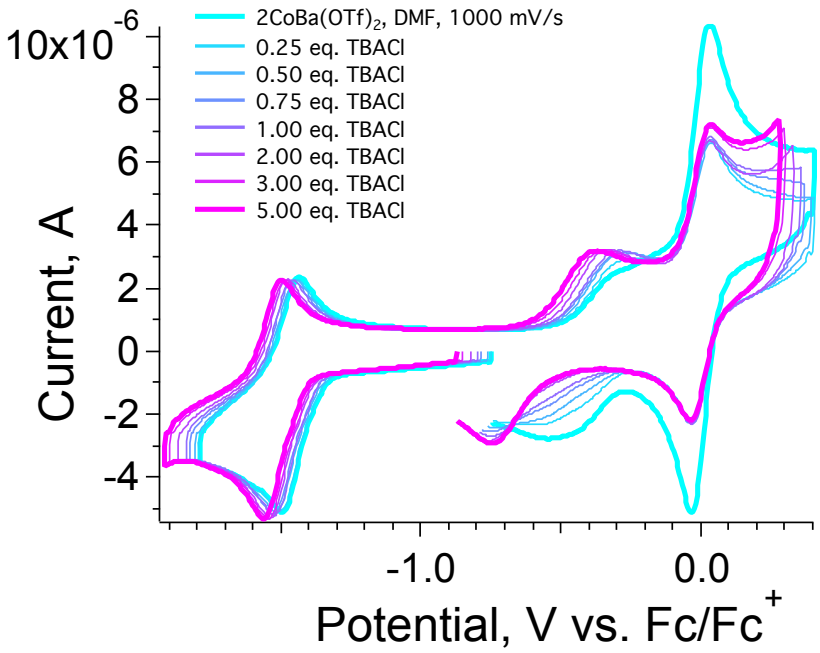


**Figure 1.29:** Cyclic voltammograms from the titration of **2CoBa(OTf)$_2$** with tetrabutylammonium chloride in dimethylformamide.

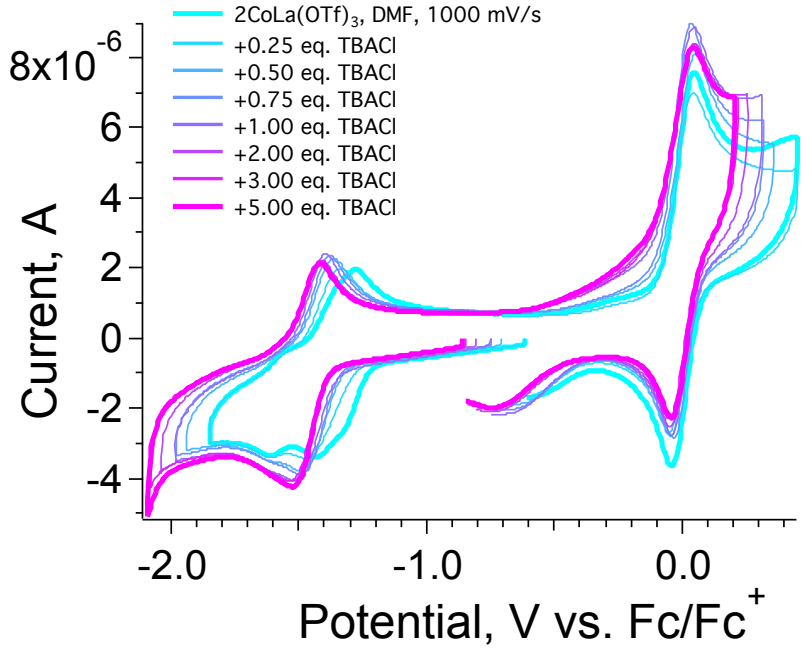


**Figure 1.30:** Cyclic voltammograms from the titration of **2CoLa(OTf)$_3$** with tetrabutylammonium chloride in dimethylformamide.

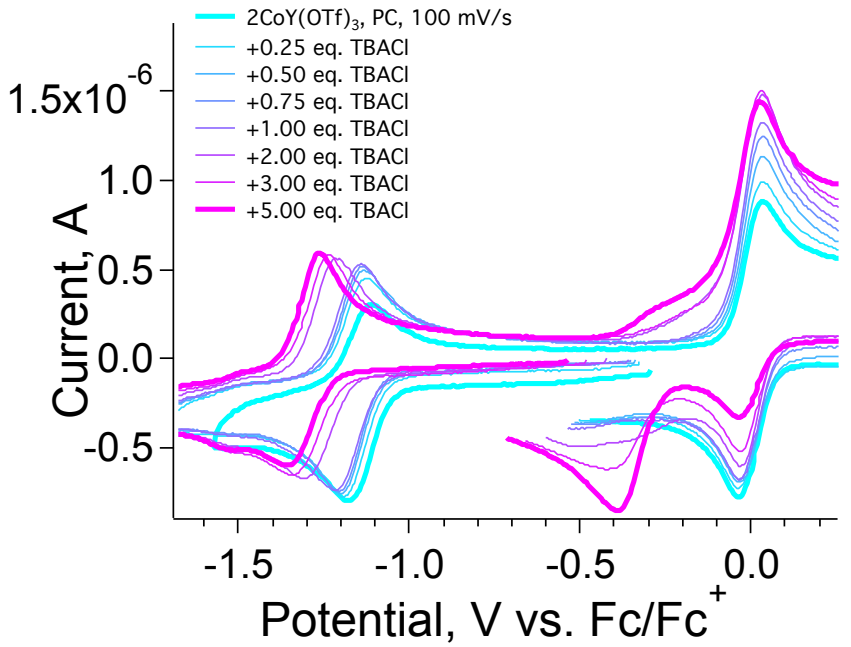


**Figure 1.31:** Cyclic voltammograms from the titration of **2CoY(OTf)$_3$** with tetrabutylammonium chloride in propylene carbonate.

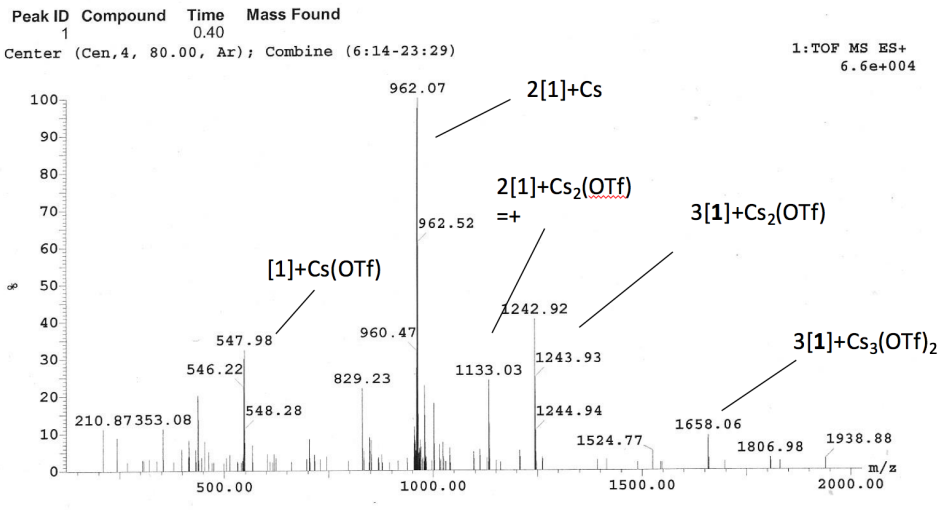


**Figure 1.32:** Electrospray ionization mass spectrum of the product isolated by Method 1a using Cs(OTf).

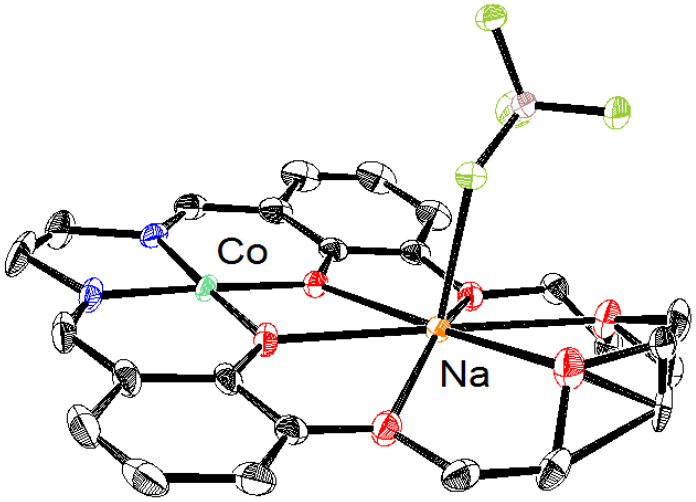


**Figure 1.33:** ORTEP of **2Co$^{II}$Na(BF$_4$)**. Thermal ellipsoids are drawn to 50% probability. Hydrogen atoms and outersphere anions and solvent molecules have been omitted for clarity.

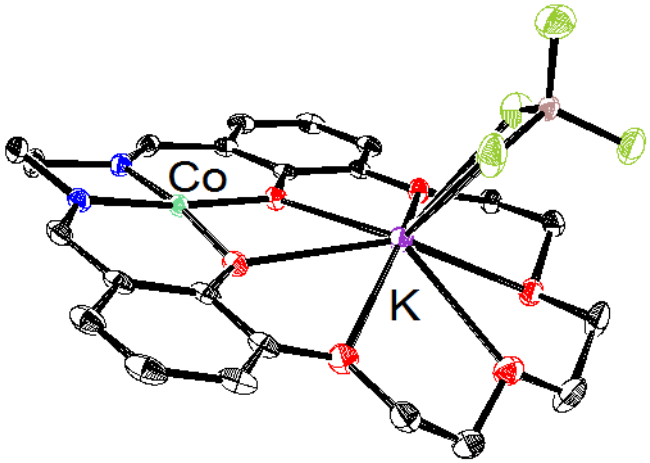


**Figure 1.34:** ORTEP of **2Co$^{II}$K(BF$_4$)**, depicting one of three molecules in the unit cell. Thermal ellipsoids are drawn to 50% probability. Hydrogen atoms and outersphere anions and solvent molecules have been omitted for clarity.

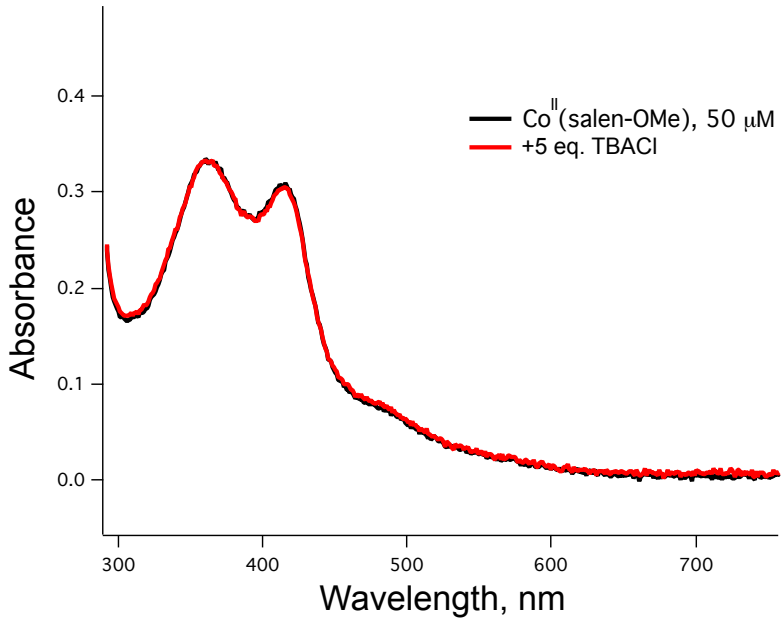


**Figure 1.35:** UV-Vis spectra from the titration of $Co^{II}$(salen)OMe with tetrabutylammonium chloride in propylene carbonate. Spectra were taken at 50 μM in a 1 cm cuvette.

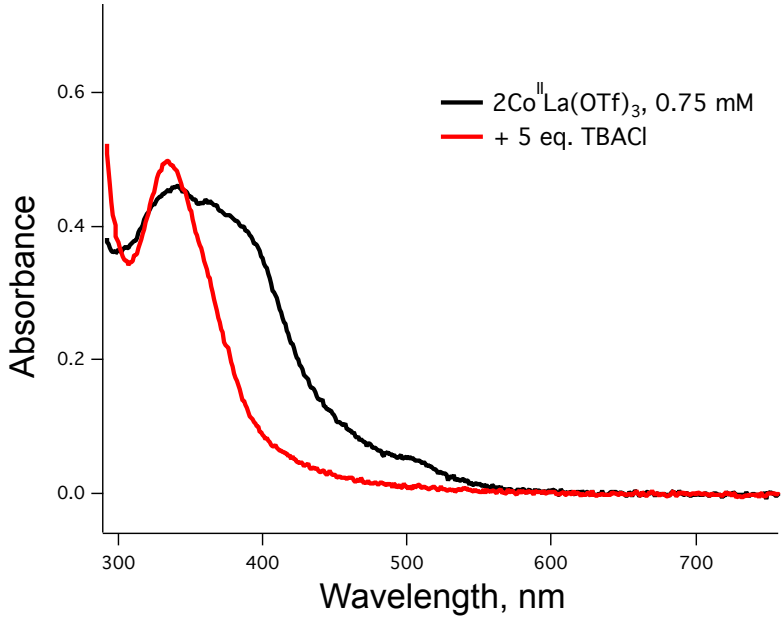


**Figure 1.36:** UV-Vis spectra from the titration of **$2Co^{II}La(OTf)_3$** with tetrabutylammonium chloride in propylene carbonate. Spectra were taken at 0.75 mM in a 1 mm cuvette.

## 1.6 References


1. Warshel, A., *Journal of Biological Chemistry* **1998,** *273* (42), 27035-27038.

2. Warshel, A.; Sharma, P. K.; Kato, M.; Xiang, Y.; Liu, H.; Olsson, M. H. M., *Chem. Rev.* **2006,** *106* (8), 3210-3235.

3. Isaksen, G. V.; Hopmann, K. H.; Åqvist, J.; Brandsdal, B. O., *Biochem.* **2016,** *55* (14), 2153-2162.

4. Perrin, D. D., Tables. In *Ionisation Constants of Inorganic Acids and Bases in Aqueous Solution (Second Edition)*, Pergamon: 1982; pp 1-138.

5. Gutmann, V., *Electrochimica Acta* **1976,** *21* (9), 661-670.

6. Morgenstern, A.; Jaszai, M.; Eberhart, M. E.; Alexandrova, A. N., *Chem. Sci.* **2017,** *8* (7), 5010-5018.

7. Shannon, R., *Acta Crystallogr., Sect. A: Found. Crystallogr.* **1976,** *32* (5), 751-767.

8. Kolling, O. W., *Analytical Chemistry* **1982,** *54* (2), 260-264.

9. Munakata, M.; Kitagawa, S.; Miyazima, M., *Inorg. Chem.* **1985,** *24* (11), 1638-1643.

10. Yocum, C. F., *Coord. Chem. Rev.* **2008,** *252* (3–4), 296-305.

11. Ferreira, K. N.; Iverson, T. M.; Maghlaoui, K.; Barber, J.; Iwata, S., *Science* **2004,** *303* (5665), 1831-1838.

12. Yano, J.; Kern, J.; Sauer, K.; Latimer, M. J.; Pushkar, Y.; Biesiadka, J.; Loll, B.; Saenger, W.; Messinger, J.; Zouni, A.; Yachandra, V. K., *Science* **2006,** *314* (5800), 821-825.

13. Barber, J., *Inorg. Chem.* **2008,** *47* (6), 1700-1710.

14. Sauer, K.; Yano, J.; Yachandra, V. K., *Coord. Chem. Rev.* **2008,** *252* (3–4), 318-335.

15. Umena, Y.; Kawakami, K.; Shen, J.-R.; Kamiya, N., *Nature* **2011,** *473* (7345), 55-60.

16. Pecoraro, V. L.; Baldwin, M. J.; Caudle, M. T.; Hsieh, W. Y.; Law, N. A., A proposal for water oxidation in photosystem II. In *Pure Appl. Chem.*, **1998**; Vol. 70, p 925.

17. Cady, C. W.; Crabtree, R. H.; Brudvig, G. W., *Coord. Chem. Rev.* **2008,** *252* (3–4), 444-455.

18. Brudvig, G. W., *Philos. Trans. R. Soc., B* **2008,** *363* (1494), 1211-1219.

19. Mullins, C. S.; Pecoraro, V. L., *Coord. Chem. Rev.* **2008,** *252* (3–4), 416-443.

20. Díaz-Torres, R.; Alvarez, S., *Dalton Trans.* **2011,** *40* (40), 10742-10750.

21. Yiu, S.-M.; Man, W.-L.; Lau, T.-C., *J. Am. Chem. Soc.* **2008,** *130* (32), 10821-10827.

22. Miller, C. G.; Gordon-Wylie, S. W.; Horwitz, C. P.; Strazisar, S. A.; Peraino, D. K.; Clark, G. R.; Weintraub, S. T.; Collins, T. J., *J. Am. Chem. Soc.* **1998,** *120* (44), 11540-11541.

23. Guo, H.; Chen, Z.; Mei, F.; Zhu, D.; Xiong, H.; Yin, G., *Chem. Asian J.* **2013,** *8* (5), 888-891.

24. Dong, L.; Wang, Y.; Lv, Y.; Chen, Z.; Mei, F.; Xiong, H.; Yin, G., *Inorg. Chem.* **2013,** *52* (9), 5418-5427.

25. Zhang, Z.; Coats, K. L.; Chen, Z.; Hubin, T. J.; Yin, G., *Inorg. Chem.* **2014,** *53* (22), 11937-11947.

26. Chen, Z.; Yang, L.; Choe, C.; Lv, Z.; Yin, G., *Chem. Commun.* **2015,** *51* (10), 1874-1877.

27. Qin, S.; Dong, L.; Chen, Z.; Zhang, S.; Yin, G., *Dalton Trans.* **2015,** *44* (40), 17508-17515.

28. Zhang, S.; Chen, Z.; Qin, S.; Lou, C.; Senan, A. M.; Liao, R.-Z.; Yin, G., *Org. Biomol. Chem.* **2016,** *14* (17), 4146-4157.

29. Choe, C.; Yang, L.; Lv, Z.; Mo, W.; Chen, Z.; Li, G.; Yin, G., *Dalton Trans.* **2015,** *44* (19), 9182-9192.

30. Park, J.; Morimoto, Y.; Lee, Y.-M.; Nam, W.; Fukuzumi, S., *J. Am. Chem. Soc.* **2011,** *133* (14), 5236-5239.

31. Kumbharkhane, A. C.; Puranik, S. M.; Mehrotra, S. C., *Journal of Solution Chemistry* **1993,** *22* (3), 219-229.

32. Metz, D. J.; Glines, A., *J. Phys. Chem.* **1967,** *71* (4), 1158-1158.

33. Carvajal, C.; Tölle, K. J.; Smid, J.; Szwarc, M., *J. Am. Chem. Soc.* **1965,** *87* (24), 5548-5553.

34. Payne, R.; Theodorou, I. E., *J. Phys. Chem.* **1972,** *76* (20), 2892-2900.

35. Cammarota, R. C.; Lu, C. C., *J. Am. Chem. Soc.* **2015,** *137* (39), 12486-12489.

36. Park, Y. J.; Ziller, J. W.; Borovik, A. S., *J. Am. Chem. Soc.* **2011,** *133* (24), 9258-9261.

37. Morimoto, Y.; Kotani, H.; Park, J.; Lee, Y.-M.; Nam, W.; Fukuzumi, S., *J. Am. Chem. Soc.* **2011,** *133* (3), 403-405.

38. Fukuzumi, S.; Morimoto, Y.; Kotani, H.; Naumov, P.; Lee, Y.-M.; Nam, W., *Nat. Chem.* **2010,** *2* (9), 756-759.

39. Karlin, K. D., *Nat. Chem.* **2010,** *2* (9), 711-712.

40. Hong, S.; Lee, Y.-M.; Sankaralingam, M.; Vardhaman, A. K.; Park, Y. J.; Cho, K.-B.; Ogura, T.; Sarangi, R.; Fukuzumi, S.; Nam, W., *J. Am. Chem. Soc.* **2016,** *138* (27), 8523-8532.

41. Tsui, E. Y.; Agapie, T., *Proc. Natl. Acad. Sci.* **2013,** *110* (25), 10084-10088.

42. Tsui, E. Y.; Tran, R.; Yano, J.; Agapie, T., *Nat. Chem.* **2013,** *5* (4), 293-299.

43. Krewald, V.; Neese, F.; Pantazis, D. A., *Phys. Chem. Chem. Phys.* **2016,** *18* (16), 10739-10750.

44. Lin, P.-H.; Takase, M. K.; Agapie, T., *Inorg. Chem.* **2015,** *54* (1), 59-64.

45. Herbert, D. E.; Lionetti, D.; Rittle, J.; Agapie, T., *J. Am. Chem. Soc.* **2013,** *135* (51), 19075-19078.

46. Al Obaidi, N.; Beer, P. D.; Bright, J. P.; Jones, C. J.; McCleverty, J. A.; Salam, S. S., *J. Chem. Soc., Chem. Commun.* **1986,** (3), 239-241.

47. Plenio, H.; Diodone, R., *Inorg. Chem.* **1995,** *34* (15), 3964-3972.

48. Beer, P. D.; Blackburn, C.; McAleer, J. F.; Sikanyika, H., *Inorg. Chem.* **1990,** *29* (3), 378-381.

49. Andrews, M. P.; Blackburn, C.; McAleer, J. F.; Patel, V. D., *J. Chem. Soc., Chem. Commun.* **1987,** (14), 1122-1124.

50. Delgado, M.; Ziegler, J. M.; Seda, T.; Zakharov, L. N.; Gilbertson, J. D., *Inorg. Chem.* **2016,** *55* (2), 555-557.

51. Risch, M.; Klingan, K.; Ringleb, F.; Chernev, P.; Zaharieva, I.; Fischer, A.; Dau, H., *ChemSusChem* **2012,** *5* (3), 542-549.

52. Hadt, R. G.; Hayes, D.; Brodsky, C. N.; Ullman, A. M.; Casa, D. M.; Upton, M. H.; Nocera, D. G.; Chen, L. X., *J. Am. Chem. Soc.* **2016,** *138* (34), 11017-11030.

53. Hodel, F. H.; Luber, S., *ACS Catalysis* **2016**, 6750-6761.

54. Evangelisti, F.; Moré, R.; Hodel, F.; Luber, S.; Patzke, G. R., *J. Am. Chem. Soc.* **2015,** *137* (34), 11076-11084.

55. Van Staveren, C. J.; Van Eerden, J.; Van Veggel, F. C. J. M.; Harkema, S.; Reinhoudt, D. N., *J. Am. Chem. Soc.* **1988,** *110* (15), 4994-5008.

56. Kumar, A.; Lionetti, D.; Day, V. W.; Blakemore, J. D., *Chem. Eur. J.* **2018,** *24* (1), 141-149.

57. Akine, S.; Utsuno, F.; Piao, S.; Orita, H.; Tsuzuki, S.; Nabeshima, T., *Inorg. Chem.* **2016,** *55* (2), 810-821.

58. Liu, D.-F.; Lü, X.-Q.; Lu, R., *Transition Met. Chem.* **2014,** *39* (6), 705-712.

59. West, B. O., *Journal of the Chemical Society (Resumed)* **1954,** (0), 395-400.

60. Alleman, K. S.; Peters, D. G., *J. Electroanal. Chem.* **1998,** *451* (1–2), 121-128.

61. Harned, H. S.; Geary, C. G., *J. Am. Chem. Soc.* **1937,** *59* (10), 2032-2035.

62. Kangro, W., Konzentrierte wäßrige Lösungen, II. In *Zeitschrift für Physikalische Chemie*, **1962**; Vol. 32, p 273.

63. Corain, B.; Longato, B.; Favero, G.; Ajò, D.; Pilloni, G.; Russo, U.; Kreissl, F. R., *Inorg. Chim. Acta* **1989,** *157* (2), 259-266.

64. Van Veggel, F. C. J. M.; Harkema, S.; Bos, M.; Verboom, W.; Van Staveren, C. J.; Gerritsma, G. J.; Reinhoudt, D. N., *Inorg. Chem.* **1989,** *28* (6), 1133-1148.

65. Van Veggel, F. C. J. M.; Harkema, S.; Bos, M.; Verboom, W.; Woolthuis, G. K.; Reinhoudt, D. N., *J. Org. Chem.* **1989,** *54* (10), 2351-2359.

66. Horwitz, C. P.; Ciringh, Y., *Inorg. Chim. Acta* **1994,** *225* (1–2), 191-200.

67. Serr, B. R.; Andersen, K. A.; Elliott, C. M.; Anderson, O. P., *Inorg. Chem.* **1988,** *27* (24), 4499-4504.

68. Lin, Z.-J.; Yang, Z.; Liu, T.-F.; Huang, Y.-B.; Cao, R., *Inorg. Chem.* **2012,** *51* (3), 1813-1820.

69. Wang, X.; Zhao, J.; Zhao, Y.; Xu, H.; Shen, X.; Zhu, D.-R.; Jing, S., *Dalton Trans.* **2015,** *44* (19), 9281-9288.

70. Russell, S. E.; Gosset, C.; Agache, X.; Volkringer, C.; Henry, N.; Decadt, R.; Van Deun, R.; Visseaux, M.; Loiseau, T., *CrystEngComm* **2016,** *18* (20), 3594-3605.

71. Morgan, W. E.; Van Wazer, J. R.; Stec, W. J., *J. Am. Chem. Soc.* **1973,** *95* (3), 751-755.

72. Pui, A.; Policar, C.; Mahy, J.-P., *Inorg. Chim. Acta* **2007,** *360* (6), 2139-2144.

73. Ortiz, B.; Park, S.-M., *Bull. Korean Chem. Soc.* **2000,** *21* (4), 405-411.

74. Fried, S. D.; Boxer, S. G., *Acc. Chem. Res.* **2015,** *48* (4), 998-1006.

75. APEX2 Version 2014.11-0, B. A., Inc.; Madison, WI 2014.

76. SAINT Version 8.34a, B. A., Inc.; Madison, WI 2013.

77. Sheldrick, G. M. S., Version 2014/5, Bruker AXS, Inc.; Madison, WI 2014.

78. Sheldrick, G. M. SADABS, Version 2014/5, Bruker AXS, Inc.; Madison, WI 2014. .

79. International Tables for Crystallography 1992, Vol. C., Dordrecht: Kluwer Academic Publishers.

# CHAPTER 2:

# EXPERIMENTAL AND THEORETICAL INVESTIGATIONS OF ELECTROSTATIC INTERACTIONS IN NICKEL SCHIFF BASE COMPLEXES

The majority of the synthesis and characterization of the complexes presented in this chapter was carried out by undergraduate researcher Kevin Kang under my supervision. DFT studies were conducted by doctoral student Jack Fuller III and Prof. Anastassia Alexandrova at the University of California, Los Angeles.

## 2.1 Motivation and Specific Aims

In Chapter 1, the use of the **1M** metalloligand was used to demonstrate electrostatic interactions and their resulting effects on heterobimetallic cobalt complexes. In order to better understand how electrostatics modulate the properties of transition metal complexes, this heterobimetallic series was expanded to include other transition metals. The following chapter outlines the synthesis, characterization, and detailed analysis of the electronic structure of a series of nickel complexes utilizing the **1M** framework. Nickel was chosen for further study due to its close proximity to cobalt on the periodic table, ability to form stable salen complexes, and air-stability. Another advantage is the diamagnetic electron configuration of $Ni^{II}$(salen) complexes, which greatly simplifies the application of density functional theory to model electronic orbitals. Computational studies, in addition to the experimental work presented herein, provides a more comprehensive and quantitative analysis of the molecular orbital manifold in the presence of electrostatic fields.

## 2.2 Background

Efforts to generate modular electric fields have focused on installation of non-redox active cations proximal to redox-active reaction sites. Chapter 1 discusses the cobalt derivatives of the salen-crown ligand framework shown in Scheme 2.1. The crown moiety appended to the four-coordinate Schiff-base ligand can accommodate a large range of cationic metal centers ($M_2$). Alkali and alkaline earth metals were utilized because they are known to generate significant electric fields in enzymes[1-2] and zeolite cavities.[3] A subsequent study on the analogous iron complexes

found the magnitude of the $Fe^{III/II}$ reduction potential also had a strong dependence on both $M_2$ and whether a counterion was coordinated to the Fe.[4] However, initial studies lacked definitive evidence for the magnitude of the electric field, its impact on the electronic structure of the redox-active center, and the effect of inner-sphere anions. These details are critical to effectively utilize cations to generate directional electric fields to optimize reaction rates or selectivity.

**Scheme 2.1:**

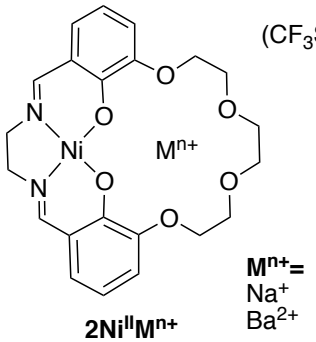


In order to investigate the electrostatic effects in more detail and to enable the use of density functional theory for modelling molecular orbital energies, a diamagnetic $Ni^{II}$ analogue of the ligand with $Na^+$ and $Ba^{2+}$ cations as $M_2$ (Scheme 2.1) was synthesized and characterized. As electric fields scale with charge, dications would be expected to have twice the effect on its magnitude as monocations. The salen framework easily accommodates a square-planar closed-shell $Ni^{II}$ coordination environment. This chapter outlines the synthesis and spectroscopic properties of $Ni^{II}$ complexes with $Na^+$ or $Ba^{2+}$ incorporated in the crown as well as computational methods to more fully understand the changes in redox potential and electronic properties. Taken together, this study provides a detailed and quantitative examination of how positioned cations install electric field of fixed magnitude and direction.

## 2.3 Results and Discussion

### 2.3.1 Synthesis and Characterization

**1Na(OTf)** and **1Ba(OTf)$_2$** were synthesized using a modified literature procedure outlined in Chapter 1.[5] **1Na(OTf)** and **1Ba(OTf)$_2$** were synthesized using the corresponding metal triflate salts. **1M** (M = $Na^+$, $Ba^{2+}$) ligand and an equivalent of $Ni(OAc)_2$ were refluxed in methanol to synthesize the heterobimetallic **2M** $Ni^{II}$ complexes (Scheme 2.1). Synthesis was followed by removal of methanol and acetic acid *in vacuo*. The heterobimetallic complexes were purified and recrystallized by vapor diffusion of diethyl ether into methanol solutions of each compound. The compound identities were confirmed using mass spectrometry and single crystal X-ray diffraction analysis. Purities were determined by elemental analysis. Ni(salen-OMe) (salen-OMe = N,N'-bis(3-methoxysalicylidene)-1,2-diaminoethane) was synthesized according to a literature procedure[6] to compare with the **2M** complexes.

Compounds were characterized by $^1$H NMR spectroscopy, shown in Figures 2.10-12. Compared to Ni(salen-OMe), each **2M** complex had a downfield shift in the imine proton signal with a greater shift correlating with higher cationic charge. The imine proton in **1M** complexes was shifted farther downfield than in the corresponding **2M** complexes.

### 2.3.2 Structural Studies

Single crystals for X-ray diffraction were grown by diffusion of diethyl ether into methanol solutions of the **2M** triflate salts; the solid-state structures are shown in Figure 2.1. In each heterobimetallic complex, the triflate counteranions are bound to the M cation. In **2Ni$^{II}$Ba(OTf)$_2$**, two triflate anions are coordinated to the $Ba^{2+}$ and form a symmetric bridge to an adjacent

**2Ni$^{II}$Ba(OTf)$_2$** complex. The mass spectrum does not contain peaks consistent with a dimer, suggesting that the species only exists in the solid-state form. A methanol molecule is also coordinated to each $Ba^{2+}$ cation.

Each complex contains a minimally distorted square planar nickel ion with the M cation inhabiting the crown ether pocket. The $\tau_4$ values describing the coordination around the $Ni^{II}$ ions are listed in Table 2.1 and confirm similar coordination environments.[7] The distances between the $Ni^{II}$ ion and M cations are also listed in Table 2.1.

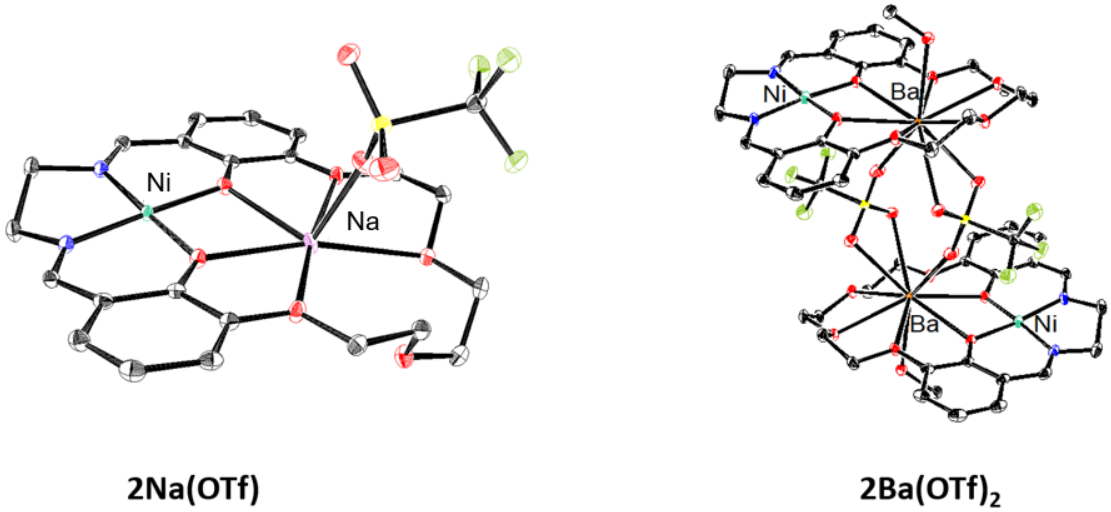


**2Na(OTf)** **2Ba(OTf)$_2$**

**Figure 2.1:** Solid-state structures of **2Ni$^{II}$Na(OTf)** and **2Ni$^{II}$Ba(OTf)$_2$**. Thermal ellipsoids are drawn to 50% probability. Hydrogen atoms, outer-sphere anions, and solvent molecules have been omitted for clarity.

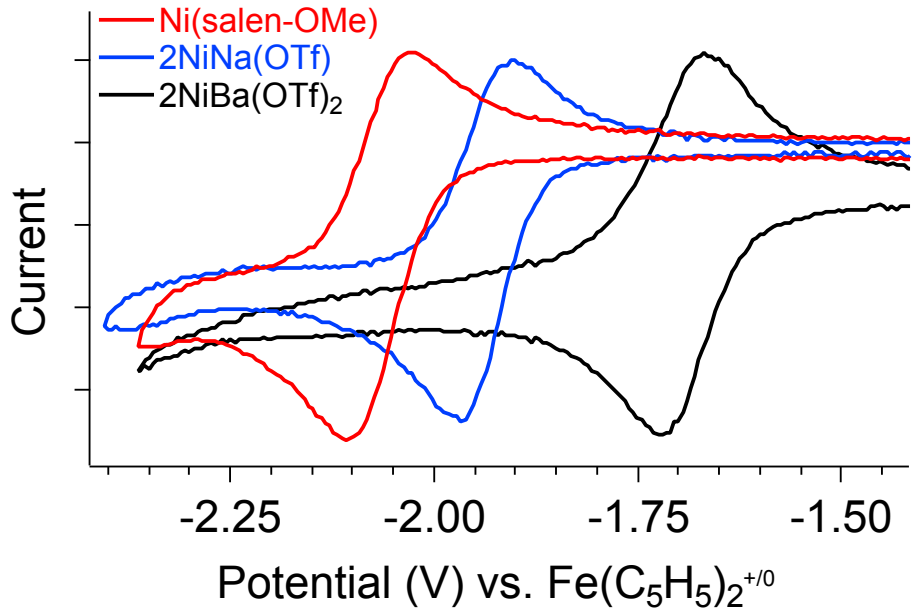


**Figure 2.2:** Cyclic voltammograms of the reversible Ni $^{II/I}$ redox couples of Ni(salen-OMe) and **2NiM** (M = $Na^+$, $Ba^{2+}$) in 0.1 M tetrabutylammonium hexafluorophosphate in acetonitrile under $N_2$ at a scan rate of 100 mV/s. Individual CVs are shown in Figures 2.13-15.

### 2.3.3 Electrochemistry

Cyclic voltammetry of Ni(salen-OMe) in acetonitrile versus ferrocene/ferrocenium revealed a reversible reduction at -2.07 V that is assigned to a $Ni^{II/I}$ redox event (Figure 2.2, red trace). The corresponding $Ni^{II/I}$ reduction events in **2Ni$^{II}$Na(OTf)** and **2Ni$^{II}$Ba(OTf)$_2$** are also reversible and found at -1.94 and -1.69 V, respectively**.** Compared to Ni(salen-OMe), the redox potential for **2Ni$^{II}$Na(OTf)$_2$** and **2Ni$^{II}$Ba(OTf)$_2$** are shifted positive by 130 mV and 380 mV, respectively. The increased difference in redox potential correlates with increased cationic charge, similar to the observed trend in the **2Co$^{II}$M** complexes in Chapter 1.[8]

### 2.3.4 Electronic and Vibrational Spectroscopy

The compounds were examined by electronic absorption and infrared spectroscopy to further probe the electronic effects of the $Na^+$ and $Ba^{2+}$ cation on the $Ni^{II}$ ligand field. The

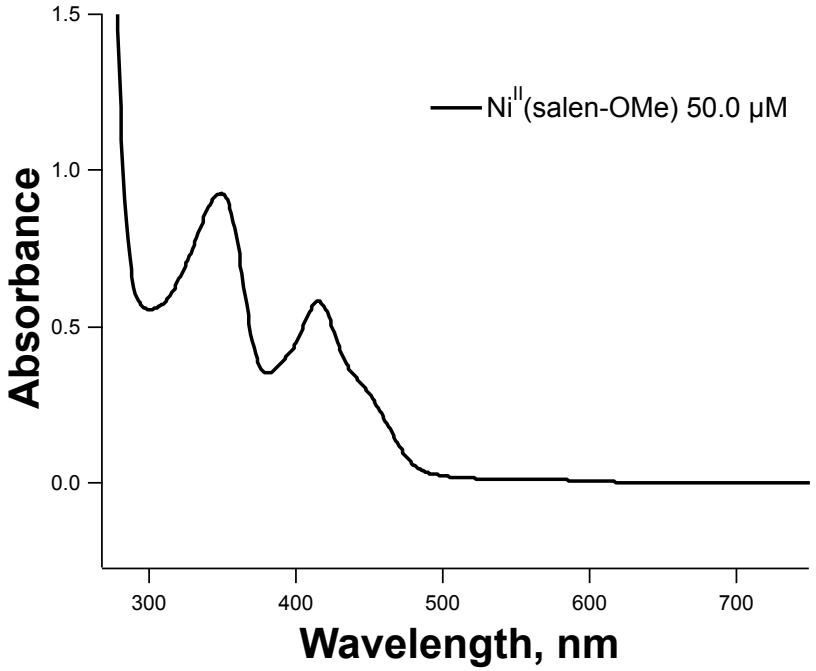


**Figure 2.3:** UV-Vis spectrum of Ni(salen-OMe), 50.0 µM in dimethylformamide.

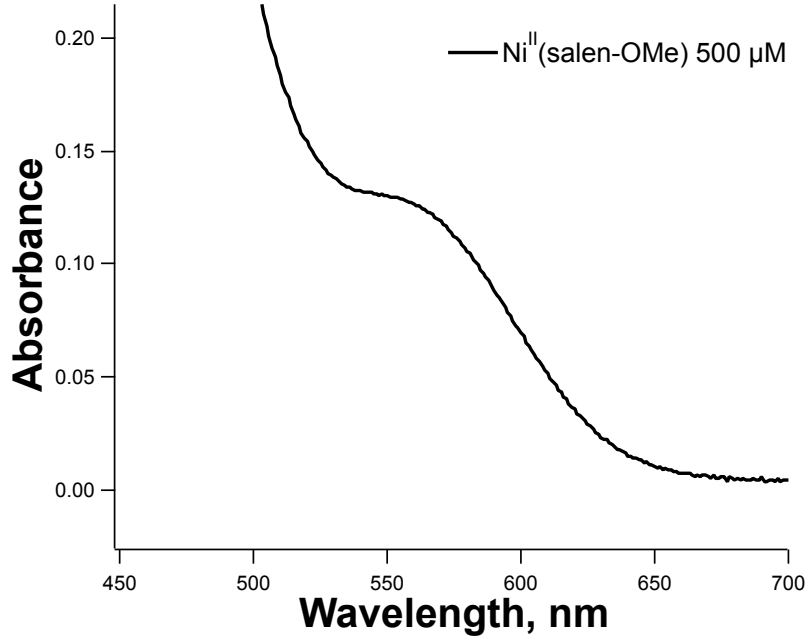


**Figure 2.4:** UV-Vis spectrum of Ni(salen-OMe), highlighting the d→d absorption band, 500 µM in dimethylformamide.

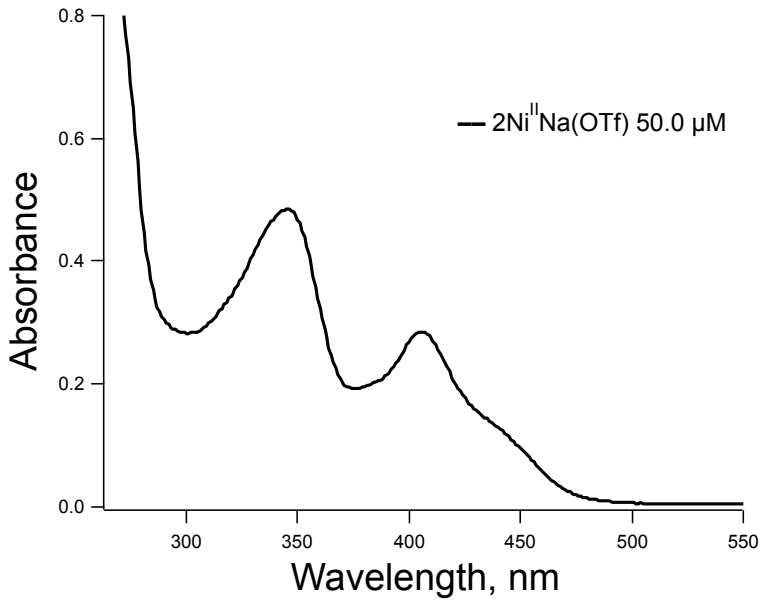


**Figure 2.5:** UV-Vis spectrum of **2Ni$^{II}$Na(OTf)**, 50.0 µM in dimethylformamide.

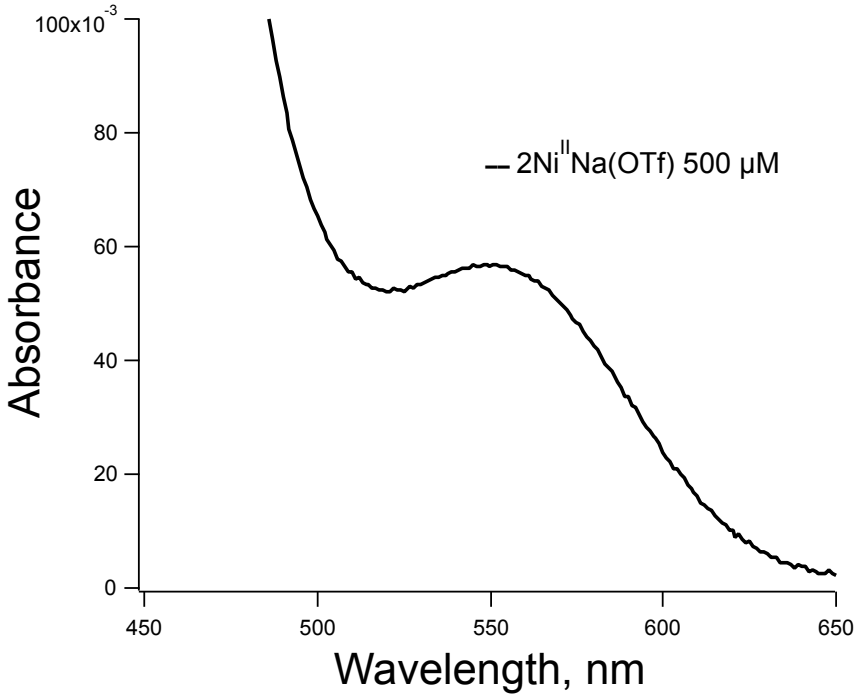


**Figure 2.6:** UV-Vis spectrum of **2Ni$^{II}$Na(OTf)**, highlighting the d→d absorption band, 500 µM in dimethylformamide.

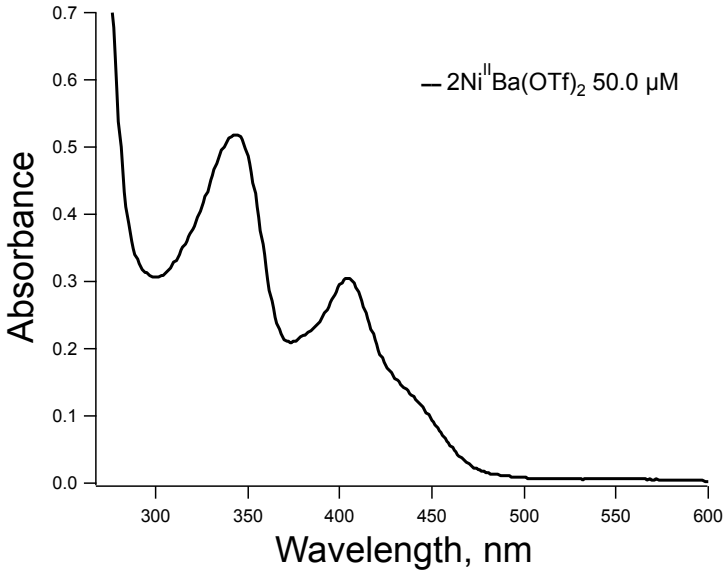


**Figure 2.7:** UV-Vis spectrum of **$2Ni^{II}Ba(OTf)_2$**, 50.0 µM in dimethylformamide.

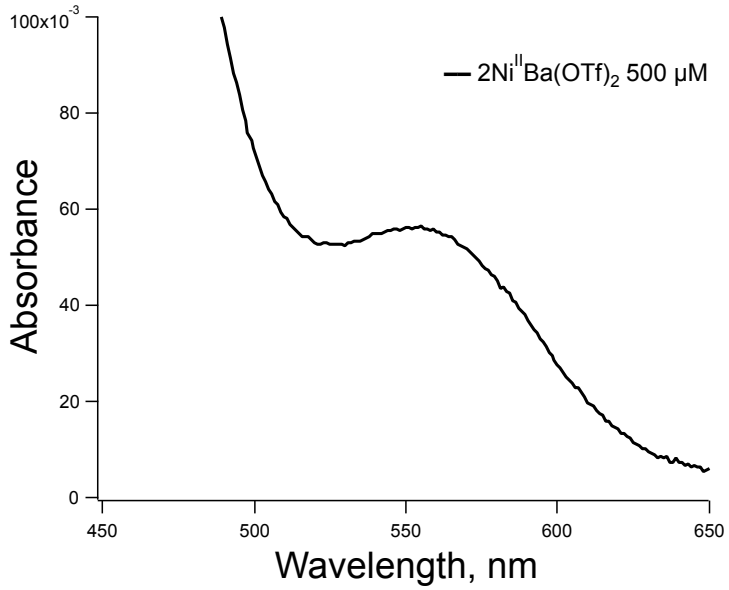


**Figure 2.8:** UV-Vis spectrum of **$2Ni^{II}Ba(OTf)_2$**, highlighting the d→d absorption band, 500 µM in dimethylformamide.

**Table 2.1:** Summary of structural, spectroscopic, and electrochemical data for Ni(salen-OMe) and **2Ni$^{II}$M** complexes.

| Complex | $E_{1/2}$ $Ni^{II/I}$,[a] V | ΔE,[b] V | Ni···M , Å | $Ni^{II}$ ion, $\tau_4$[c] | ν(C=N), $cm^{-1}$ |
|---|---|---|---|---|---|
| **Ni(salen–OMe)** | -2.07 | -- | -- | 0.0152[d] | 1545 |
| **2Ni$^{II}$Na(OTf)** | -1.94 | 0.12 | 3.4374(6) | 0.0217 | 1553 |
| **2Ni$^{II}$Ba(OTf)$_2$** | -1.69 | 0.38 | 3.7095(4) | 0.0882 | 1554 |

[a]Reduction potentials in acetonitrile referenced to ferrocene/ferrocenium. [b]Difference between the reduction potential of 2M and Ni(salen–OMe). [c]$\tau_4$ value describing the coordination geometry around the $Ni^{II}$ ions, where $\tau_4$ =1 for a tetrahedral geometry and $\tau_4$ = 0 for a square planar geometry. [d]From ref 14.

electronic absorption spectra in dimethylformamide are shown in figures 2.3-2.8 and are summarized in Table 2.2. The absorption spectrum of Ni(salen-OMe) displays a π → π* transition at 349 nm and a d → π* (MLCT) transition at 415 nm.[9-10] The **2M** complexes exhibit a slight blue shift in both their π → π* bands (≤5 nm) and MLCT bands (≤11 nm) relative to Ni(salen-OMe). Additionally, Ni(salen-OMe) has a d → d absorption band at 547 nm, which appears in **2M** with a small red shift (≤8 nm). Molar absorptivity for each transition for **2M** is comparable to Ni(salen-OMe). Changes in absorption in **2NiM** compared to Ni(salen-OMe) indicate that the presence of M influences the ligand field around the $Ni^{II}$ center; however, it appears to only have a minor effect relative to changes in redox potential.

Solid state infrared spectroscopy of the complexes was taken to compare the electronic environment of the nickel center (Figures 2.16-2.19). As cationic charge increases, the vibrational frequency of the imine C=N stretch increases (Table 2.1).

### 2.3.5 Computational Studies

To clarify the effect of the secondary cation, density functional theory (DFT) calculations were performed using the ωB97X-D functional.[11] The def2-SVP basis set was used for geometry optimizations and the def2-TZVP basis for final electronic energies and spectra.[12] Solvent was modeled using the SMD solvent model[13] with the corresponding parameters for dimethylformamide or acetonitrile. Calculations were performed using Gaussian 09[14] and electrostatic potential maps were plotted using ChemCraft.[15]

Electronic absorption spectra simulated using time-dependent DFT (TD-DFT)[16] showed fairly good agreement with experimental spectra; only small shifts in wavelengths were observed for different secondary cations (Table 2.2). However, all the frontier orbitals shift in energy by a similar magnitude with increasing cationic charge, as shown in Figure 2.9. The small relative changes in orbital energies is consistent with the modest differences observed in absorption spectra. In addition, the energies of all the MOs near the HOMO-LUMO gap trend in response to the field in a nearly parallel fashion. Hence, minimal spectral changes can be seen. Both the experimental and computational results indicate the major impact of the secondary cations is electrostatic as they do not significantly alter the ligand field at the redox site. Instead, the reduction potential from Ni(salen-OMe) to **2Ni$^{II}$Na(OTf)** (0.27 eV) and to **2Ni$^{II}$Ba(OTf)$_2$** (0.42 eV) shifts positive as the LUMO energy trends down in energy as a function of the electric field generated by the cation.

**Table 2.2:** Observed and calculated UV-Vis transitions for **2Ni$^{II}$M** and Ni$^{II}$(salen-OMe).

| Complex | λ(d→d), nm (ε, $M^{-1}cm^{-1}$) | Calc. λ(d→d), nm | λ(π→π*)[a], nm (ε, $M^{-1}cm^{-1}$) | Calc. λ (π→π*), nm | λ (MLCT)[a], nm (ε, $M^{1}cm^{-1}$) | Calc. λ (MLCT), nm |
|---|---|---|---|---|---|---|
| **Ni(salen–OMe)** | 547 (111) | 563 | 349 (8033) | 345 | 415 (5019) | 390 |
| **2Ni$^{II}$Na(OTf)** | 552 (113) | 565 | 345 (9800) | 333 | 406 (5695) | 389 |
| **2Ni$^{II}$Ba(OTf)$_2$** | 555 (105) | 607 | 344 (9358) | 327 | 404 (5176) | 386 |

[a]Assignment based on ref. 16 and 17

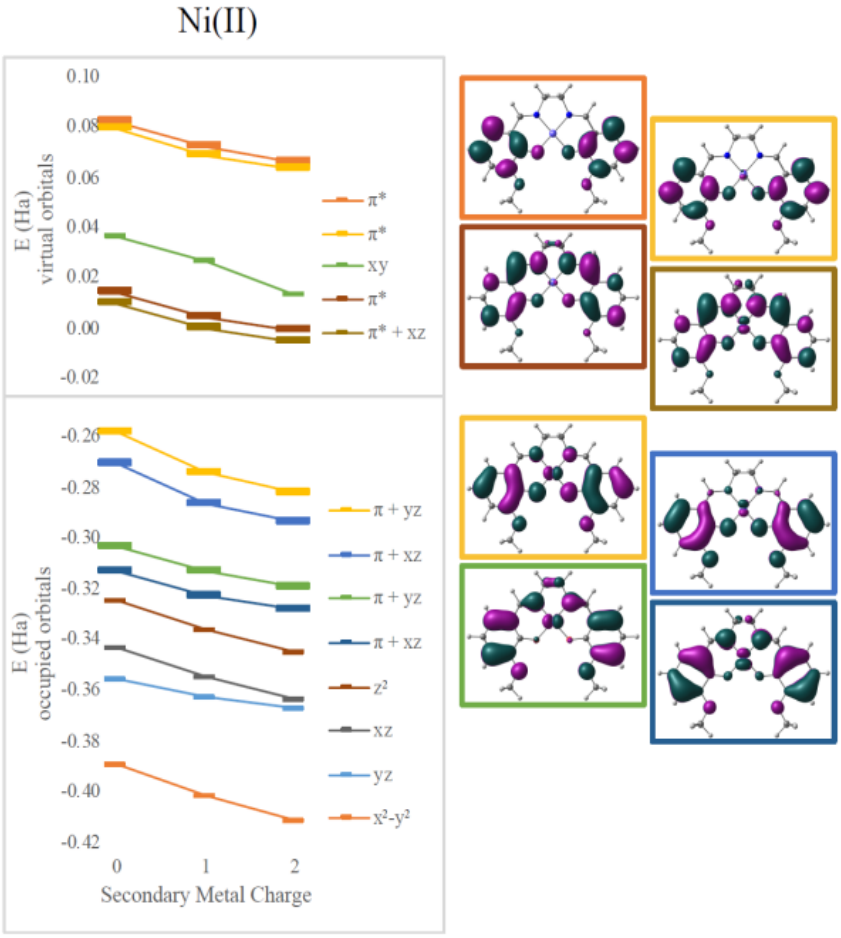


**Figure 2.9:** Effect of secondary metals on orbital energies in Ni complexes. Orbitals involved in MLCT are bolded in the graph and plotted on the right for the Ni(salen–OMe) complex.

## 2.4 Conclusions

The development of the **2Ni$^{II}$M** series of heterobimetallic complexes expanded the range of heterobimetallic complexes from the work discussed in Chapter 1. These studies show that the electrostatic potential effects from the proximal cation interact with both transition metal hosts in a similar manner, regardless of open or closed shell electron configurations. The anodic potential shift of the $Ni^{II/I}$ couple of up to 380 mV was observed, which is slightly larger than those observed in the **2Co$^{II}$M** series. UV-vis spectroscopy shows that the lowest energy d-d transition is not strongly affected by the electrostatic interactions. The electronic environment of the metal center, measured by the C=N stretch of the imine donors, is consistent with the decreased ability of the metal to participate in π-backbonding in the presence of a cationic field. TD-DFT calculations modelling the energies of the frontier molecular orbitals demonstrate the electrostatic basis for the potential shift, and also reveal the expanded electronic MO scaffold that could not be observed through UV-vis spectroscopy or electrochemical analysis.

## 2.5 Experimental Details

**General Considerations:** For syntheses containing air and moisture sensitive reagents or products, manipulations were carried out in a glovebox or using standard Schlenk techniques under an inert atmosphere of nitrogen. Unless otherwise noted, all experiments were carried out at room temperature (21-24 °C). All solvents used were degassed by sparging with argon and dried by passing through columns of neutral alumina or molecular sieves. Deuterated acetonitrile was purchased from Cambridge Isotopes Laboratories, Inc. and was degassed and stored over activated 3 Å molecular sieves prior to use. Reagents were purchased from

commercial vendors and used without further purification unless otherwise noted. 3,3'-(((ethane-1,2-diylbis(oxy))bis(ethane-2,1-diyl))bis(oxy))bis(2-hydroxybenzaldehyde) was synthesized according to a literature preparation[6] with the following modification. The crude product was purified by silica gel column chromatography using a ratio of ethyl acetate to hexanes of 1:1 that progressed to a ratio of 2:1.

**Physical Methods:** NMR spectra were taken on a 500 MHz Bruker Avance GN500 ($^1$H) with a BBO probe at 20 °C. Electrospray ionization mass spectrometry was performed using an ESI LC-TOF Micromass LCT 3 mass spectrometer. Elemental analysis was taken on a PerkinElmer 2400 Series II CHNS elemental analyzer. Infrared (IR) absorption measurements were taken as compressed solids on a Thermo Scientific Nicolet iS5 spectrophotometer with an iD5 ATR attachment. UV-vis spectra were collected in dimethylformamide solution using an Agilent Technologies Cary 60 UV−vis.

**Electrochemical procedures**

All measurements performed on a Pine Wavedriver 10bipotentiostat with a 2 mm diameter glassy carbon disc working electrode, a glassy carbon counter electrode, and a Ag/Ag+ psuedoreference electrode separated from the bulk solution by a Vicor frit. Potentials were referenced to a ferrocene internal standard at 0 V, and all experiments were performed in dry, degassed acetonitrile at a concentration of 1 mM analyte and 0.1 M tetrabutylammonium hexafluorophosphate and at a 100 mV/s scan rate unless otherwise noted.

**X-ray Crystallographic Methods**

X-ray Data Collection, Structure Solution and Refinement for **2Ni$^{II}$Na(OTf)**.

A violet crystal of approximate dimensions 0.759 x 0.342 x 0.208 mm was mounted on a glass fiber and transferred to a Bruker SMART APEX II diffractometer. The APEX2[17] program package was used to determine the unit-cell parameters and for data collection (15 sec/frame scan time for a sphere of diffraction data). The raw frame data was processed using SAINT[18] and SADABS[19] to yield the reflection data file. Subsequent calculations were carried out using the SHELXTL[20] program. The diffraction symmetry was 2/*m* and the systematic absences were consistent with the monoclinic space group $P2_1/n$ that was later determined to be correct.

The structure was solved by direct methods and refined on $F^2$ by full-matrix least-squares techniques. The analytical scattering factors[21] for neutral atoms were used throughout the analysis. Hydrogen atoms were located from a difference-Fourier map and refined (x,y,z and $U_{iso}$).

Least-squares analysis yielded wR2 = 0.0599 and Goof = 1.046 for 361 variables refined against 6354 data (0.73 Å), R1 = 0.0233 for those 5947 data with $I > 2.0\sigma(I)$.

X-ray Data Collection, Structure Solution and Refinement for **$2Ni^{II}Ba(OTf)_2$**

A red crystal of approximate dimensions 0.204 x 0.366 x 0.367 mm was mounted in a cryoloop and transferred to a Bruker SMART APEX II diffractometer. The APEX2[17] program package was used to determine the unit-cell parameters and for data collection (15 sec/frame scan time for a sphere of diffraction data). The raw frame data was processed using SAINT[18] and SADABS[19] to yield the reflection data file. Subsequent calculations were carried out using the SHELXTL[20] program. There were no systematic absences nor any diffraction symmetry other than the Friedel condition. The centrosymmetric triclinic space group $P\bar{1}$ was assigned and later determined to be correct.

The structure was solved by direct methods and refined on $F^2$ by full-matrix least-squares techniques. The analytical scattering factors[21] for neutral atoms were used throughout the analysis. Hydrogen atom H(13) was located from a difference-Fourier map and refined (x,y,z and $U_{iso}$). The remaining hydrogen atoms were included using a riding model. The molecule was a dimer located about an inversion center. There were two non-coordinated triflate ions present per dimeric formula-unit.

Least-squares analysis yielded wR2 = 0.0594 and Goof = 1.054 for 456 variables refined against 7985 data (0.73 Å), R1 = 0.0219 for those 7701 data with $I > 2.0\sigma(I)$.

Definitions:
wR2 = $[\Sigma[w(F_o^2-F_c^2)^2] / \Sigma[w(F_o^2)^2] ]^{1/2}$
R1 = $\Sigma||F_o|-|F_c|| / \Sigma|F_o|$
Goof = S = $[\Sigma[w(F_o^2-F_c^2)^2] / (n-p)]^{1/2}$ where n is the number of reflections and p is the total number of parameters refined.
The thermal ellipsoid plot is shown at the 50% probability level.

**Synthetic Procedures**

**Method 2.1: General procedure for synthesis of 2M:** In an inert atmosphere glovebox, 1 equivalent of **1M** ($M = Na^+$, $Ba^{2+}$) was dissolved in refluxing methanol. 1 equivalent of $Ni(OAc)_2$ was added dropwise in a concentrated methanol solution over several minutes, and the reaction was refluxed for ten minutes. The crude red product was isolated under reduced pressure at 80 °C, redissolved in methanol, and passed through a glass microfiber filter. Vapor diffusion of diethyl ether into the methanol solution precipitated the product as crystals, which were isolated by filtration and washed with diethyl ether.

**Ni(salen-OMe):** Synthesized according to a previous literature procedure[6] with salen-OMe (N,N'-bis(3-methoxysalicylidene)-1,2-diaminoethane) (0.05 g, 0.152 mmol) and $Ni(OAc)_2$ (0.038 g, 0.152 mmol) to give 47 mg product (80.2% yield). ESI mass spectrometry: Calculated m/z for Ni(salen-OMe): 407.05. Found: 407.05. $^1$H NMR (500 MHz, $CD_3CN$) δ 7.69 (s, 2H), 6.83 (d, 2H), 6.79 (d, 2H), 6.49 (t, 2H), 3.78 (s, 6H), 3.41 (s, 4H).

**$2Ni^{II}Na(OTf)$:** Synthesized using method 2.1 with **1Na(OTf)** (0.010 g, 0.017 mmol) and $Ni(OAc)_2$ (0.003 g, 0.017 mmol) to give 0.009 g product (66.6% yield). ESI mass spectrometry: Calculated m/z for (**$2Ni^{II}Na(OTf)$-$CF_3SO_3$]$^+$**: 493.09. Found: 493.09. Analytical calculation for $C_{23}H_{24}NaNiF_3O_9N_2S$: C, 42.95; H, 3.76; N, 4.36. Found: C, 42.95; H, 3.70; N, 4.19. $^1$H NMR (500 MHz, $CD_3CN$) δ 7.77 (s, 2H), 6.95 (d, 2H), 6.90 (d, 2H), 6.62 (t, 2H), 4.07 (t, 4H), 3.84 (t, 4H), 3.72 (s, 4H), 3.47 (s, 4H).

**$2Ni^{II}Ba(OTf)_2$:** Synthesized using method 2.1 with **$1Ba(OTf)_2$** (0.050 g, 0.059 mmol) and $Ni(OAc)_2$ (0.0146 g, 0.059 mmol) to give 0.042 g product (80% yield). ESI mass spectrometry:

Calculated m/z for **2Ni$^{II}$Ba(OTf)**$^{+}$ : 756.96. Found: 756.95. Analytical calculation for $C_{24}H_{24}BaNiF_6O_{12}N_2S_2$: C, 31.80; H, 2.67; N, 3.09. Found: C, 31.93; H, 2.67; N, 3.01. $^1$H NMR (500 MHz, $CD_3CN$) δ 7.80 (s, 2H), 7.04 (t, 4H), 6.75 (t, 2H), 4.24 (t, 4H), 3.97 (t, 4H), 3.87 (s, 4H), 3.49 (s, 4H)

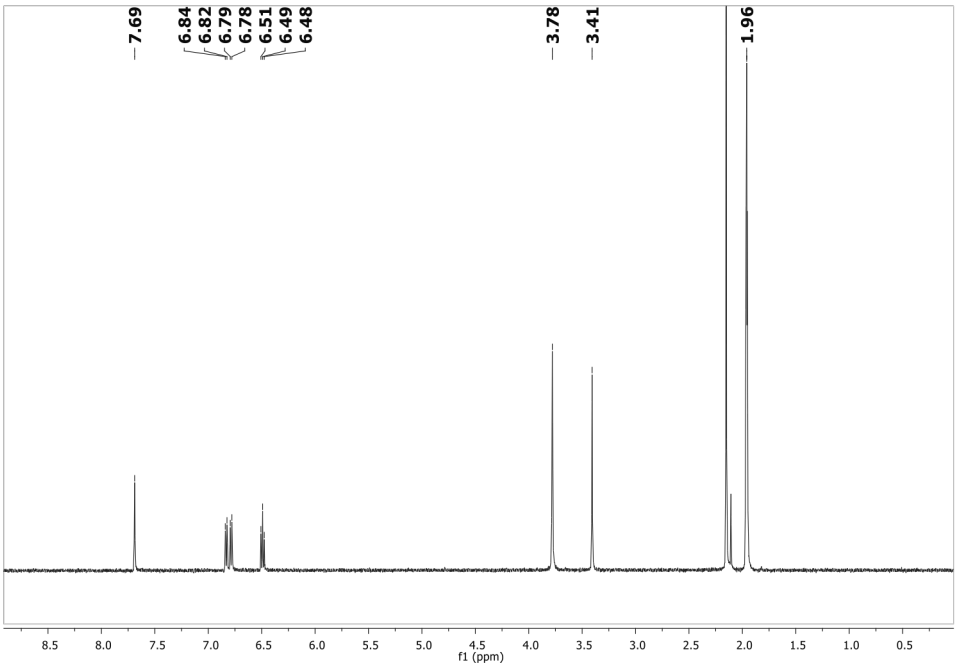


**Figure 2.10:** $^1$H NMR spectrum of Ni(salen-OMe) in $CD_3CN$.

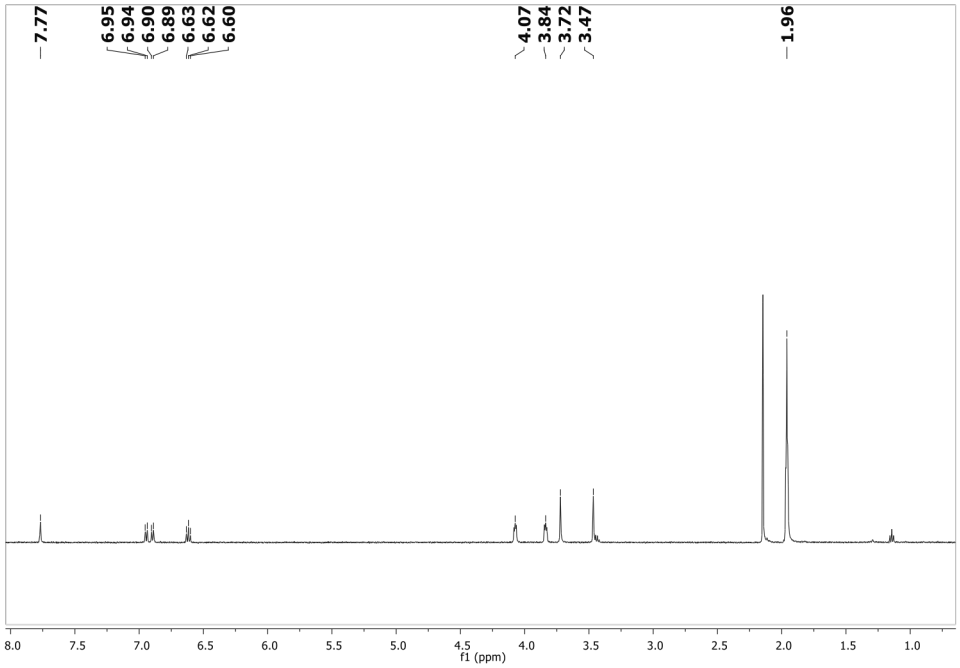


**Figure 2.11:** $^{1}$H NMR spectrum of **2Ni$^{II}$Na(OTf)** in $CD_3CN$.

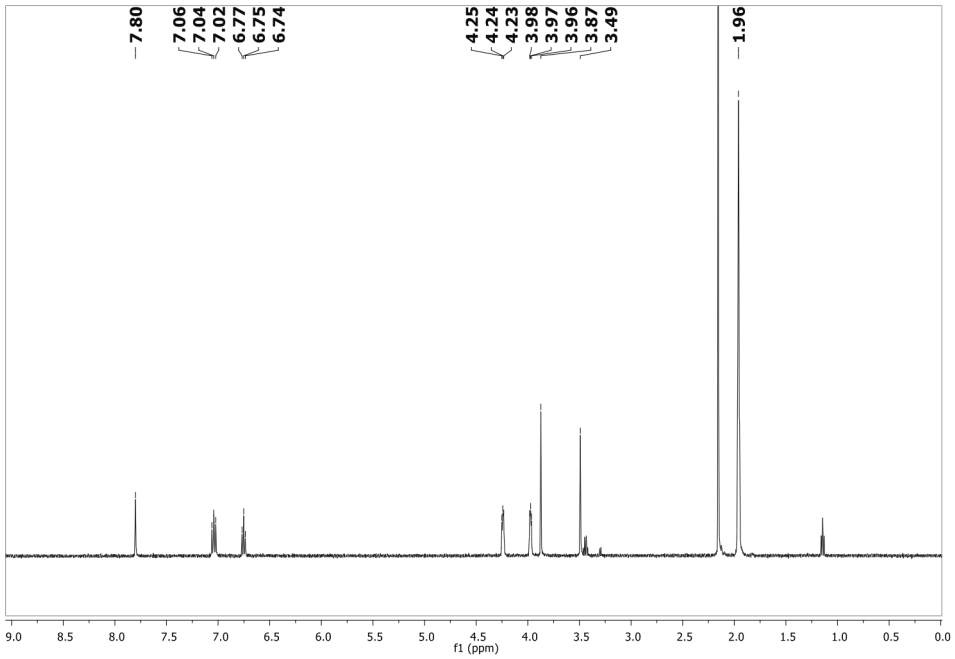


**Figure 2.12:** $^{1}$H NMR spectrum of **2Ni$^{II}$Ba(OTf)$_2$** in $CD_3CN$.

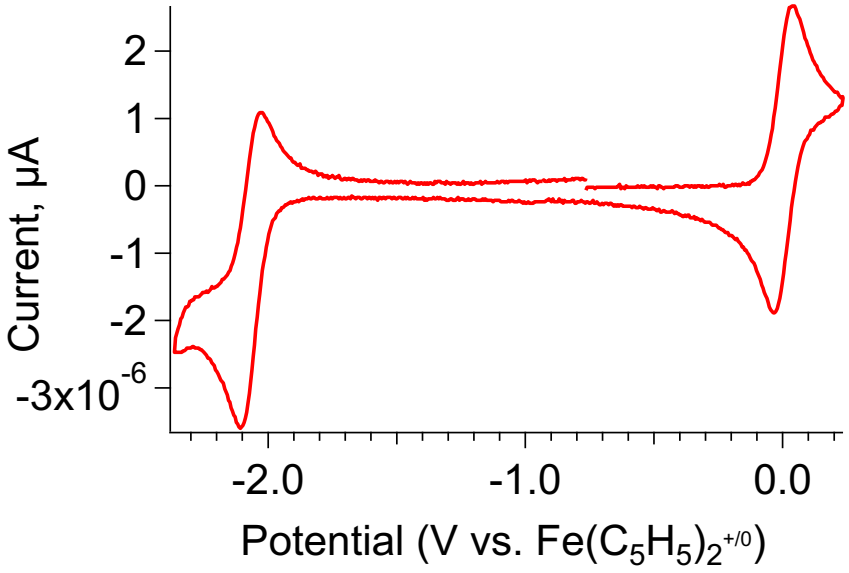


**Figure 2.13:** Cyclic voltammogram of Ni(salen-OMe) in acetonitrile.

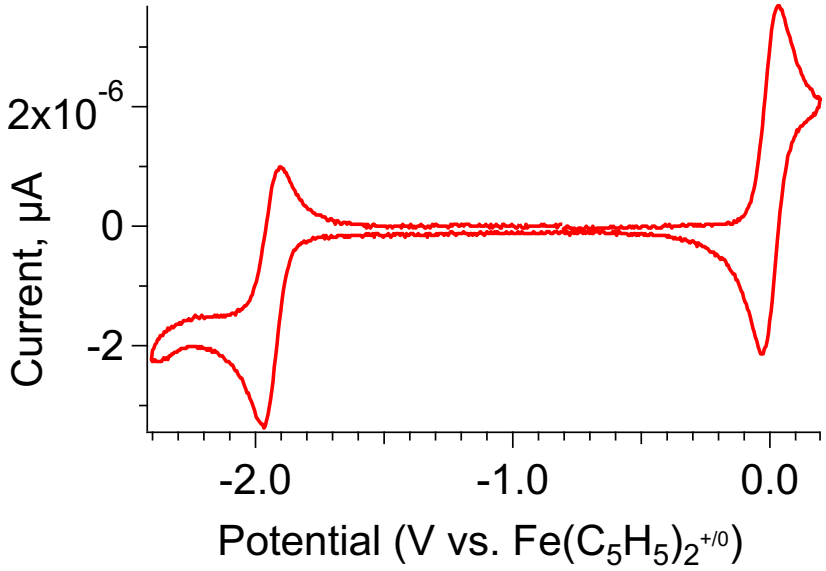


**Figure 2.14:** Cyclic voltammogram of **2Ni$^{II}$Na(OTf)** in acetonitrile.

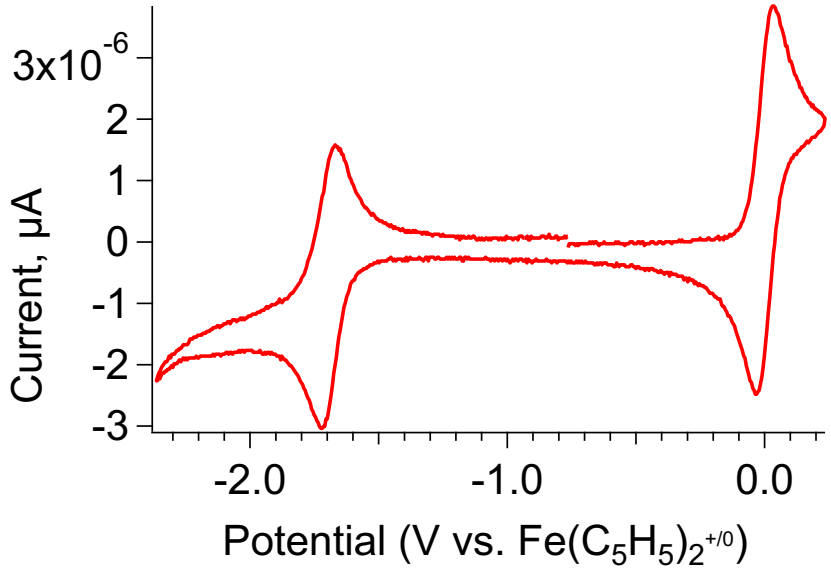


**Figure 2.15:** Cyclic voltammogram of **$2Ni^{II}Ba(OTf)_2$** in acetonitrile.

**Infrared Spectra**

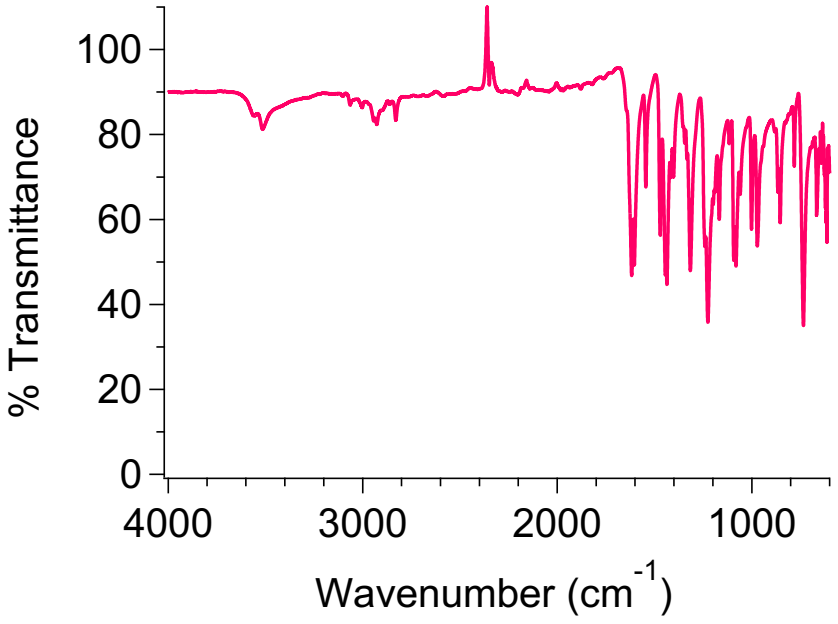


**Figure 2.16:** Solid state infrared spectrum of Ni(salen-OMe).

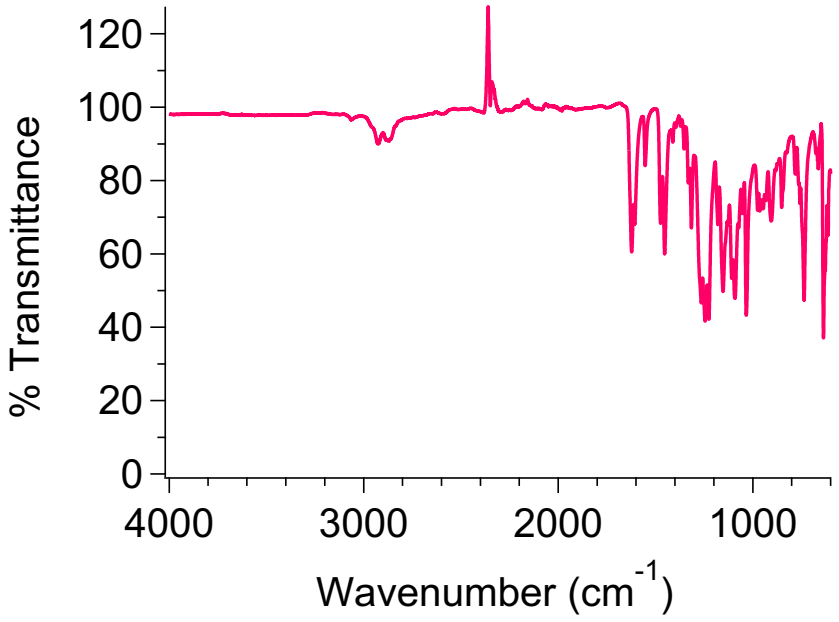


**Figure 2.17:** Solid state infrared spectrum of **2Ni$^{II}$Na(OTf)**.

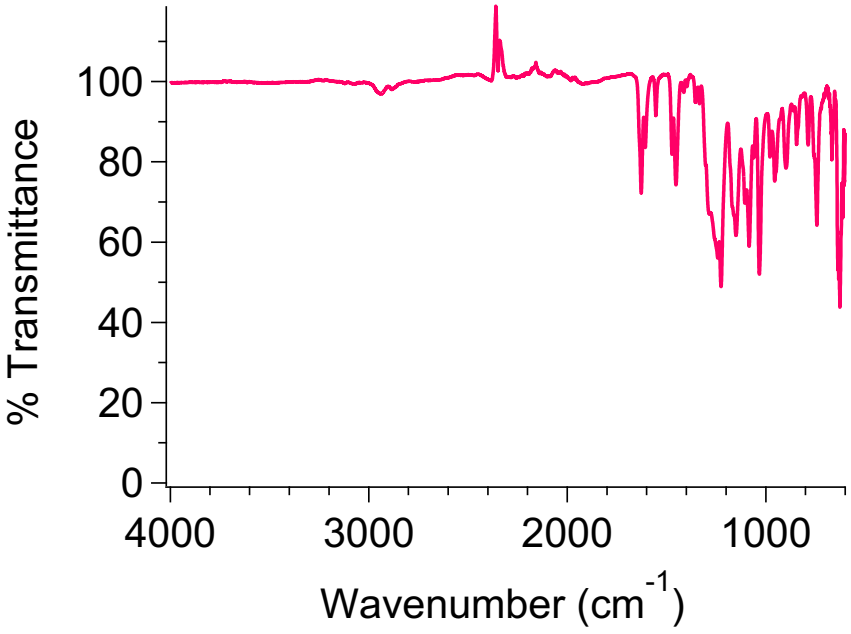


**Figure 2.18:** Solid state infrared spectrum of **2Ni$^{II}$Ba(OTf)$_2$**.

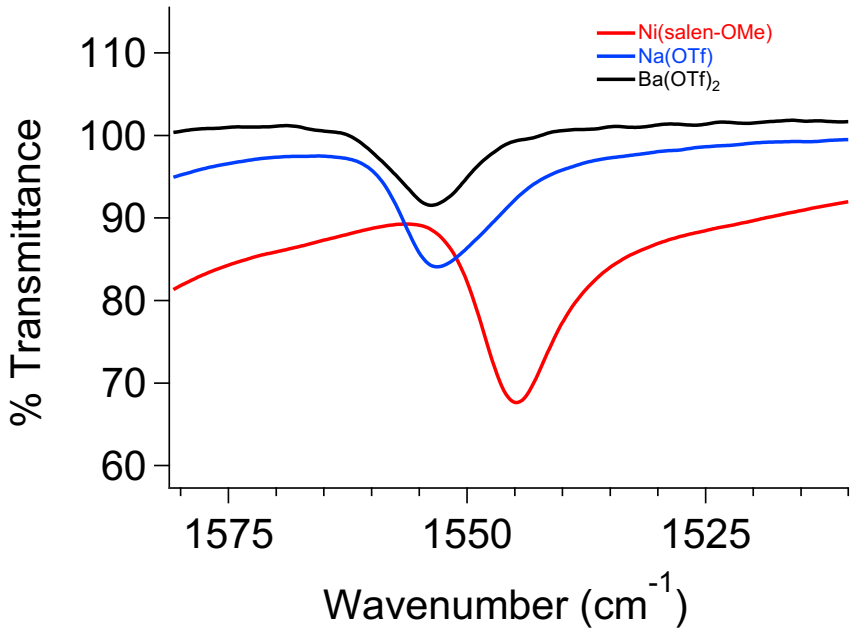


**Figure 2.19:** Overlay of the C=N vibrational stretches of complexes.

## 2.6 References

1. Morgenstern, A.; Jaszai, M.; Eberhart, M. E.; Alexandrova, A. N., *Chem. Sci.* **2017,** *8* (7), 5010-5018.

2. Major, D. T., *ACS Catal.* **2017,** *7* (8), 5461-5465.

3. Barrachin, B.; de Lara, E. C., *Journal of the Chemical Society, Faraday Transactions 2: Molecular and Chemical Physics* **1986,** *82* (11), 1953-1966.

4. Chantarojsiri, T.; Ziller, J. W.; Yang, J. Y., *Chem. Sci.* **2018,** *9* (9), 2567-2574.

5. Van Staveren, C. J.; Van Eerden, J.; Van Veggel, F. C. J. M.; Harkema, S.; Reinhoudt, D. N., *J. Am. Chem. Soc.* **1988,** *110* (15), 4994-5008.

6. Liu, D.-F.; Lü, X.-Q.; Lu, R., *Transition Met. Chem.* **2014,** *39* (6), 705-712.

7. Ayikoe, K.; Butcher, R. J.; Gultneh, Y., *Acta Crystallogr. Sect. E: Struct. Rep. Online* **2011,** *67* (3), m328.

8. Reath, A. H.; Ziller, J. W.; Tsay, C.; Ryan, A. J.; Yang, J. Y., *Inorg. Chem.* **2017,** *56* (6), 3713-3718.

9. Hipp, C. J.; Baker, W. A., *J. Am. Chem. Soc.* **1970,** *92* (4), 792-798.

10. Bosnich, B., *J. Am. Chem. Soc.* **1968,** *90* (3), 627-632.

11. Chai, J.-D.; Head-Gordon, M., *Phys. Chem. Chem. Phys.* **2008,** *10* (44), 6615-6620.

12. Weigend, F.; Ahlrichs, R., *Phys. Chem. Chem. Phys.* **2005,** *7* (18), 3297-3305.

13. Marenich, A. V.; Cramer, C. J.; Truhlar, D. G., *The Journal of Physical Chemistry B* **2009,** *113* (18), 6378-6396.

14. Frisch, M. J.; Trucks, G. W.; Schlegel, H. B.; Scuseria, G. E.; Robb, M. A.; Cheeseman, J. R.; Scalmani, G.; Barone, V.; Petersson, G. A.; Nakatsuji, H.; Li, X.; Caricato, M.; Marenich, A. V.; Bloino, J.; Janesko, B. G.; Gomperts, R.; Mennucci, B.; Hratchian, H. P.; Ortiz, J. V.; Izmaylov, A. F.; Sonnenberg, J. L.; Williams; Ding, F.; Lipparini, F.; Egidi, F.; Goings, J.; Peng, B.; Petrone, A.; Henderson, T.; Ranasinghe, D.; Zakrzewski, V. G.; Gao, J.; Rega, N.; Zheng, G.; Liang, W.; Hada, M.; Ehara, M.; Toyota, K.; Fukuda, R.; Hasegawa, J.; Ishida, M.; Nakajima, T.; Honda, Y.; Kitao, O.; Nakai, H.; Vreven, T.; Throssell, K.; Montgomery Jr., J. A.; Peralta, J. E.; Ogliaro, F.; Bearpark, M. J.; Heyd, J. J.; Brothers, E. N.; Kudin, K. N.; Staroverov, V. N.; Keith,

T. A.; Kobayashi, R.; Normand, J.; Raghavachari, K.; Rendell, A. P.; Burant, J. C.; Iyengar, S. S.; Tomasi, J.; Cossi, M.; Millam, J. M.; Klene, M.; Adamo, C.; Cammi, R.; Ochterski, J. W.; Martin, R. L.; Morokuma, K.; Farkas, O.; Foresman, J. B.; Fox, D. J. *Gaussian 16 Rev. D.01*, Wallingford, CT, 2016.

15. Front Matter A2 - PERRIN, D.D. In *Ionisation Constants of Inorganic Acids and Bases in Aqueous Solution (Second Edition)*, Pergamon: **1982**; p iii.

16. Dreuw, A.; Head-Gordon, M., *Chem. Rev.* **2005,** *105* (11), 4009-4037.

17. APEX2 Version 2014.11-0, Bruker AXS, Inc.; Madison, WI 2014.

18. SAINT Version 8.34a, Bruker AXS, Inc.; Madison, WI 2013.

19. Sheldrick, G. M. SADABS, Version 2014/5, Bruker AXS, Inc.; Madison, WI 2014. .

20. Sheldrick, G. M. SHELXTL, Version 2014/7, Bruker AXS, Inc.; Madison, WI 201. .

21. International Tables for Crystallography 1992, Vol. C., Dordrecht: Kluwer Academic Publishers.

# CHAPTER 3

# THE ROLE OF ELECTROSTATIC EFFECTS ON THE REACTIVITY OF MANGANESE NITRIDE SCHIFF BASE COMPLEXES

Portions of this chapter have been published: Chantarojsiri, T.; Reath, A. H.; Yang, J. Y. *Angew. Chem. Int. Ed.* **2018**, *57*, 14037. Reproduced with permission from John Wiley and Sons.

The manganese nitride coupling studies presented in this chapter were part of a collaborative body of work by Dr. Teera Chantarojsiri and myself.

### 3.1. Motivation and Specific Aims

In this chapter, $Mn^{III/II}$ and $Mn^{V}N$ Schiff- base complexes incorporating a $K^+$ or $Ba^{2+}$ ion in the ligand framework are used in various reactivity studies to explore the effects of electrostatic interactions. Recent studies found metal-based, one-electron oxidation of $Mn^{V}N$ Schiff-base complexes results in bimolecular coupling to form $N_2$ and the corresponding $Mn^{III}$ complexes.[1-2] Installation of electron-withdrawing functional groups on the ligand results in more oxidizing $Mn^{VI}N$ complexes that couple to form $N_2$ at a higher rate.[1] Subsequent studies demonstrate how cationic charge affects the inverse free energy relationship for bimolecular coupling compared to the use of ligand functionalization. Brief experiments were also undertaken in attempt to exploit the increased stability of the $Mn^{VI}N$ species to apply towards useful reactions such as C-H bond activation. Further reactivity explored herein investigates the potential for electrochemical ammonia oxidation using $Mn^{III}$ Schiff base complexes, as well as the effect of proximal electrostatic fields on the acid/base chemistry of the $Mn^{V}N$ species.

### 3.2. Background

High-valent transition metal nitride complexes play a diverse role in catalytic and stoichiometric reactivity.[3-37] Their reactivity is dictated by their nucleophilic or electrophilic character, which is in turn dependent on the identity of the metal, oxidation state, and ligand environment.[3-6, 38-51] Although nucleophilic $Mn^{V}N$(salen) complexes have been studied for several decades,[52-68] Storr[1] and Menard[2] recently uncovered a new reactivity pattern. One-electron oxidation of the $Mn^{v}N$(salen) derivatives **A**, **B**, **C**, and **D** (Figure 3.1) was pursued to generate a metal nitride with radical character. However, the resulting $Mn^{VI}N$(salen) complex was unstable,

engaging in bimolecular coupling to form $N_2$ and two equivalents of the corresponding $Mn^{III}$(salen) complex (eq 3.1). Bimolecular $N_2$ evolution had also previously been observed in Schiff base $Ru^{VI}$ [69-70] and $Os^{VI}$ [71] nitride complexes.

(eq 3.1) 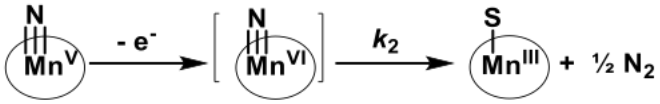


Storr et. al. explored the effect of ligand substituents on the rate of N–N bond formation (complexes **B**, **C**, and **D** in Figure 3.1). More electron-withdrawing groups led to more positive oxidation potentials in accordance with their Hammett parameters.[1] The $Mn^{V}$N salen with the most electron-donating substituent, $NMe_2$ (**B** in Figure 3.1), led to a ligand-centered radical upon oxidation and no bimolecular reactivity, whereas Mn-based one-electron oxidation of **C** and **D** in Figure 3.1 led to $N_2$ evolution (eq 3.1). Not surprisingly, the most oxidizing $Mn^{VI}$nitride complex (**D**) reacts at the highest rate ($k_2$ in eq 3.1). Thus, installation of electron-withdrawing substituents to produce a more oxidizing $Mn^{VI}$ nitride complex also results in an increased rate of bimolecular coupling.

The synthesis and characterization of $Mn^{V}N$ (**1K**, **1Na**, **1Ba, 1Sr**) and $Mn^{III}$ (**2K**, **2Ba**) complexes with appended $K^+$ and $Ba^{2+}$ cations are, shown in Figure 3.1. Similar to their Co and Fe analogue, the $Mn^{V}N$ complexes incorporating a $K^+$ or $Ba^{2+}$ ion exhibit a positive shift in the $Mn^{V/VI}N$ reduction potential. Oxidation of **1K, 1Na, 1Sr,** and **1Ba** also results in $Mn^{VI}N$ complexes that reductively couple to form $N_2$ according to eq 3.1. However, the stability of the $Mn^{VI}N$ is enhanced with increasing cationic charge. As a result, the most stable $Mn^{VI}N$ complex to bimolecular coupling is also the most oxidizing – the opposite trend to what is observed through electron-donating or withdrawing substituent ligand modifications.

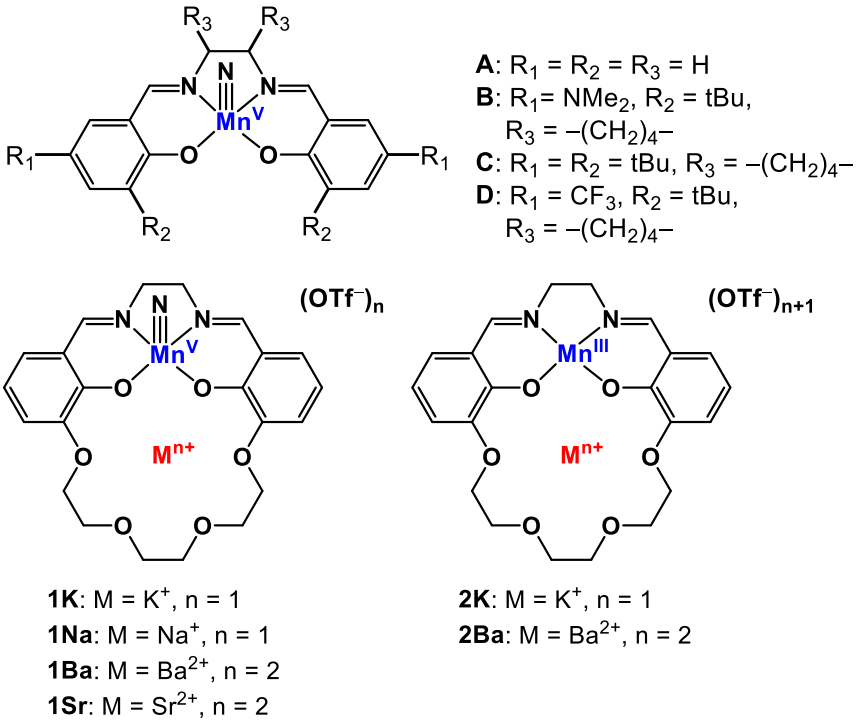


**Figure 3.1:** The reactivity of A (ref. 2) and B, C, and D (ref. 1) has previously been described. The reactivity of 1K, 1Ba, 1Na, and 1Sr compared to A are discussed in this work.

The inhibition of bimolecular coupling using electrostatic interactions offers an opportunity to exploit the activated radical nitride of the $Mn^{VI}N$ species for more useful applications. Activated metal nitrides are known to participate in a wide range of reactivity including olefin amination[60, 72] and aziridation,[53, 57, 73] N-atom transfer to metal complexes,[67] and C–H bond activation.[74] Shutting down the pathway towards N–N coupling would demonstrate the use of electrostatic charge to reduce undesirable catalyst deactivation pathways involving bimolecular steps, such as those observed in olefin metathesis.[72, 75] An attempt to initiate C-H bond activation with $Mn^{VI}N$ complexes using dihydroanthracene as a substrate is explored in later sections of this report. Additionally, the imido species generated from the protonation of $Mn^{V}N$ Schiff base compounds are known to decompose through a bimolecular pathway. This reactivity was also explored to determine whether a stabilized $Mn^{V}NH$ could be generated, as well as to better understand the effects of electrostatic interactions on the p$K_a$ and bond dissociation free energies (BDFE) of metal-bound substrates.

### 3.3 Results and Discussion

#### 3.3.1 Synthesis and Characterization

**Synthetic Methods**

Synthesis of the $Mn^{III}$ complexes **1M** and **2M** ($M = K^+$ or $Ba^{2+}$, Figure 3.1) was adapted from a literature procedure[76,77] by Dr. Teera Chantarojsiri as outlined in a previous publication.[78] The corresponding $Mn^{V}$ nitrides, **1M** (Figure 3.1), were synthesized from **2M** by reaction with $NH_4OH$ followed by bleach (NaOCl). Additional equivalents of the respective metal triflate salts, K(OTf) and $Ba(OTf)_2$, were added to ensure the occupancy of desired cations residing in the crown

ether pocket. **1M** (M = $Na^+$ or $Sr^{2+}$) was synthesized following a similar procedure but without first isolating their respective $Mn^{III}$ precursors. The $Mn^{V}N$ complexes were recrystallized by $Et_2O$ diffusion into concentrated $CH_3CN$ solution. $Mn^{III}$(salen)OTf (salen = N,N′-bis(salicylidene)ethylenediamine) and $Mn^{V}N$(salen) (**A**) were prepared as previously reported.[60] The purity and formulation of the complexes were confirmed using mass spectrometry and elemental analysis.

**Solid State Structures**

Crystals of **1M** (M = $K^+$ or $Ba^{2+}$) and **2Ba** suitable for single crystal X-ray crystallography were grown by $Et_2O$ diffusion into a concentrated $CH_3CN$ solution. (Crystals of **2K** for structural characterization were isolated after oxidation of **1K**, *vide infra*). Selected bond metrics and structural parameters are listed in Table 3.1 and the ORTEPs are shown in Figure 3.2. The $\tau_5$ values for **A**, **1K**, and **1Ba** are 0.086, 0.110, and 0.203, respectively, where a $\tau_5$ of 0 represents an ideal square pyramidal coordination geometry and a $\tau_5$ of 1 an ideal trigonal bipyramidal geometry. Although the coordination geometry of the Mn ion can be described as square pyramidal in all of the structures, the geometry becomes more distorted as the charge of M increases.

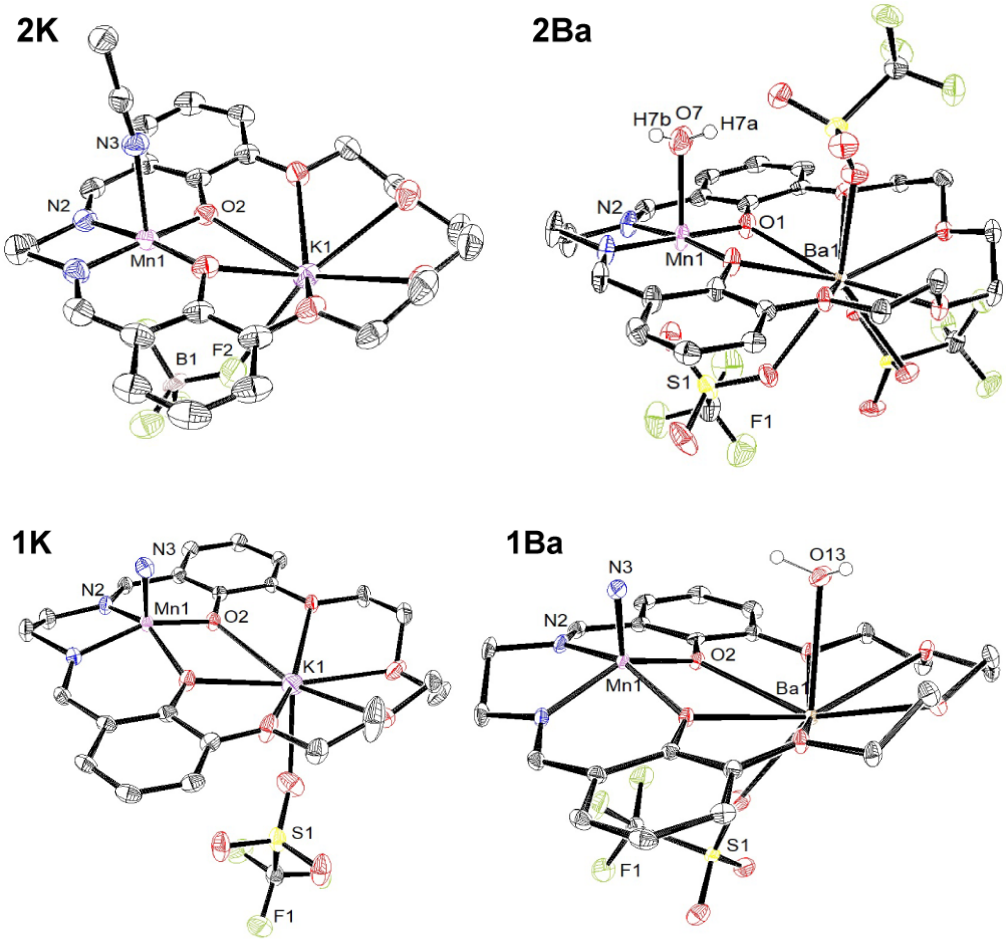


**Figure 3.2:** ORTEP representations of solid-state structures of **1K**, **1Ba**, **2K**, and **2Ba**. Outer-sphere anions are omitted for clarity. Hydrogen atoms are only depicted in water molecules.

## UV-vis Spectroscopy

The electronic absorption for MnN(salen) (**A**), **1K**, **1Na**, **1Ba** and **1Sr** have identical bands at 596 nm ($\epsilon$ = 200 $M^{-1}$ $cm^{-1}$) that we assign as a *d-d* transition (Table 3.1 and Figure 3.3). The similar profiles indicate minimal changes in electronic structure across the series.

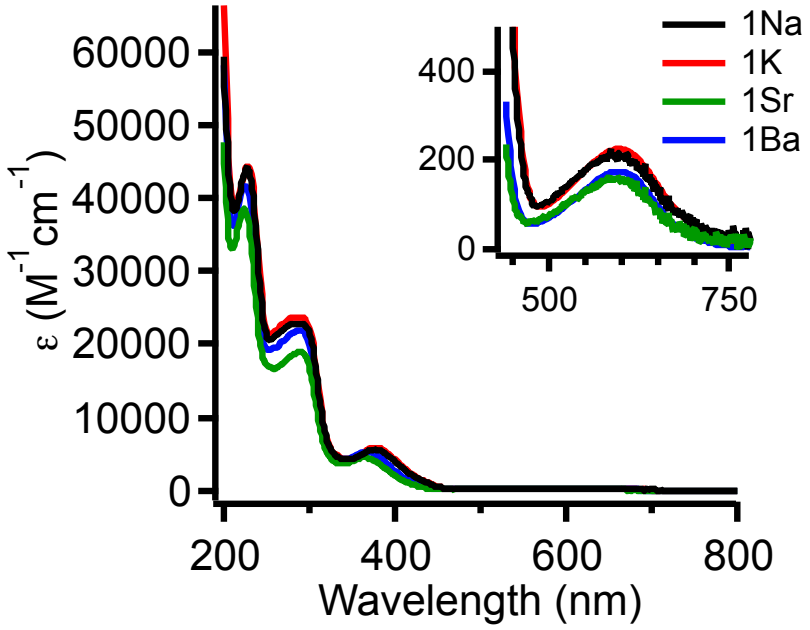


**Figure 3.3:** UV-vis spectra of **1M** complexes. Magnified view of d-d bands shown in the inset

**Infrared Spectroscopy**

The Mn≡N stretch of **1K**, **1Na**, **1Ba**, and **1Sr** is 1050, 1052, 1055, and 1058 $cm^{-1}$, respectively, compared to 1047 $cm^{-1}$ in MnN(salen) (**A**) (Figure 3.4).[52] The Mn≡N vibrational frequency for **A** is consistent with previously reported MnN species and is slightly higher for **1M**.

Vibrational spectroscopy and structural details from these studies and previously reported complexes MnN complexes are compiled in Table 3.2.

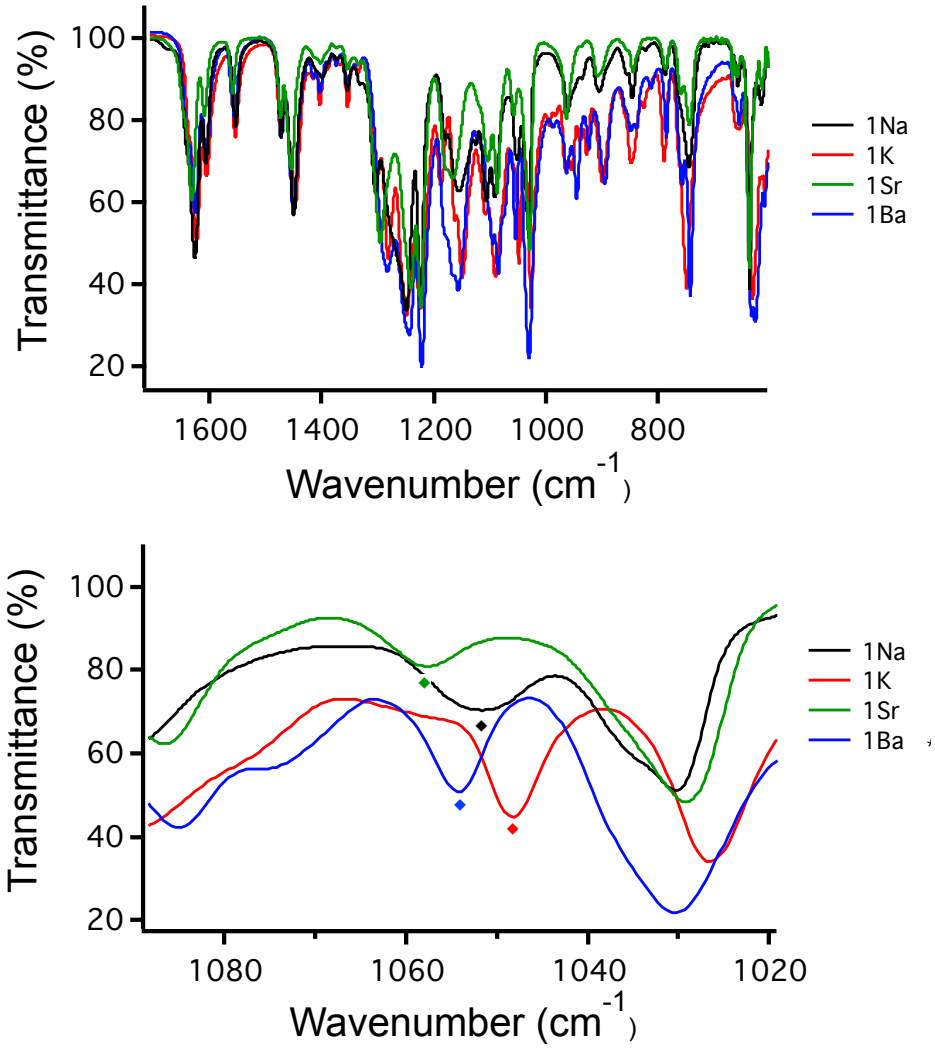


**Figure 3.4:** Top: Infrared spectra of **1M** complexes. Bottom: Expanded view to trend in Mn≡N stretching frequency.

**Table 3.1:** Selected bond metrics, redox properties, vibrational frequencies, and UV-visible absorption parameters. Kinetic and thermodynamic parameters extrapolated from Eyring plots in Figure 3.9.

| | Mn≡N bond distance (Å) | Mn—M distance (Å) | $\tau_5$ | ν (Mn≡N) ($cm^{-1}$) | *λ (d-d*, nm), ε ($M^{-1}$ $cm^{-1}$) | $E_{1/2}$ $Mn^{V/VI}$(V vs $[Fe(C_5H_5)_2]^{+/0}$) | $k_2$ (20 °C, $M^{-1}$ $s^{-1}$) | $\Delta H^{‡}$ (kcal /mol ) | $\Delta S^{‡}$ (e.u.) |
|---|---|---|---|---|---|---|---|---|---|
| MnN(salen ) (**A**) | 1.512(3) [a] | – | 0.086 [a] | 1047[a] | 596, 200 | 0.427 | 2166 | 1.75 | 37.21 |
| **1K** | 1.528(2) | 3.7864(8) | 0.110 | 1050 | 596, 200 | 0.616 | 857 | 2.14 | 37.71 |
| **1Na** | – | – | – | 1052 | 596, 185 | 0.591 | 684 | – | – |
| **1Ba** | 1.5287(17) | 3.7959(4) | 0.203 | 1055 | 596, 200 | 0.805 | 99.7 | 6.47 | −27.63 |
| **1Sr** | – | – | – | 1058 | 596, 223 | 0.880 | 87.0 | – | – |
| **2K** | – | 3.6893(11 ) | 0.002 | – | 521, 890 | – | – | – | – |
| **2Ba** | – | 3.7217(4) | 0.071 | – | 500, 700 | – | – | – | – |

[a]From ref 50

### 3.3.2 Electrochemical studies

#### Cyclic Voltammetry

The electrochemical properties of the $Mn^{V}N$ complexes in acetonitrile were measured using cyclic voltammetry. Scan-rate dependent data for all complexes are shown in Figure 3.5. The cathodic and anodic peak separation ($\Delta E_p$) for the $Mn^{VI/V}$ redox couple of **A** and **1M** increases with the scan-rate (Table 3.3 and 3.4). An increasing $\Delta E_p$ with scan-rate indicates the rate of electron transfer is slow under these conditions, or the redox event is quasi-reversible.[79] In all

cases, the current increases linearly with the square root of the scan rate, indicating electron transfer is under diffusion control (Figure 3.6). $E_{1/2}$ values can be accurately obtained using the midpoint potential of quasi-reversible redox events.[79] The $Mn^{V/VI}$ reduction potentials for **A**, **1K**, **1Na**, **1Ba** and **1Sr** are 0.427, 0.616, 0.591, 0.805, and 880 V versus $Fe(C_5H_5)_2^{+/0}$, respectively (Table 1).

The similar electronic structure and accompanying increase in redox potential between **A** and **1M** is likely due to an electric field potential from the cation, which we have characterized in other metal complexes with this ligand framework, described previously in Chapters 1 and 2 of this report.[76, 80] We previously demonstrated we can estimate the magnitude of the electrostatic effect by modelling the non-redox active cation as a point charge.[76] By this model, the electric field potential at Mn is dependent on the point charge *q* (1 for $K^+/Na^+$ and 2 for $Ba^{2+}/Sr^{2+}$) and its distance (r) from Mn. For **1K** and **2Ba**, the distance r is nearly the same in the solid state (Table 1), and each sequential increase in charge leads to a positive shift in the reduction potential of 189 mV. The doubling of the positive shift in redox potential between **1K** and **1Ba** relative to **A** is consistent with a doubling of the electric field potential from a monocation to a dication.

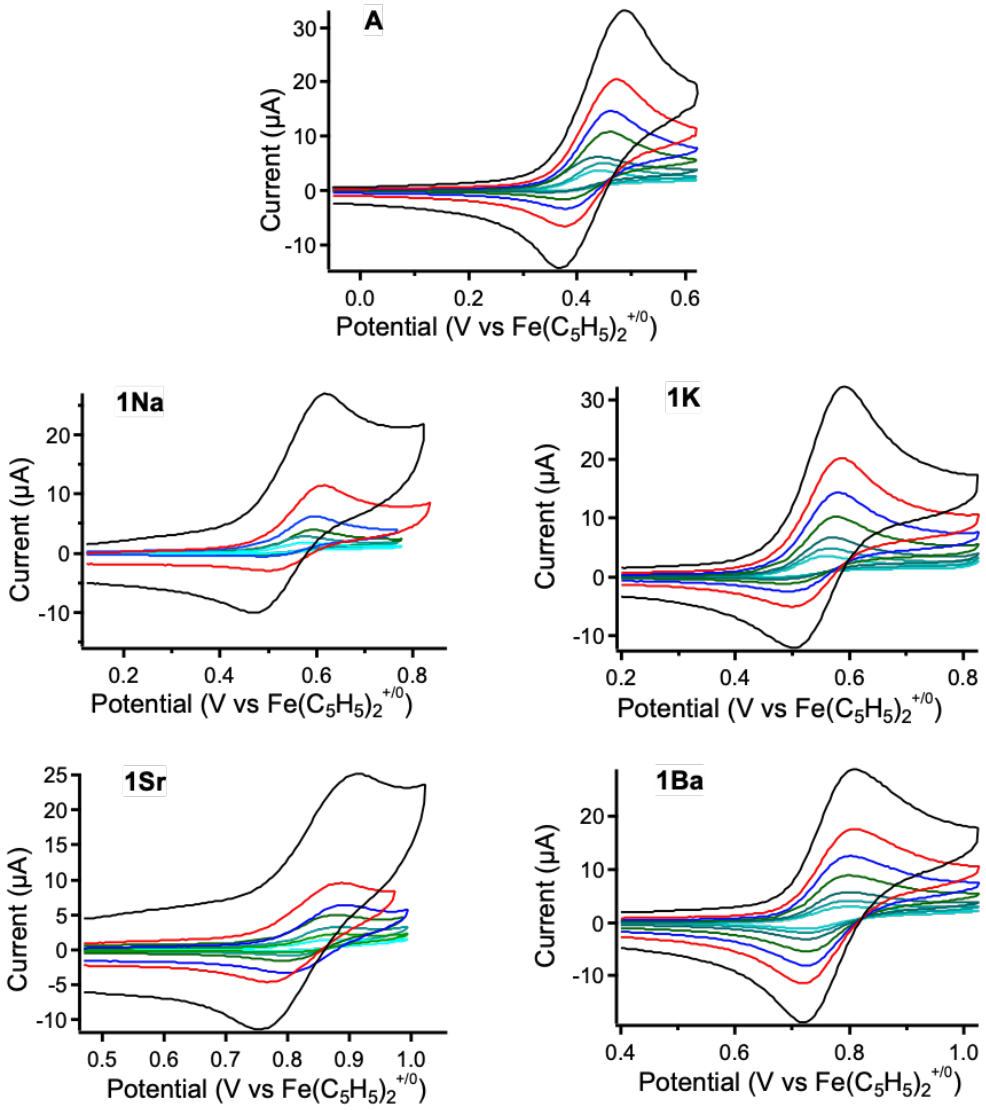


**Figure 3.5:** Scan-rate dependent cyclic voltammetry of **A** (top), **1Na** (middle left) and **1K** (middle right), **1Sr** (bottom left) and **1Ba** (bottom right) with scan rate ranging from 25 mV/s to 1000 mV/s.

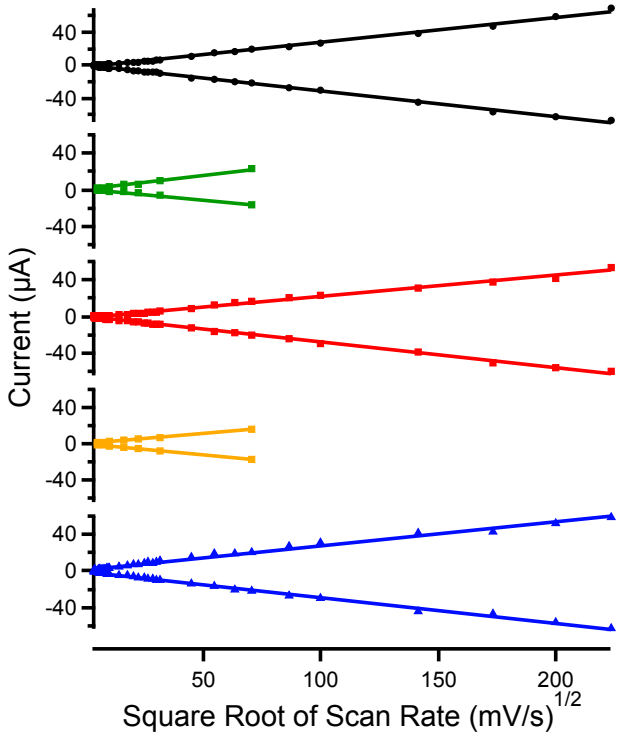


**Figure 3.6:** Plot of current versus square root of scan rate of Mn(N)salen (**1**) (black, $R^2$ = 0.985, 0.990), **1Na** (green, $R^2$ = 0.982, 0.992) **1K** (red, $R^2$ = 0.991, 0.993), **1Sr** (orange, $R^2$ =0.999, 0.999) and **1Ba** (blue, $R^2$ = 0.988, 0.990). All show a linear relationship, indicating that $Mn^{V/VI}N$ reduction processes are diffusion limited.

### 3.3.3 N–N Coupling Kinetic Studies

Chemical oxidation was used to characterize the oxidized product and determine whether the electron transfer is metal or ligand based. Although aminium cations have previously been used to oxidize $Mn^{V}$ nitrides,[1] their solubility properties and stability in acetonitrile preclude their

use with **1K** and **1Ba**. Nitrosonium or thianthrenium cations were employed instead. Addition of the chemical oxidant into a thawing $CH_3CN$ solution of **1K** or **1Ba** and quick mixing at low temperature allowed characterization of the oxidized species by perpendicular mode EPR. The EPR spectra of both species taken at 77 K showed a six-line pattern with a g value around 2, signifying a radical residing on an atom with a nuclear spin of 5/2 (Figure 3.7) and consistent with a $Mn^{VI}$ species.[38, 40]

The EPR and UV-visible spectroscopic experiments with **1K** and **1Ba** indicate the **1M** derivatives behave in a chemically similar fashion as the previously reported MnN(salen) derivatives. One electron oxidation results in a putative $Mn^{VI}N$ species which can couple to form $N_2$ and regenerate the $Mn^{III}$ species as shown in eq 3.1.

The one-electron oxidation of **A** or **1M** followed by bimolecular coupling represents an EC mechanism (electron transfer followed by a chemical step), which is evident in the scan-rate dependent cyclic voltammograms (Figure 3.5, top). At scan rates slow relative to the chemical step (observed with **A** and **1K** in Figure 2 and **1Na** in 3.8), no corresponding reduction event is observed after oxidation (or electrochemical oxidation is irreversible due to the chemical step). Upon scanning to more negative potentials (Figure 3.8, bottom), a new reduction event appears that matches the $Mn^{III/II}$ couple from the independently prepared respective $Mn^{III}$ complexes. The redox event assigned to the $Mn^{III/II}$ couple is absent if $Mn^{V}N$ is not first oxidized before scanning anodically. At faster scan rates for **A**, **1K**, and **1Na** the anodic peak current ($i_a$) of the $MnN^{V/VI}$ couple increases relative to the cathodic peak current ($i_c$), (Table 3.3 and 3.4). At the highest scan rates for **A**, **1K**, and **1Na** $i_c/i_a$ approaches 1 but does not achieve unity. Thus, the $Mn^{III/II}$ couple

from the reaction product is still observed at the highest scan rates. For **1Ba** and **1Sr**, the $i_c/i_a$ is about 1 at all scan rates, indicating the chemical step is slow and consistent with an absence of a $Mn^{III/II}$ peak corresponding to product (Table 3.3). The turnaround potential for **1Sr** was taken slightly negative of **1Ba** (Figure 3.5), resulting in a shorter timeframe to evaluate the chemical step, but $i_c/i_a$ quickly becomes about 1 at scan rates of 100 mV/s and higher.

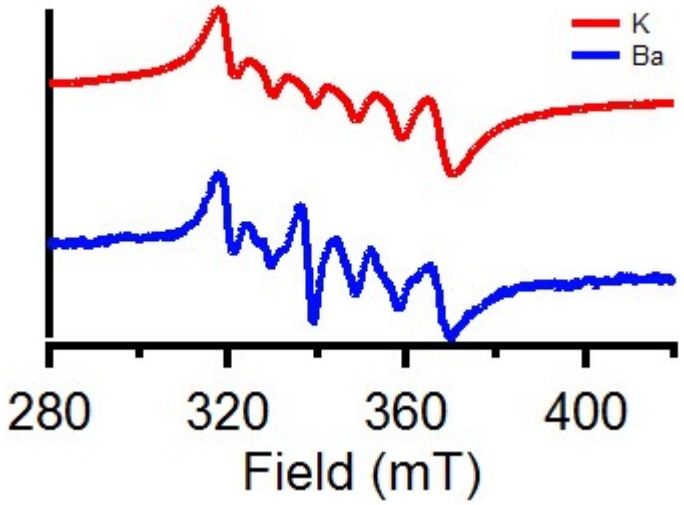


**Figure 3.7:** Perpendicular mode EPR spectra of oxidized 1K (red) and oxidized 1Ba (blue), as trapped intermediates in oxidation of 1K and 1Ba by $NO^+$ at 77K. Both spectra exhibit a g-value around 2, with a six-line pattern, indicating S = 1/2 radical that resides on a I = 5/2 Mn center. Residual $NO^+$ can be observed in the blue spectrum which causes it to deviate from an ideal six-line pattern.

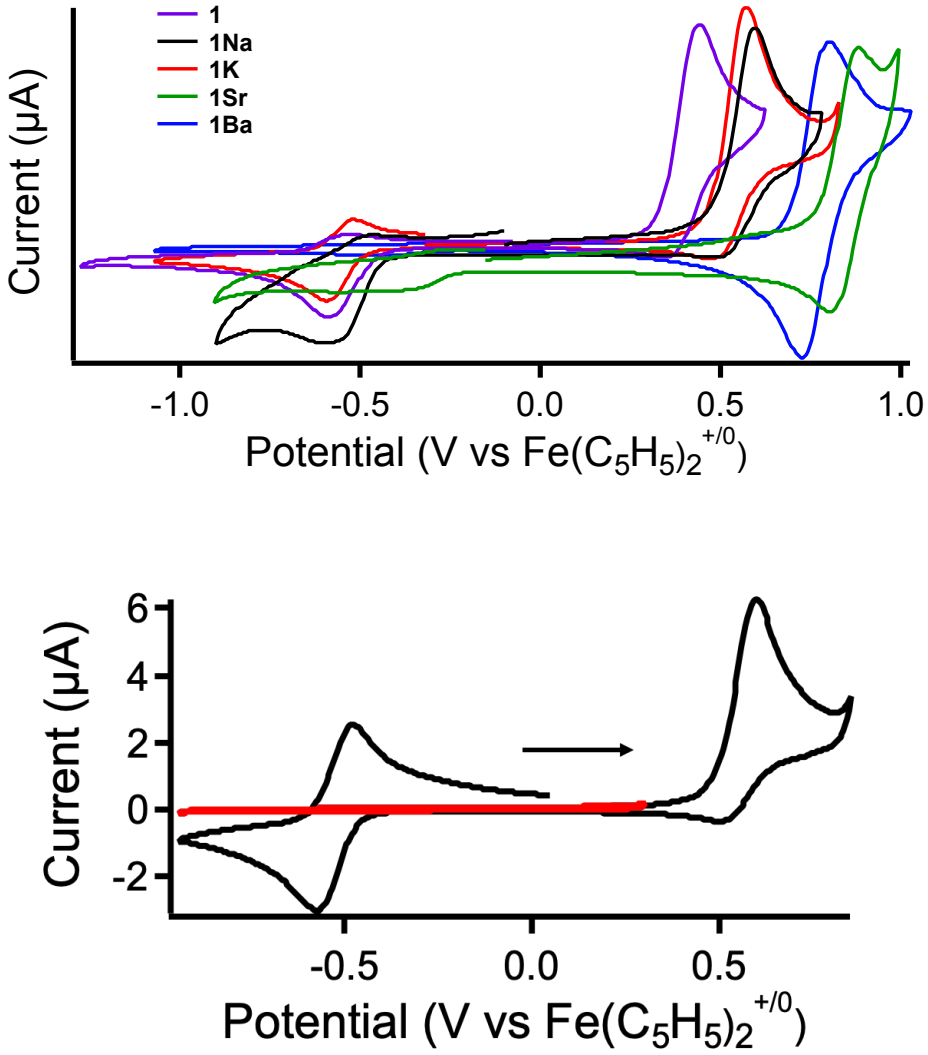


**Figure 3.8:** Top: Cyclic voltammetry of Mn(N)salen (**A**) (black), **1Na** (dark green), **1K** (red), **1Sr** (light green), and **1Ba** (blue), showing $Mn^{V/VI}N$ redox couple. Current values have been normalized as a visual aid. Bottom: Representative cyclic voltammetry for MnN(salen) (**A**) (black), and **1K** (red), showing absence of $Mn^{III/II}$ redox couple when oxidation of $Mn^{V}N$ to $Mn^{VI}N$ does not first occur**.** All cyclic voltammograms were taken at 100 mV/s.

The scan rate dependent cyclic voltammograms suggests the rate of the chemical step (N–N coupling) decreases from **A**, **1K/1Na**, and **1Ba/1Sr**. Slow electron transfer at high scan rates complicates determination of the reaction rate using cyclic voltammetry. As a result, we turned to UV-vis spectroelectrochemistry to measure the temperature dependent rate constants for the chemical step (Figure 3.10, 3.11, 3.13, and 3.14). MnN(salen) (**A**) and **1M** were oxidized *in situ* using a honeycomb electrode in a UV-visible spectroelectrochemical cell at a potential 200 mV positive of their respective oxidation potentials and the rate of $Mn^{III}$ formation was monitored.

At a temperature of 20 °C, the rates of N–N coupling for **1Sr**, **1Ba**, **1Na**, **1K**, and **A** are 87, 99.7, 684, 857, and 2166 $M^{-1}s^{-1}$, respectively. We have been unable to measure an equilibrium constant for cation occupancy in **1M** due to synthetic challenges in isolating analytically pure complexes without any cation present. However, addition of 10 equivalents of the salts $Ba(OTf)_2$ and K(OTf) to **1Ba** and **1K**, respectively, did not lead to any appreciable differences to the reversibility of the $Mn^{V/VI}$ redox couple (Figure 3.12). As a result, it is not likely that equilibria involving partial occupancy of the crown moiety plays a major role in the reaction rate.

The same experiment was repeated at -20, -10, 0, and 10 °C with **A, 1K**, and **1Ba**. An Eyring plot (see Table 3.1 and Figure 3.9) was used to derive the enthalpy ($\Delta H^{\ddagger}$) and entropy of activation ($\Delta S^{\ddagger}$). All three species have negative entropies of activation, suggesting an associative mechanism in the rate-determining step. The enthalpies of activation increase from **A** to **1K** to **1Ba**, which corresponds with our measured reaction rates.

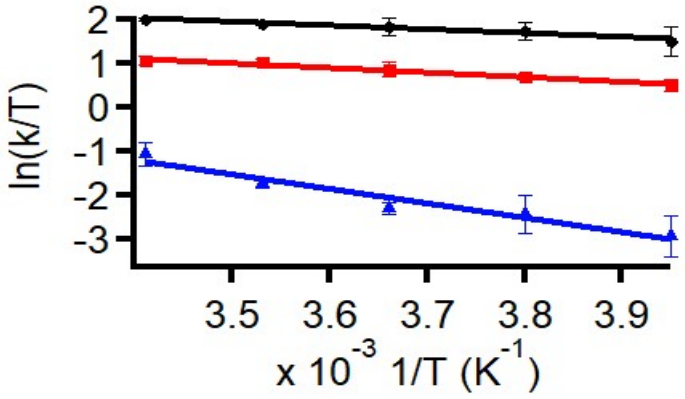


**Figure 3.9:** Eyring Plot of MnN(salen) (**A**) (black), **1K** (red), and **1Ba** (blue), showing linear relationships between ln(k/T), where k is a second-order rate constant and T is temperature in K, and 1/T, according to the Eyring equation:

$$ln\frac{k}{T} = \left(-\frac{\Delta H^{\ddagger}}{R} \times \frac{1}{T}\right) + ln\frac{k_B}{h} + \frac{\Delta S^{\ddagger}}{R}$$

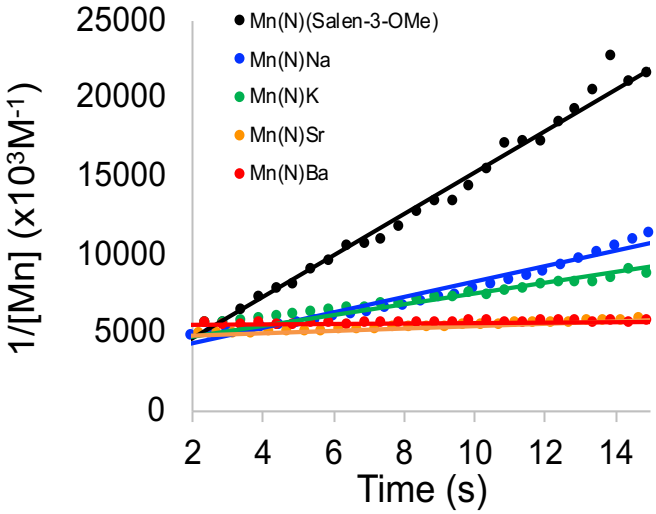


**Figure 3.10:** Kinetic trace of electrochemical oxidation of MnN(salen) (**A**) (black), **1K** (red), **1Ba** (blue) plotted according to a second-order rate law.

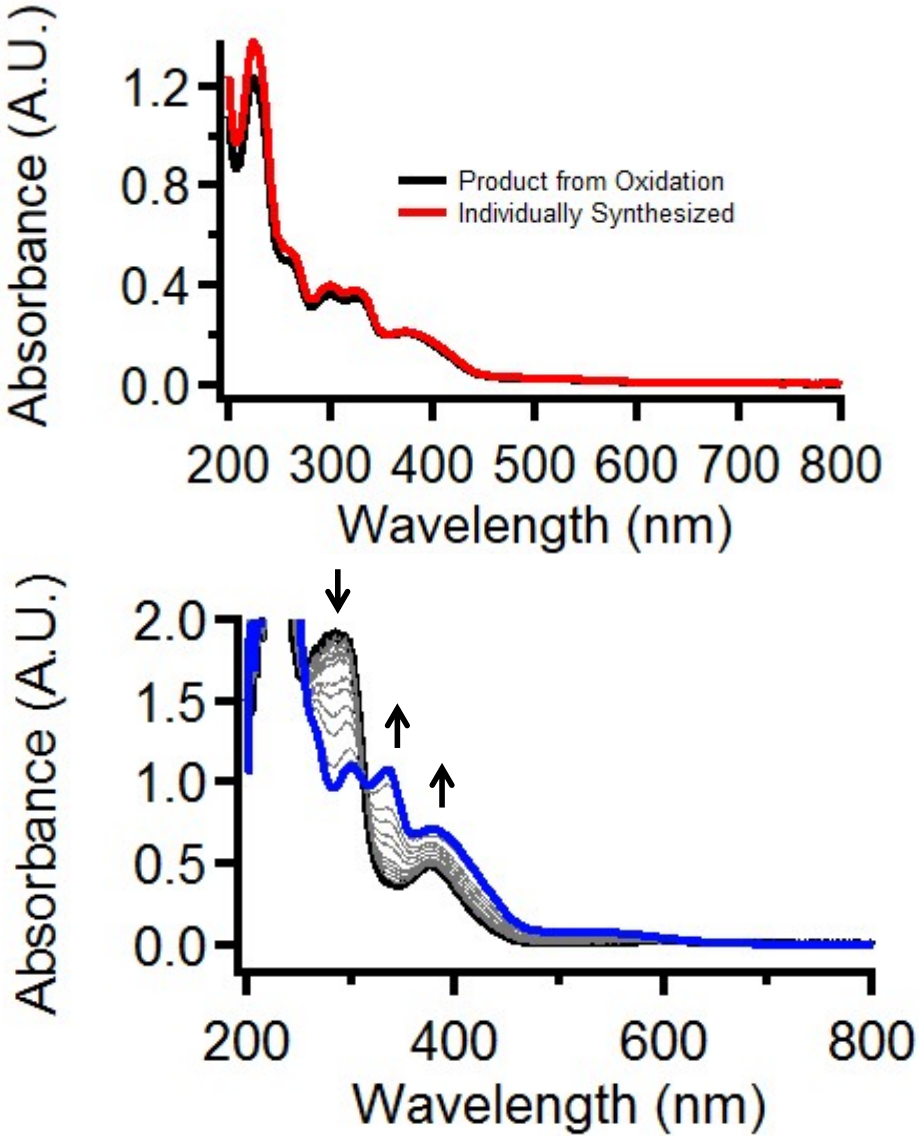


**Figure 3.11:** Top: UV-vis spectra of **2K** as product from oxidation (black trace) and as individually synthesized product (red trace). Bottom: UV-vis spectra of **1K** with addition of $NO^+$ in $CH_3CN$ solution demonstrating the conversion to $Mn^{III}$ (**2K**) following reductive N–N coupling.

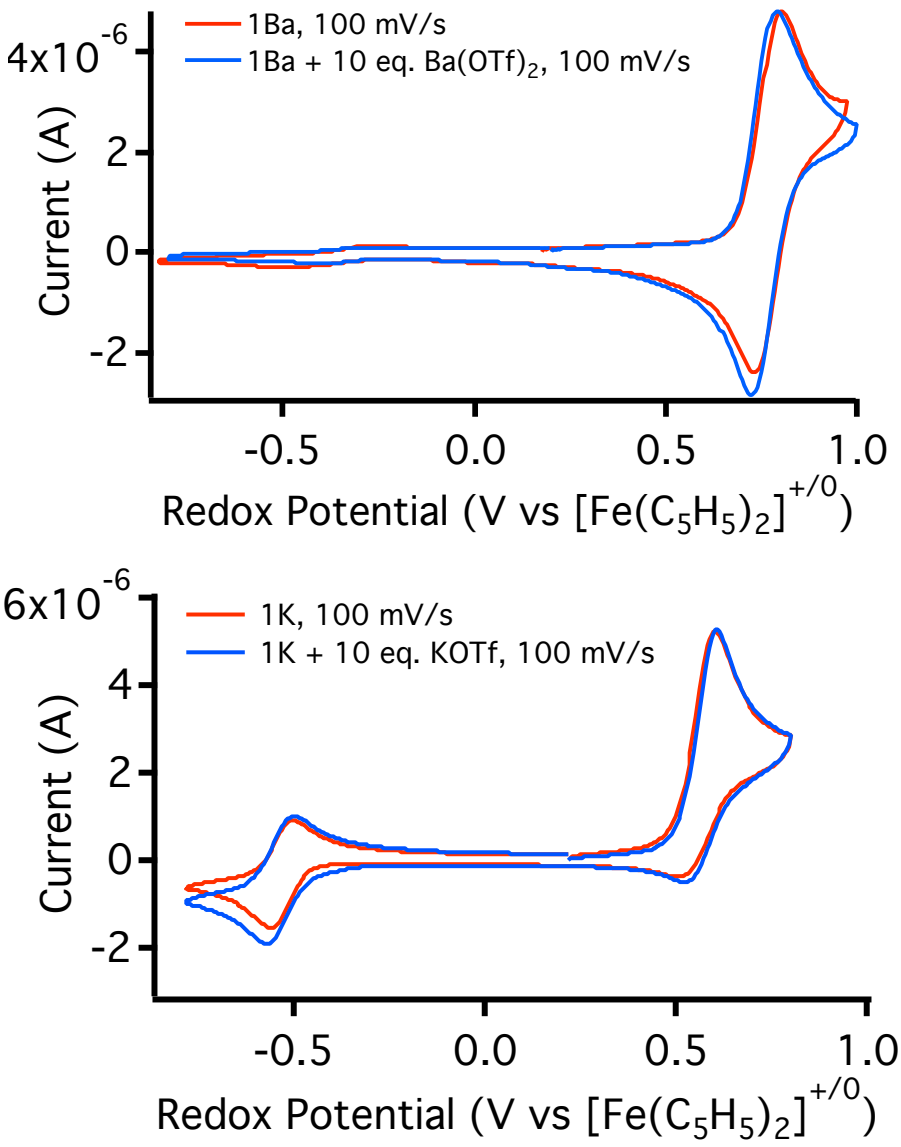


**Figure 3.12:** Cyclic voltammetry titrations of **1Ba** (top) and **1K** (bottom) with excess triflate salts.

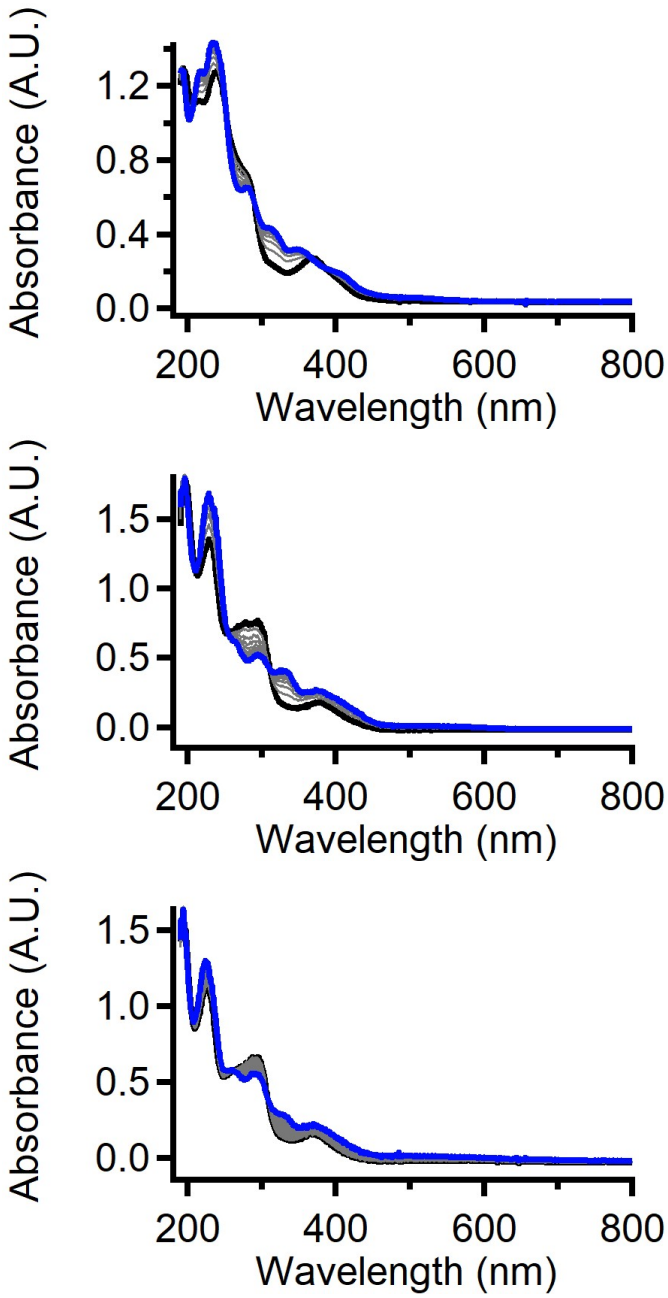


**Figure 3.13:** Electronic absorbance spectra from electrochemical oxidation in UV-visible spectroelectrochemical cell of **A** (top), **1K** (middle), and **1Ba** (bottom), each line represents a time point 10 s apart. (Black spectrum at t = 0 and blue spectrum at the end point).

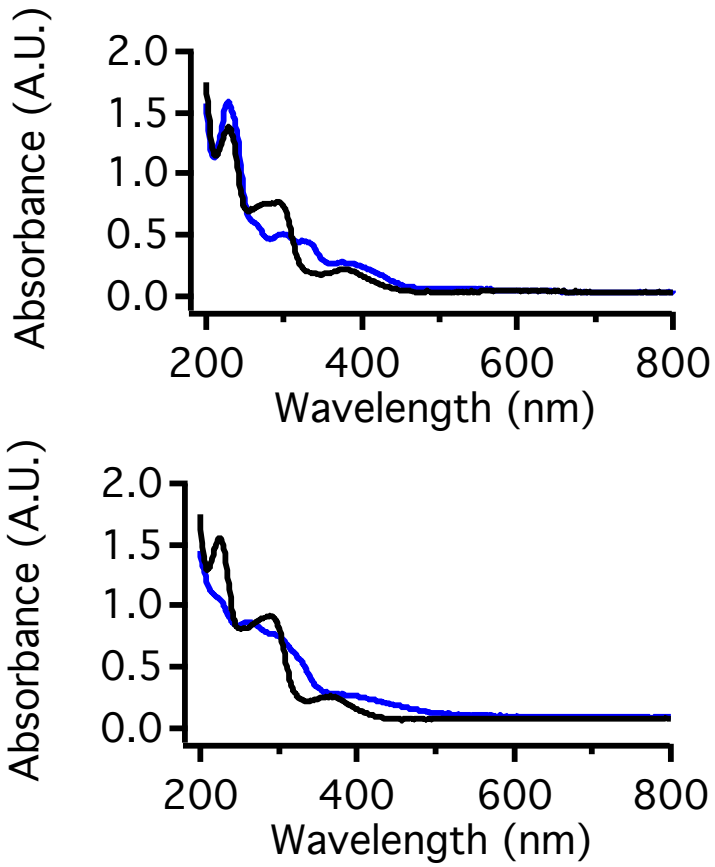


**Figure 3.14:** Electronic absorbance spectra before (black) and after (blue) electrochemical oxidation in UV-visible spectroelectrochemical cell of **1Na** (top), and **1Sr** (bottom).

### 3.3.4 Attempted C–H Bond Activation with 1Ba

The stabilization of the $Mn^{VI}N$ intermediate during oxidative N-N coupling provides an opportunity to exploit this reactive metal nitride species for useful transformations. Dihydroanthracene was chosen as a substrate as it readily undergoes C-H bond activation due to the low bond dissociation free energy of its benzylic C-H bonds (79 kcal/mol[81]). Initial cyclic voltammograms demonstrated an increase in current upon adding one equivalent dihydroanthracene (DHA) to an electrolyte solution of acetonitrile solution and **1Ba**, which increased upon the addition of further equivalents (Figure 3.15). Subsequently, a bulk electrolysis

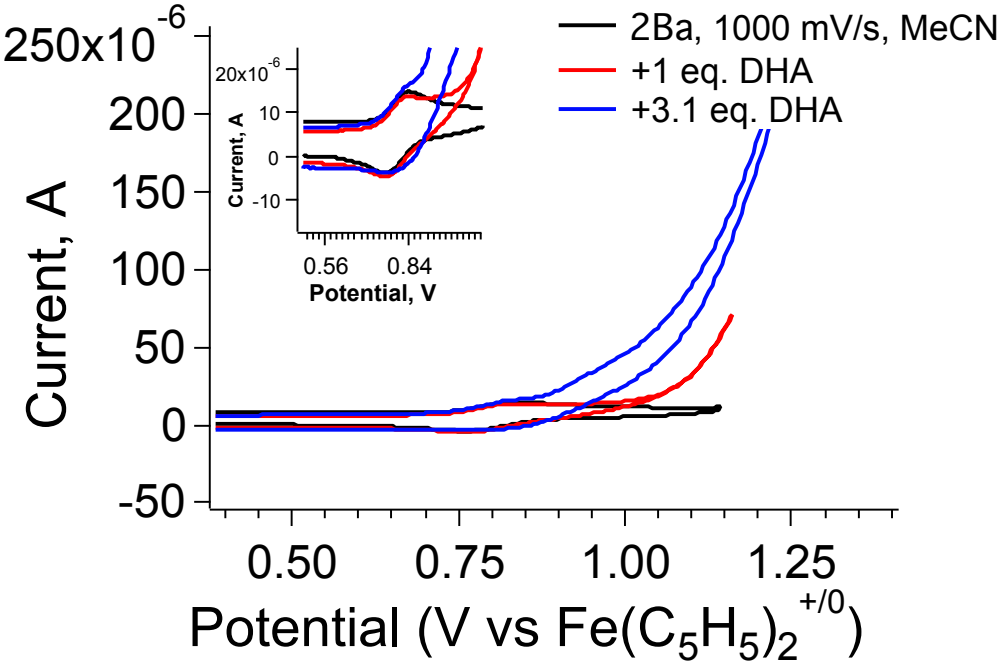


**Figure 3.15:** Cyclic voltammograms demonstrating catalytic current increase associated with the addition of dihydroanthracene (DHA) to **1Ba** in acetonitrile. Inset figure shows an expanded view of the $Mn^{V}$ redox couple.

(BE) experiment was conducted to attempt to identify any products formed during the reaction. The experiment was conducted in $CD_3CN$ so that $^1H$ NMR spectrscopy could be used to identify the products of the reaction. After the experiment, the post-BE solution was passed through a silica gel column with 10:2.5 Hex:EtAc in order to remove the large excess of electrolyte that would interfere with NMR analysis. The $^1H$ NMR spectrum of the post-BE solution revealed a large excess of residual DHA, along with small amounts of anthracene, with no other detectable products (Figure 3.16). GC/MS analysis of the post-BE solution also failed to identify any other products of the reaction. A similar bulk electrolysis experiment was also conducted using the isotopically labelled Mn($^{15}$N)Ba complex to identify any nitrogen containing products (Figure 3.17). The initial spectrum shows a peak at 244.77 ppm corresponding to the $Mn^V(^{15}N)$ species. Upon addition of DHA, a second peak is observed at 379.40 ppm, which ultimately diminishes over time. This species has been assigned as an $Mn^V$(NH) species based on a similar signal observed during protonation studies, discussed in Section 3.3.5. A likely mechanism for this reaction is shown in Scheme 3.1, involving a hydrogen atom transfer from DHA to the activated nitride ligand of the oxidized $Mn^{VI}N$ complex. The resulting $Mn^V$(NH) species is known to be extremely acidic, since the $Mn^V$(N)Ba complex

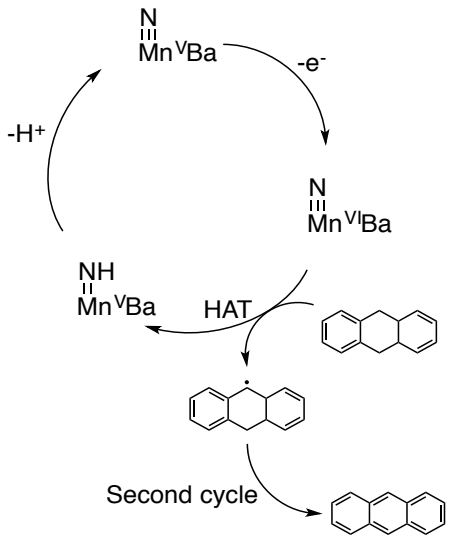


**Scheme 3.1**: Possible mechanism for anthracene formation from DHA catalyzed by **2Ba**.

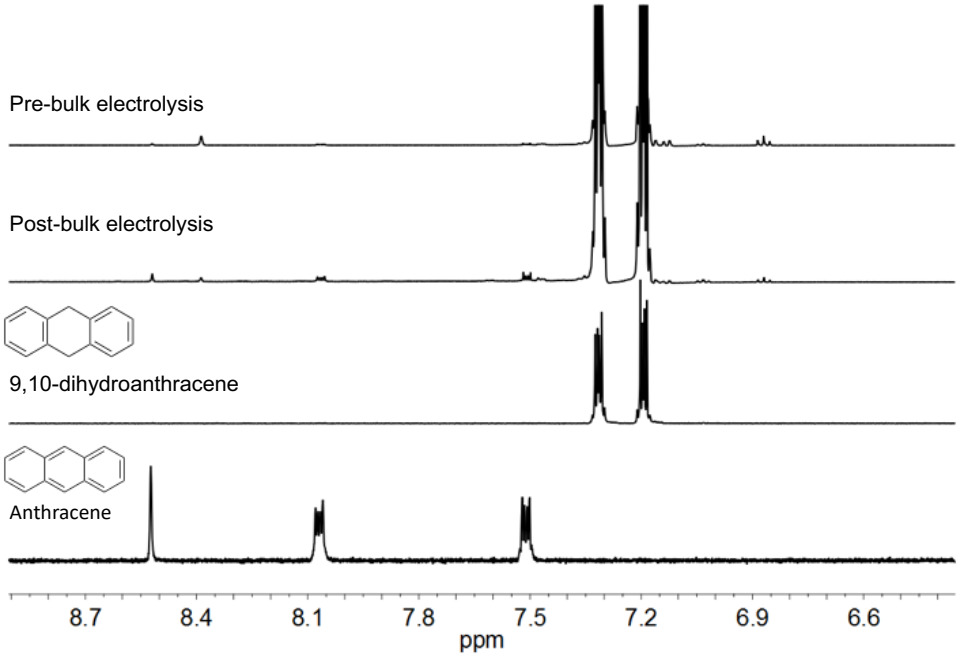


**Figure 3.16:** $^{1}$H NMR spectra of bulk electrolysis solutions before and after oxidation in $CD_3CN$, with dihydroanthracene and anthracene shown for reference.

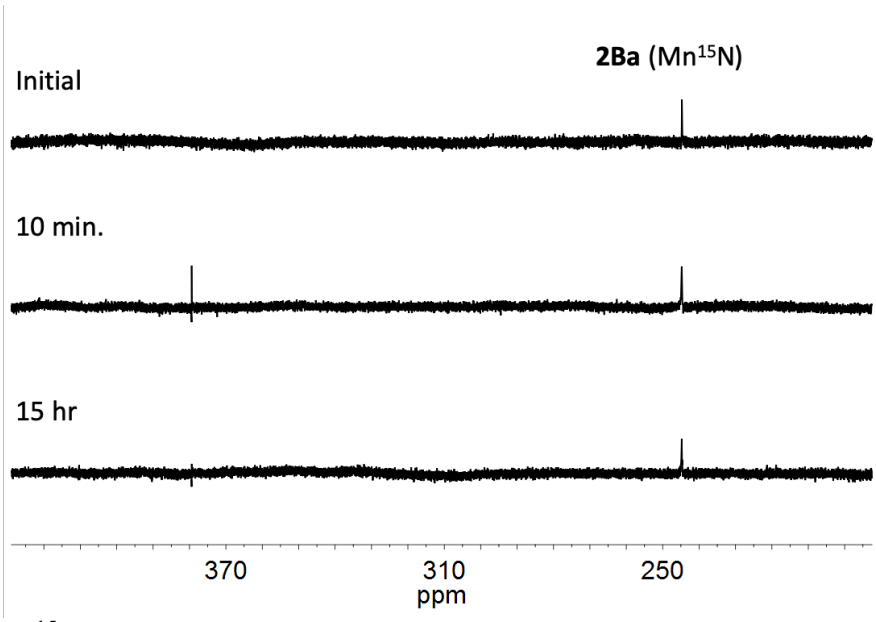


**Figure 3.17:** $^{15}$N NMR spectra before and after bulk oxidation of isotopically labelled **2Ba** in the presence of DHA.

could not be protonated with triflic acid in previous experiments. The acidic proton is then likely removed, regenerating the $Mn^{V}N$ starting material.

### 3.3.5 MnN Protonation Studies

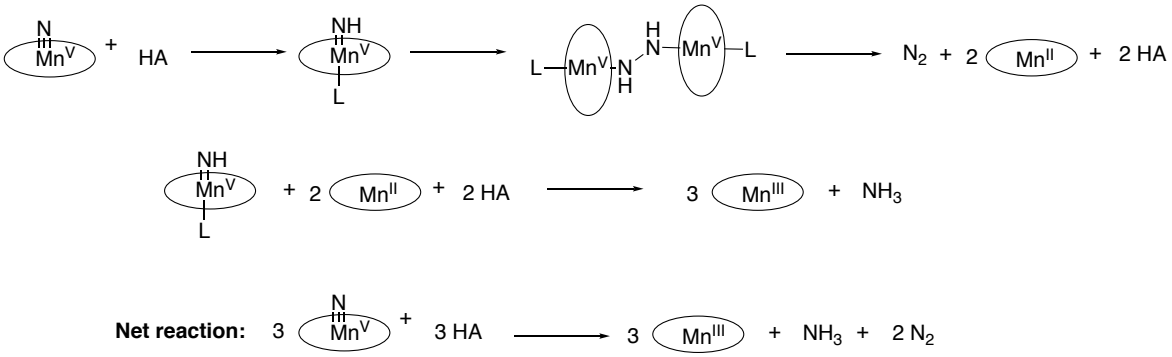


**Scheme 3.2:** Proposed mechanism for decomposition following the protonation of MnN Schiff base complexes based on ref. 82.

The protonation of the MnN complexes was explored to better understand the effects of electrostatic interactions on the p$K_a$ of metal-bound substrates. The acid-base chemistry of metal nitrides has an important role in the reduction of dinitrogen, or alternatively, the oxidation of ammonia. Both of these reactions are relevant to chemical fuel synthesis/utilization, and are further motivation for exploring this chemistry. Upon protonation, MnN Schiff base compounds are known to be unstable and decompose through a bimolecular pathway[82] (Scheme 3.2). Based on the existing findings from the N–N coupling studies, additional cationic charge resulting from the encapsulated metal ion should inhibit bimolecular interactions, and the withdrawal of electron

density should increase the acidity of the manganese nitride. Stabilization of the $Mn^{V}N$ species would be beneficial for utilizing this species for useful reactivity such aziridination[54, 57, 73]

A survey of acid sources showed that anilinium salts were sufficiently strong to protonate **1K** and Mn(N)salen-OMe.[83] However, no reaction was observed with triflic acid and **1Ba** in acetonitrile. Attempts to protonate **1B** have so far been unsuccessful (Scheme 3.3). $^{1}H$ NMR was used to measure the extent of protonation by exploiting the slow timescale of nuclear magnetic resonance spectroscopy to measure the equilibrium between the anilinium salt and its conjugate base. The chemical shifts of the aromatic protons in the acid/conjugate base pair can be used to determine the mole fraction of both compounds in equilibrium.[84-85] Attempts to determine p$K_a$ values using this method were unsuccessful due to a slow decomposition of the manganese nitrene to $Mn^{III}$(scheme 3.1). $^{15}N$ NMR experiments were carried out to determine whether a protonated

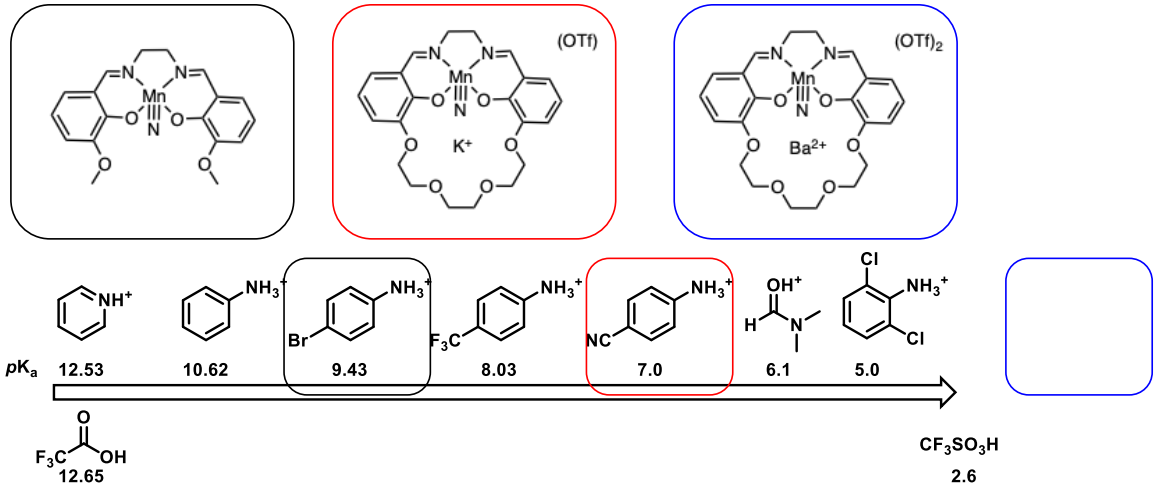


**Scheme 3.3:** Acid sources used for the protonation of MnN(salen-OMe), **1K**, and **1Ba** (ref. 83).

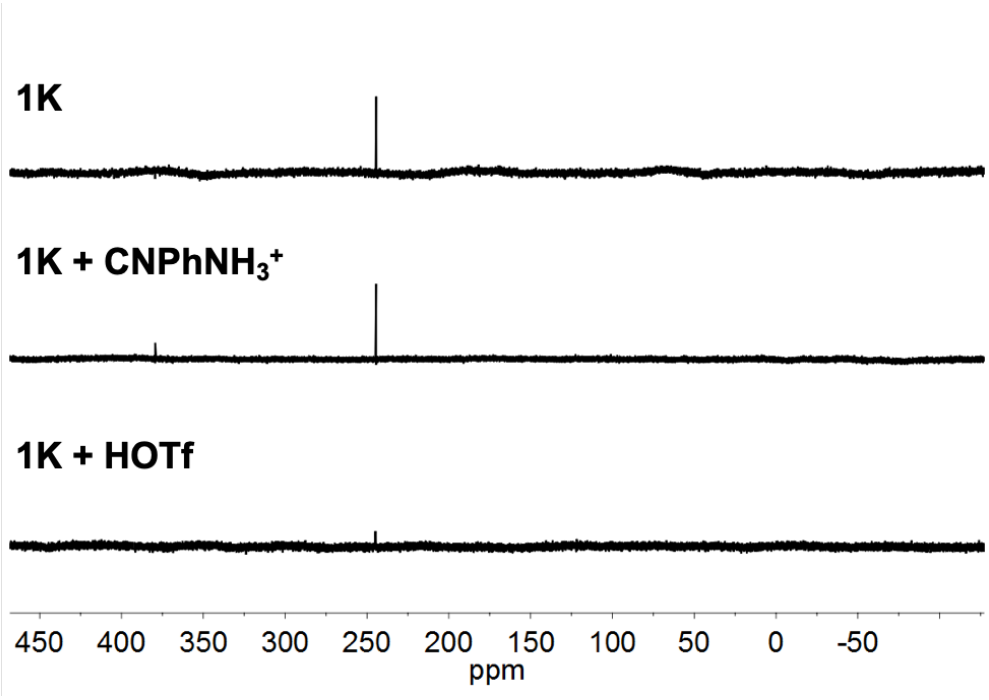


**Figure 3.18:** $^{15}$N NMR spectrum of **1K** (top) with added equivalents of 4-cyanoanilinium (middle) and triflic acid (bottom).

species could be detected spectroscopically. Upon addition of 4-cyanoanilinium to $^{15}$N-labelled **1K**, a new peak is observed at 379.47 ppm (Figure 3.18). This peak is similar to that observed during the C–H bond activation studies with **1Ba** (Figure 3.17).

### 3.3.6 Attempted Electrocatalytic Ammonia Oxidation

Previous studies involving the oxidative N-N coupling reaction of $Mn^{VI}$(N)salen complexes indicate the potential for a closed catalytic cycle for ammonia oxidation. The aforementioned N-N bond forming step to form dinitrogen and $Mn^{III}$(salen) is the last step in an ammonia oxidation mechanism, while the synthesis of the initial Mn(N) complexes involves the oxidation of $Mn^{III}$(salen) in the presence of $NH_4OH$ (see experimental section) using sodium hypochlorite as the oxidant. An electrochemical cycle for the oxidation of ammonia with

$Mn^{III}$(salen) can be conceived if the $Mn^{V}N$ can be generated electrochemically using $NH_4OH$ or $NH_3$ and a proton acceptor. Reactivity studies with $Mn^{III}$(salen) and $NH_3$ under various conditions are herein described.

**MnCl(salen) reactivity with ammonium hydroxide, DMF:** Initial studies investigated the reactivity of $Mn^{III}$Cl(salen) with ammonium hydroxide in dimethylformamide by cyclic voltammetry. DMF was first chosen as a solvent for these studies because it was used with the Mn(N) experiments carried out in previous work. A 0.5 M $NH_4OH$ (aq) stock solution was used for the cyclic voltammetry experiments (Figure 3.20). Upon the addition of either 1 or 11 equivalents of $NH_4OH$, a large anodic current enhancement was observed with an onset of 0.25 V versus the ferrocene/ferrocenium redox couple. Unfortunately, $NH_4OH$ reduction at the glassy carbon electrode takes place at a nearly identical potential, complicating efforts to investigate these reaction conditions further. However, the current increase for the $NH_4OH$ oxidation is larger in the presence of $Mn^{III}$Cl(salen), which could be a sign that catalysis is taking place.

**MnCl(salen) reactivity with $NH_3$ + Base**

The use of aqueous ammonia solutions as a substrate source created issues with water oxidation, so $NH_3$ in THF (400 mM) was used instead. This modification to the reaction conditions also allows for selection of exogenous bases that may avoid the background oxidation observed with $NH_4OH$. A wide survey of bases was conducted, including various hydroxides, carbonates, acetates, and amines, but unfortunately there was not a suitable candidate for $NH_3$ oxidation studies that was both soluble and oxidatively stable at the required potential for catalysis to take place.

**$Mn^{III}$(salen)(OTf) reactivity with $NH_3$ only**

The triflate salt of $Mn^{III}$(salen) was synthesized in order to determine if anion coordination was interfering with ammonia binding. Cyclic voltammetry studies of this complex in the presence of a large excess of ammonia (60 mM $NH_3$: 1 mM Mn) show new anodic features and increased potentials that do not correspond to direct oxidation of ammonia (Figure 3.21). It is possible that this is indicative of catalysis, but future experiments are required to conclusively determine this using isotopically labelled $NH_3$ and analyzing the product headspace for $^{15}N_2$. While this result is exciting, the potentials required for this possible reactivity are considerable and optimization would need to take place for meaningful catalysis to be enabled.

**Mn(salen)(OTf) reactivity with $NH_3$ in $H_2O$**

The triflate salt of the MnCl(salen) complex is fairly soluble in water, enabling reactivity studies under aqueous conditions. In unbuffered solutions, using excess KOH, catalytic water oxidation occurred readily, masking any other redox activity at oxidizing potentials. Using buffered solutions of pH 7.0 and 9.4, similar issues were observed as shown in the red traces in Figure 3.20. Upon the addition of ammonia to the $Mn^{III}$(salen)(OTf) solution, there appears to be a very slight increase in current that could be indicative of reactivity. Unfortunately, the background anodic reactions occurring at these potentials not only make the targeted reactivity ambiguous, but also make selective catalysis impractical. In order for aqueous ammonia oxidation to be viable for study with manganese salen systems, the reactivity would have to be shifted to significantly more negative potentials.

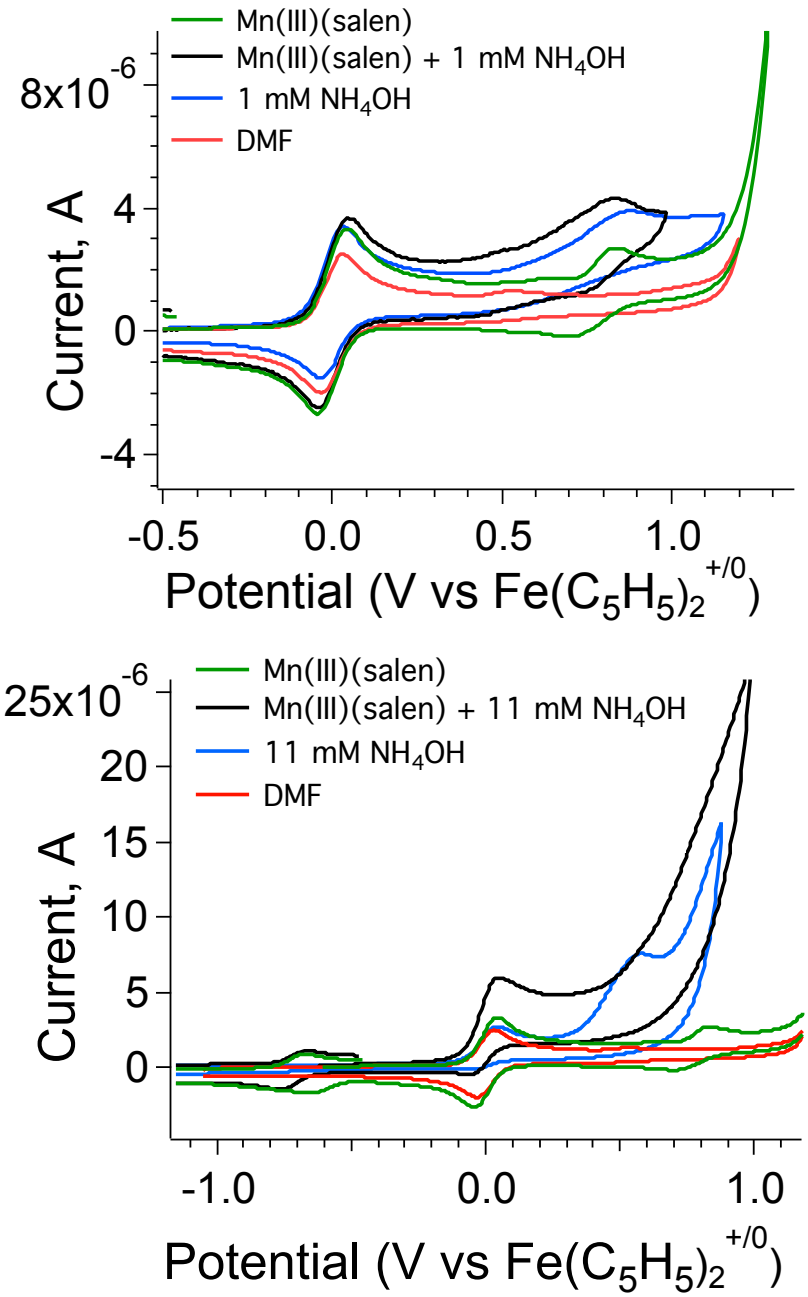


**Figure 3.19:** Cyclic voltammograms of $Mn^{III}Cl$(salen) with 1 eq. (left) and 11 eq. (right) of $NH_4OH$ added as a 0.5 M stock solution in water. All scans take place in dimethylformamide at a scan rate of 100 mV/s.

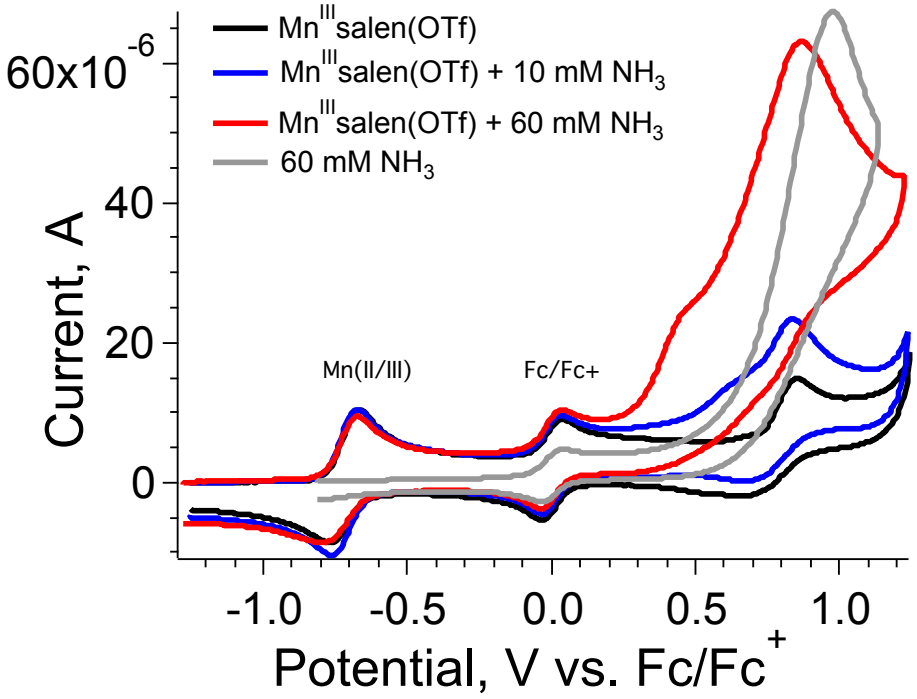


**Figure 3.20:** Cyclic voltammograms of $Mn^{III}$(salen) in the presence of excess ammonia in dimethylformamide. All cyclic voltammograms were taken at a scan rate of 1000 mV/s, with ammonia being titrated from a 400 mM solution of tetrahydrofuran.

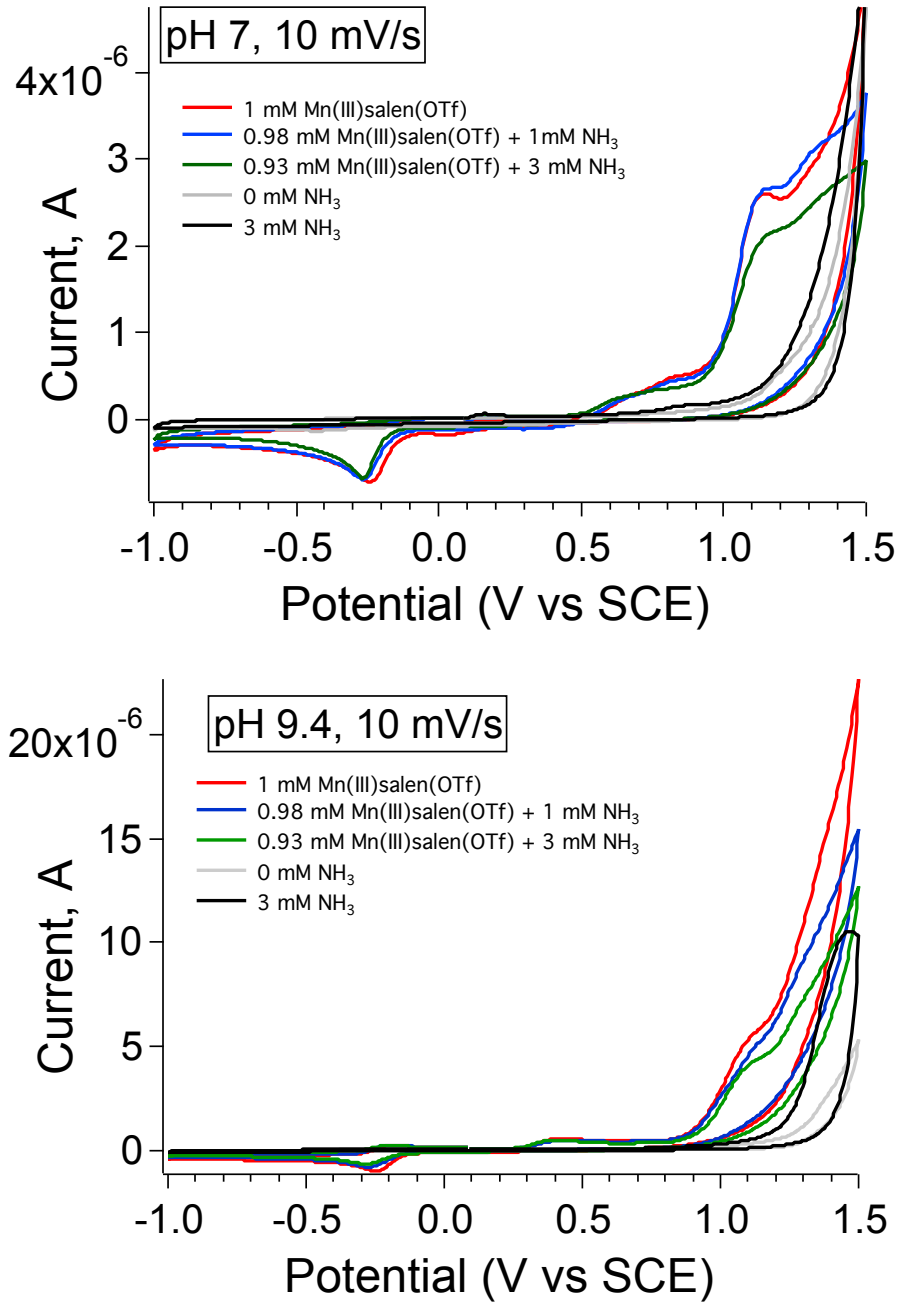


**Figure 3.21:** Cyclic Voltammograms from $Mn^{III}$(salen)(OTf) reactivity studies with ammonia in aqueous phosphate buffer solutions with additional 200 mM KCl as a supporting electrolyte.

### 3.4 Conclusions

In prior studies with neutral MnN salen complexes, addition of electron-withdrawing ligand substituents leads to more oxidizing $Mn^{VI}N$ complexes which predictably leads to higher rates of coupling to form $N_2$. We find that incorporation of cationic charges leads to the opposite trend. As the charge increases, the oxidation potential shifts positive but the rate of bimolecular coupling decreases by an order of magnitude per charge, leading to an inverse linear free energy relationship (Figure 4).

The difference in the rate of bimolecular coupling between **1K** and **1Ba** is not likely due to steric effects. $K^+$ and $Ba^{2+}$ have similar ionic radii of 138 and 135 pm,[86] respectively, so the steric profile of **1K** and **1Ba** are similar. We note the vibrational stretching frequency of Mn≡N is consistent with a mild increase in bond strength for **1M** versus **A** (Table 3.1), which may contribute to the observed decrease in rate. The slightly higher vibrational frequencies observed in **1M** may reflect a vibrational Stark effect from the electric field potential generated from the cation, which was observed in the prior Co analogues of this ligand.[76] However, the differences in bond force constant were calculated to be quite small (Table 3.2). Therefore, we believe the major contribution to the rate differences is through electrostatic repulsion that increases with increasing charge.

The effect of charge on $N_2$ coupling was previously explored in Ir nitride complexes, but the charge differences were due to oxidation of the complex so that cationic effects could not be isolated from changes in electronic structure.[25] In this ligand framework, we can modify the charge without changing the oxidation state of the metal or primary coordination sphere. As a result, incorporation of a mono- or dication presents an effective route to overriding the electronic effects

observed using inductive ligand modifications. The result is metal nitrides that are both more oxidizing *and* more stable to bimolecular quenching, properties that could not be accessed through the use of inductive ligand modifications.

Steric interactions are commonly used to mitigate undesirable bimolecular reaction pathways but may also negatively affect substrate reactivity. In contrast, adjusting charge has the potential to inhibit bimolecular reactivity without affecting interactions with neutral substrates.[87] For example, a series of monometallic iron salen complexes were known to catalyze the aerobic oxidation of allylic C-H bonds. Total catalyst turnover number was limited by formation of inactive Fe-O-Fe complexes.[88-90] In our prior study of Fe analogues of **1K** and **1Ba**, we found that increasing cationic charge led to progressively slower rates of bimolecular aerobic deactivation and higher overall turnover numbers.[80] Another potential application exists to improve many olefin metathesis catalysts, where bimolecular reactivity is a major decomposition pathway.[72, 87, 91-92]

The incorporation of cationic charge presents an alternative strategy for constructing reactive complexes or catalysts that may otherwise deactivate through bimolecular coupling. It is demonstrated herein that non-redox active cations can be utilized in transition metal complexes to both modulate the redox potential *and* reactivity.

C-H bond activation was not observed with **2Ba** and dihydroanthracene upon electrochemical oxidation of the $Mn^{v}(N)$ species, with only anthracene observed in the product mixture following controlled potential electrolysis. The mechanism of this catalysis likely involves H-atom transfer to the $Mn^{VI}(N)$ species followed by deprotonation to regenerate $Mn^{V}(N)$ (Scheme

3.1). Future studies could be carried out with the less acidic **1K**, which would likely persist longer as the $Mn^{V}$(NH) species and could result in a change in observed reactivity.

Protonation of **1K** led to a decomposition to **2K** (Figure 3.1), likely through the same pathway observed in similar Mn(N) Schiff base compounds.[82] Attempts to calculate the p$K_a$ of this species were thwarted by subsequent reactivity of the manganese nitrene protonation product. Although discrete values could not be obtained since decomposition prevented equilibration, chemical reactivity studies indicate acidity increases with the cationic charge of **M** to the extent that **1Ba** cannot be protonated using proton sources as strong as triflic acid.

Catalytic ammonia oxidation with **A** (Figure 3.1) was pursued based on the observed N–N coupling and synthetic procedures for synthesizing the $Mn^{V}$ nitride complexes (see 3.5: Experimental Details), which revealed a potential electrocatalytic cycle.. Electrochemical experiments did not show conclusive evidence of ammonia oxidation. However, the redox potentials required to reach the $Mn^{IV/III}$ couple were too close to the substrate oxidation window at the glassy carbon electrode, so interpretation of any faradaic processes associated with Mn are difficult. Regardless, the fact that catalysis, if any, is occurring concomitantly with direct ammonia oxidation at the electrode surface is indicative of a very poor performing electrocatalyst. In order to be studied further in this context, the $Mn^{IV/III}$ redox potential must be shifted to significantly lower values.

## 3.5 Experimental Details

### General Considerations

All reagents were purchased from commercial suppliers and used without further purification. Unless otherwise noted, all organic chemical manipulations were performed under ambient conditions. Compounds were purified via flash column chromatography using Sorbent Technologies 60 Å, 230–400 mesh silica gel. Unless otherwise noted, inorganic metal complexations were performed in a Vacuum Atmospheres Co. dry box under a nitrogen atmosphere. Anhydrous solvents were sparged with UHP argon (Praxair) and passed through columns containing Q-5 and molecular sieves before use. $^{1}$H and $^{13}$C{$^{1}$H} NMR and spectra were recorded at 500 MHz and 600 MHz on Bruker instruments.

$^{1}$H NMR spectra chemical shifts are reported as δ values in ppm relative to residual protio solvent: $CDCl_3$ (7.26 ppm), $CD_3CN$ (1.94 ppm). Proton NMR data are reported as follows: chemical shift (δ ppm), multiplicity (s = singlet, d = doublet, t = triplet, q = quartet), coupling constants (J) in Hertz (Hz), and integration. Multiplets (m) are reported over the range (ppm). Electrospray ionization mass spectra (ESI-MS) were obtained on a Micromass LCT and collected at the University of California-Irvine Mass Spectrometry Facility. Elemental analyses were performed on a Perkin Elmer 2400 Series II CHNS elemental analyzer. Ultraviolet-visible (UV–vis) spectra were collected in a 10 mm or 1 mm pathlength pathlength quartz cuvette, using an Agilent Technologies Cary 60 UV–vis spectrometer and 8453 Diode-array UV-vis spectrometer equipped with Unisoku Unispeks cryostat. X-band (9.28 GHz) EPR spectra were collected as

frozen solutions using a Bruker EMX spectrometer equipped with an ER041XG microwave bridge.

Electrochemical experiments were performed under an atmosphere of nitrogen in a solution containing 0.2 M $(nBu)_4NPF_6$ in acetonitrile. Glassy carbon was used as the working and auxiliary electrode and a silver wire was used as a pseudoreference electrode. Ferrocene was used as an internal standard, and all potentials are referenced to the ferrocenium/ferrocene couple. Cyclic voltammetry experiments were performed with a Pine Wavedriver 10 or 20 potentiostat and Pine Aftermath software version 1.2.7359.

UV-visible spectroelectrochemistry experiments were conducted in a commercially available UV-vis spectroelectrochemistry kit from Pine Instrument with Pt working/counter electrode and Ag wire as a pseudo reference electrode. Ferrocene was used as an internal standard.

X-ray diffraction studies were carried out at the UCI Department of Chemistry X-ray Crystallography Facility on a Bruker SMART APEX II diffractometer. Data were collected at 100 K using Mo Kα radiation (λ = 0.71073 Å). A full sphere of data was collected for each crystal structure. The APEX2[1] program suite was used to determine unit-cell parameters and to collect data. The raw frame data were processed and absorption corrected using the SAINT[1] and SADABS[2] programs, respectively, to yield the reflection data files. Structures were solved by direct methods using SHELXS and refined against $F^2$ on all data by full-matrix least-squares with SHELXTL.[3] All non-hydrogen atoms were refined anisotropically. Non-aquo hydrogen atoms were placed at geometrically calculated positions and refined using a riding model, and their isotropic displacement parameters were fixed at 1.2 (1.5 for methyl groups) times the Ueq of the

atoms to which they are bonded. Aquo ligand's hydrogen atoms were located in the difference map, and their positions and displacement parameters were refined freely.

**Physical Methods**

**Synthesis of 1M (M = $Na^+$, $Sr^{2+}$)**

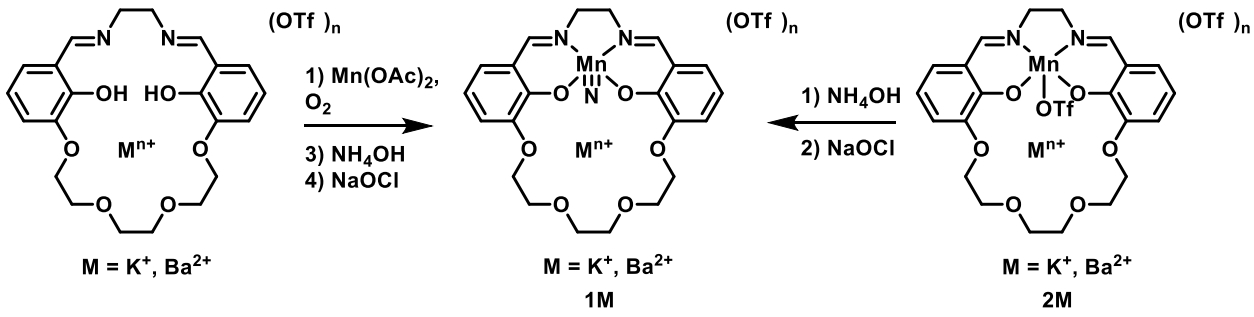


**Method 1:** Under an inert atmosphere, the ligand with $Na^+$ or $Sr^{2+}$ (0.05 mmol, 1 equiv) and $Mn(OAc)_2 \cdot 4H_2O$ (13 mg, 0.05 mmol, 1 equiv) was dissolved in 1 mL EtOH before being heated at 50°C for 1 hour. After cooling down to ambient temperature, solvent was removed *in vacuo* and the orange solid was re-dissolved in 1 mL $CH_3CN$. A concentrated $CH_3CN$ solution of AgOTf (13 mg, 0.05 mmol, 1 equiv) was added and the solution immediately turned brown with precipitate. After stirring for 1 hour, a white solid was separated by filtration and the filtrate was collected and concentrated. The solid was then dissolved in methanol at room temperature before aqueous $NH_4OH$ (6 M, 0.2 mL, 1.2 mmol, 24 equiv) was added to the solution dropwise. The brown solution turned into brown suspension. While stirring vigorously, Clorox® bleach solution (approximately 0.7 M, 0.2 mL, 0.15 mmol, 3 equiv) was added dropwise which turned the mixture green. The solution was stirred for another 15 minutes before extraction with $CH_2Cl_2$ (3x15 mL). The combined organic layer was dried using anhydrous $MgSO_4$, and solvent was removed *in*

*vacuo*. At this point, 1.0 equiv of corresponding $M(OTf)_n$ salt was added to concentrated $CH_3CN$ solution and recrystallized by $Et_2O$ diffusion into $CH_3CN$ solution. Excess $M(OTf)_n$ salt was washed by cold dimethoxyethane (DME) and then the solid was recrystallized again to yield the purified **1M**.

**1Na:** Yield 17 mg (44%), ESI-MS *m/z* calcd $C_{22}H_{24}FMnNaN_3O_6$ 504.1 ($M^+$-$CF_3SO_3$), found 504.0, Calcd $C_{23}H_{26}F_3NaMnN_3O_9S$ (653.04 g·mol$^{-1}$): C, 42.28; H, 3.70; N, 6.43. Found: C, 42.19; H, 3.74; N, 6.46. UV-vis absorption, $\lambda_{max}$, nm (ε, $M^{-1}cm^{-1}$) 227 (46,800), 285 (27,300), 376(6,900), 596 (184). IR (Mn—N) 1052 $cm^{-1}$. $^1H$ NMR (600 MHz, $CD_3CN$) δ 8.32 (s, 2H), 7.04 (ddd, *J* = 14.39, 7.93, 1.42 Hz, 4H), 6.75 (t, *J* = 7.88 Hz, 2H), 4.11 (m, 4H), 4.03 – 3.96 (m, 2H), 3.94-3.91 (m, 2H) 3.83-3.68 (m, 6H). $^{13}C$ NMR (125 MHz, $CD_3CN$) δ 167.70, 156.10, 149.01, 125.71, 119.81, 117.32, 116.42, 115.52, 69.24, 67.76, 66.84, 60.95.

**1Sr**: Yield 26 mg (42.6%), ESI-MS *m/z* calcd $C_{23}H_{24}SrF_3MnN_3O_9S$ 718.0 ($M^+$), Found: 717.6 Calcd $C_{24}H_{24}SrF_6MnN_3O_{12}S_2$ (866.92 g·mol$^{-1}$): C, 33.24; H, 2.79; N, 4.85. Found: C, 33.08; H, 2.81; N, 4.85. UV-vis absorption, $\lambda_{max}$, nm (ε, $M^{-1}cm^{-1}$) 224 (42,200) 290 (23,900), 365 (5,600), 596 (260). IR (Mn—N) 1058 $cm^{-1}$. $^1H$ NMR (600 MHz, $CD_3CN$) δ 8.39 (s, 2H), 7.17 (ddd, *J* = 31.7, 8.0, 1.4 Hz, 4H), 6.89 (t, *J* = 8.0 Hz, 2H), 4.33-4.27 (m, 4H), 4.16 (m, 2H), 4.08 (td, *J* = 10.0, 2.7 Hz, 2H), 3.99 – 3.91 (m, 4H), 3.88 – 3.84 (m, 2H), 3.82 -3.76 (m, 2H), $^{13}C$ NMR (125 MHz, $CD_3CN$) δ 167.80, 159.79, 147.94, 126.75, 119.97, 117.93, 117.32, 116.38, 70.04, 68.47, 66.99, 60.96.

**Variable Scan Rate Cyclic Voltammetry Experiment**

Cyclic voltammetry of 0.2 mM of **1M** or **2M** solutions were measured from 10 mV/s to 10,000 mV/s. Non-faradaic currents were measured and plotted with square root of scan rate, yielding a straight line, indicating a diffusion-limited process.

**UV-vis spectroelectrochemistry experiments**

0.3 mL of 200 μM Mn complex in 0.2 M $TBAPF_6$ MeCN solution was placed into a Pine UV-visible spectroelectrochemistry setup. The solution was electrolyzed at 200 mV from the anodic peak while single wavelength measurements were used to monitor the reaction progress. Before and after each electrolysis, a UV-vis spectrum was performed before and cyclic voltammogram was measured.

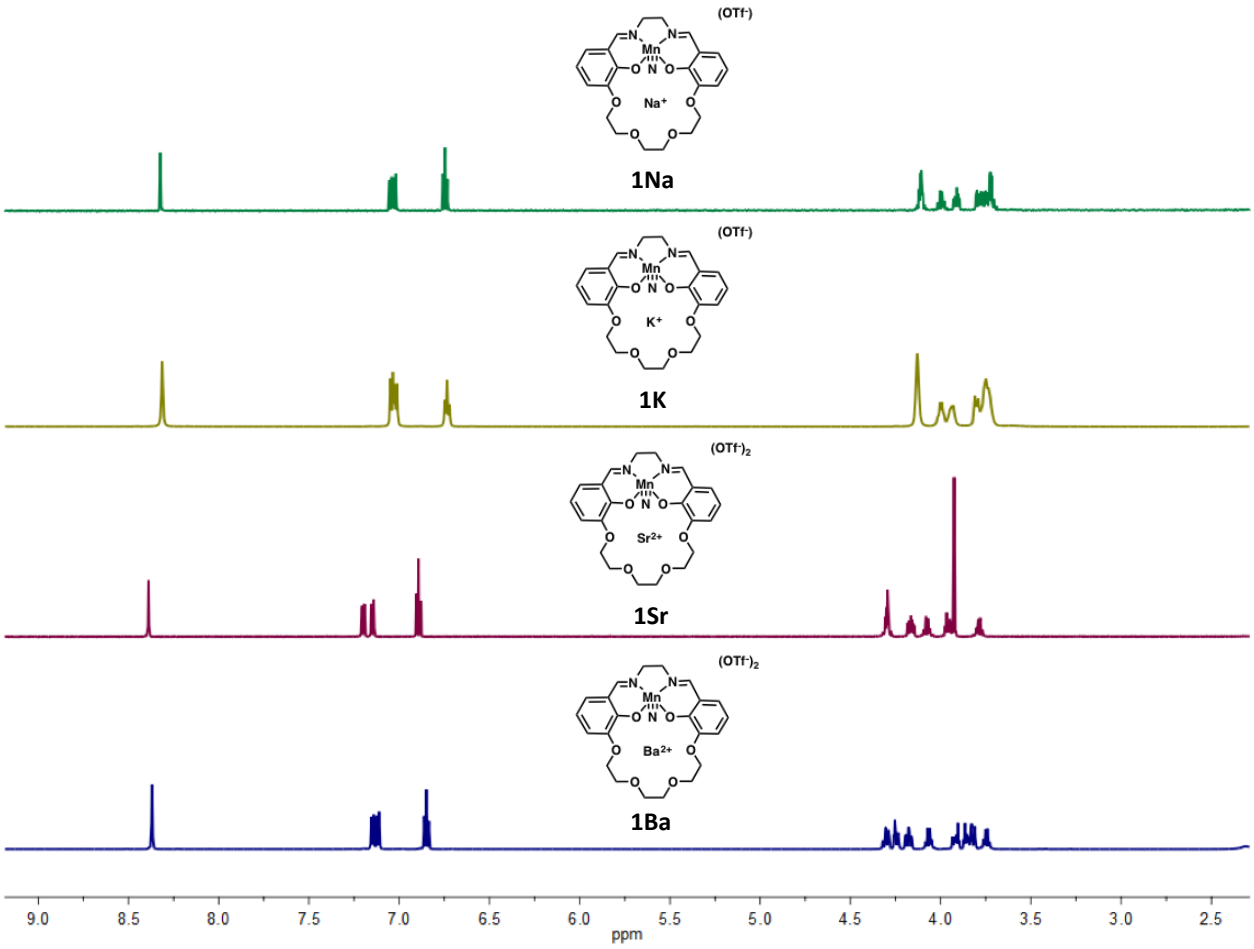


**Figure 3.22:** $^{1}$H NMR spectra of **1Na**, **1K**, **1Sr** and **1Ba** in $CD_3CN$.

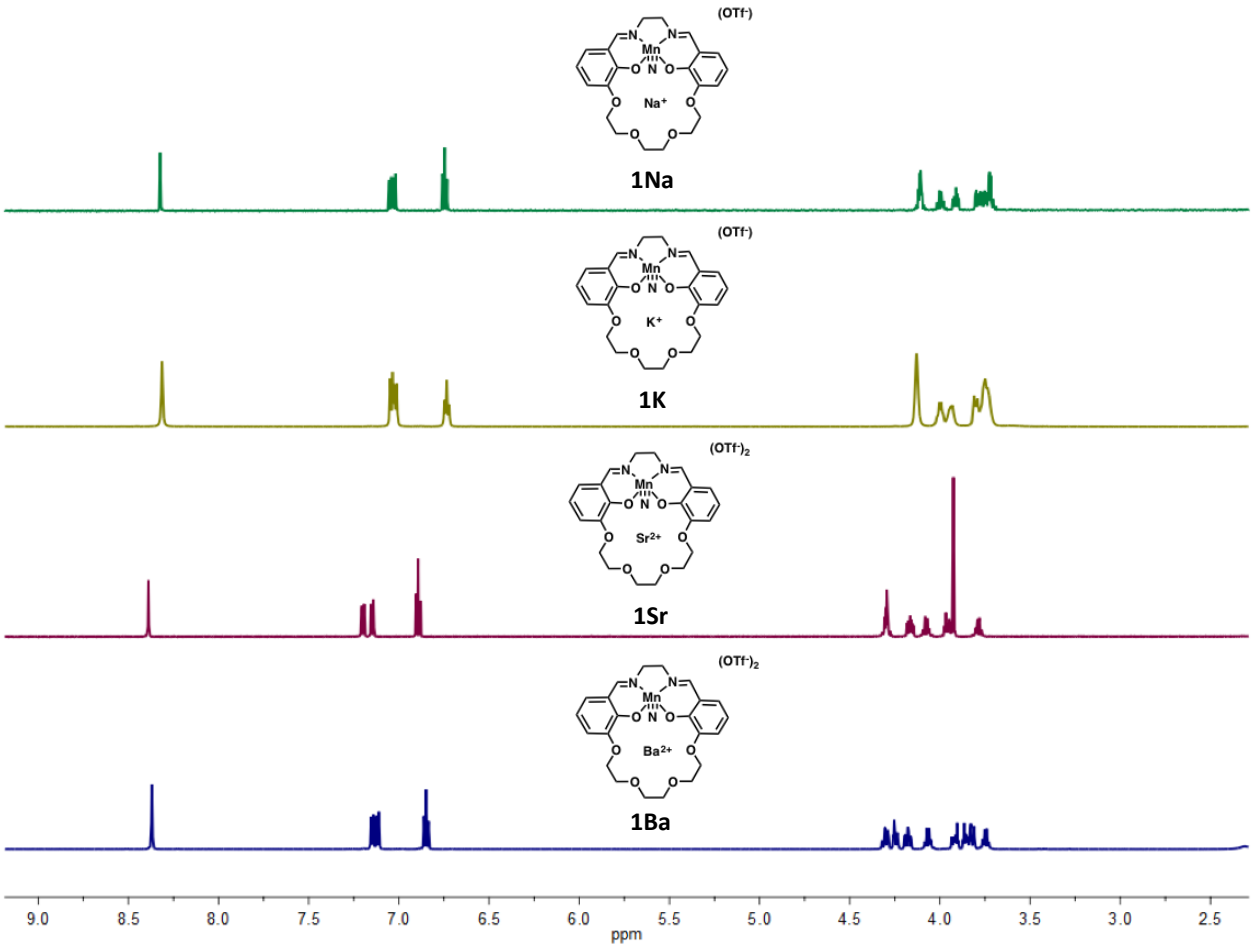


**Figure 3.23:** $^{1}$H NMR spectra of **1Na**, **1K**, **1Sr** and **1Ba** in $CD_3CN$.

**Table 3.2:** Table of different Mn-nitrido derivatives with force constant (k) calculated from $Mn^{V}\equiv N$ stretch measured by IR spectroscopy, and bond lengths obtained from solid-state structures.

| Entry | Name | Derivatives | Mn≡N stretch ($cm^{-1}$) | k (N/m) | Bond Length (Å) | Reference |
|---|---|---|---|---|---|---|
| 1 | **A** | 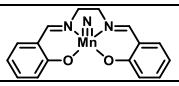 | 1047 | 720.70 | 1.512 | 52 |
| 2 | | 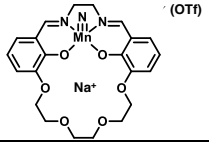 | 1052 | 726.80 | -- | This work |
| 3 | **1K** | 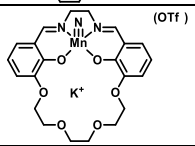 | 1050 | 724.19 | 1.528 | This work |
| 4 | | 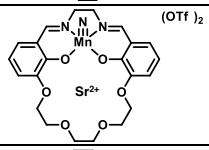 | 1058 | 735.12 | -- | This work |
| 5 | **1Ba** | 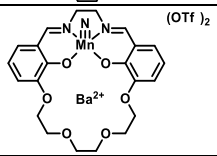 | 1055 | 731.73 | 1.529 | This work |
| 6 | – | 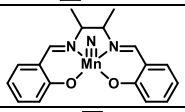 | 1047 | 720.70 | 1.51 | 52 |
| 7 | **B** | 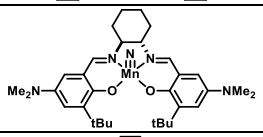 | 1045 | 717.94 | 1.514 | 1 |
| 8 | **C** | 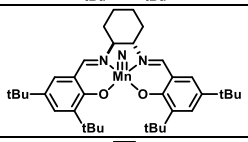 | 1043 | 715.20 | 1.526 | 1 |
| 9 | **D** | 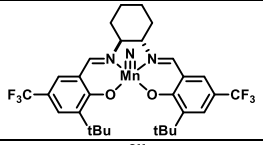 | 1042 | 713.83 | 1.526 | 1 |
| 8 | – | 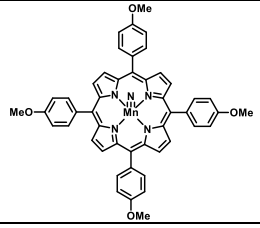 | 1036 | 705.63 | 1.515 | 68 |

**Table 3.3:** Tabulated data for $i_a/i_c$ ratio and peak-to-peak separations ($E_a-E_c$) at scan rate from 25-10,000 mV/s. At 100 mV/s under our conditions, the internal ferrocene used as a standard typically has an $E_a$-$E_c$ between 65-75 mV.

| Scan rate (mV/s) | **1**: $Mn^{V/VI}$ couple | | **1K**: $Mn^{V/VI}$ couple | | **1Ba**: $Mn^{V/VI}$ couple | |
|---|---|---|---|---|---|---|
| | $i_c/i_a$ | $E_a$-$E_c$ (V) | $i_c/i_a$ | $E_a$-$E_c$ (V) | $i_c/i_a$ | $E_a$-$E_c$ (V) |
| 25 | 0.5706 | 0.1234 | 0.5227 | 0.1346 | 1.0655 | 0.1020 |
| 50 | 0.4518 | 0.1087 | 0.4688 | 0.1298 | 0.9877 | 0.1120 |
| 100 | 0.4332 | 0.1190 | 0.4771 | 0.1248 | 0.9001 | 0.1170 |
| 250 | 0.4347 | 0.1035 | 0.5153 | 0.1497 | 1.0265 | 0.1270 |
| 500 | 0.5591 | 0.1186 | 0.5826 | 0.1548 | 1.0587 | 0.1780 |
| 1000 | 0.6674 | 0.1149 | 0.6558 | 0.1734 | 1.0897 | 0.2050 |
| 2500 | 0.7323 | 0.1541 | 0.7220 | 0.2025 | 1.0544 | 0.2310 |
| 5000 | 0.8764 | 0.1923 | 0.8188 | 0.2240 | 0.9579 | 0.4080 |
| 10000 | 0.8807 | 0.3045 | 0.7772 | 0.3093 | 1.0347 | 0.4190 |

**Table 3.4:** Tabulated data for $i_a/i_c$ ratio and peak-to-peak separations ($E_a-E_c$) at scan rate from 20-5,000 mV/s. At 100 mV/s under our conditions, the internal ferrocene used as a standard typically has an $E_a$-$E_c$ between 65-75 mV.

| Scan rate (mV/s) | **1Na**: $Mn^{V/VI}$ couple | | **1Sr**: $Mn^{V/VI}$ couple | |
|---|---|---|---|---|
| | $i_c/i_a$ | $E_a$-$E_c$ (V) | $i_c/i_a$ | $E_a$-$E_c$ (V) |
| 20 | 0.6362545 | 0.0894 | 0.66322478 | 0.0606 |
| 50 | 0.4079602 | 0.0949 | 0.72960639 | 0.0758 |
| 100 | 0.3758074 | 0.0945 | 0.90993072 | 0.0759 |
| 250 | 0.42258652 | 0.1039 | 0.94091269 | 0.08 |
| 500 | 0.59475167 | 0.0954 | 0.9667171 | 0.0958 |
| 1000 | 0.55752212 | 0.112 | 1.05165705 | 0.12 |
| 5000 | 0.72490066 | 0.1424 | 1.10918953 | 0.1576 |

### 3.6 References


1. Clarke, R. M.; Storr, T., *J. Am. Chem. Soc.* **2016,** *138* (47), 15299-15302.

2. Keener, M.; Peterson, M.; Hernández Sánchez, R.; Oswald, V. F.; Wu, G.; Ménard, G., *Chem. Eur. J.* **2017,** *23* (48), 11479-11484.

3. Smith, J. M., Reactive Transition Metal Nitride Complexes. In *Progress in Inorganic Chemistry Volume 58*, Karlin, K. D., Ed. 2014.

4. Eikey, R. A.; Abu-Omar, M. M., *Coord. Chem. Rev.* **2003,** *243* (1), 83-124.

5. Berry, J. F., *Comments Inorg. Chem.* **2009,** *30* (1-2), 28-66.

6. Mehn, M. P.; Peters, J. C., *J. Inorg. Biochem.* **2006,** *100* (4), 634-643.

7. Yandulov, D. V.; Schrock, R. R., *Science* **2003,** *301* (5629), 76-78.

8. Arashiba, K.; Kinoshita, E.; Kuriyama, S.; Eizawa, A.; Nakajima, K.; Tanaka, H.; Yoshizawa, K.; Nishibayashi, Y., *J. Am. Chem. Soc.* **2015,** *137* (17), 5666-5669.

9. Curley, J. J.; Sceats, E. L.; Cummins, C. C., *J. Am. Chem. Soc.* **2006,** *128* (43), 14036-14037.

10. Gdula, R. L.; Johnson, M. J. A., *J. Am. Chem. Soc.* **2006,** *128* (30), 9614-9615.

11. Chisholm, M. H.; Delbridge, E. E.; Kidwell, A. R.; Quinlan, K. B., *Chem. Commun.* **2003,** (1), 126-127.

12. Ertl, G., Elementary Steps in Ammonia Synthesis. In *Catalytic Ammonia Synthesis: Fundamentals and Practice*, Jennings, J. R., Ed. Springer US: Boston, MA, 1991; pp 109-132.

13. Meyer, T. J.; Huynh, M. H. V., *Inorg. Chem.* **2003,** *42* (25), 8140-8160.

14. Laplaza, C. E.; Johnson, M. J. A.; Peters, J. C.; Odom, A. L.; Kim, E.; Cummins, C. C.; George, G. N.; Pickering, I. J., *J. Am. Chem. Soc.* **1996,** *118* (36), 8623-8638.

15. Muñoz, S. B.; Lee, W. T.; Dickie, D. A.; Scepaniak, J. J.; Subedi, D.; Pink, M.; Johnson, M. D.; Smith, J. M., *Angew. Chem. Int. Ed.* **2015,** *54* (36), 10600-10603.

16. Scepaniak, J. J.; Bontchev, R. P.; Johnson, D. L.; Smith, J. M., *Angew. Chem. Int. Ed.* **2011,** *50* (29), 6630-6633.

17. Scepaniak, J. J.; Young, J. A.; Bontchev, R. P.; Smith, J. M., *Angew. Chem. Int. Ed.* **2009,** *48* (17), 3158-3160.

18. Lee, W.-T.; Juarez, R. A.; Scepaniak, J. J.; Muñoz, S. B.; Dickie, D. A.; Wang, H.; Smith, J. M., *Inorg. Chem.* **2014,** *53* (16), 8425-8430.

19. Brown, S. N., *J. Am. Chem. Soc.* **1999,** *121* (41), 9752-9753.

20. Maestri, A. G.; Cherry, K. S.; Toboni, J. J.; Brown, S. N., *J. Am. Chem. Soc.* **2001,** *123* (30), 7459-7460.

21. Crevier, T. J.; Lovell, S.; Mayer, J. M.; Rheingold, A. L.; Guzei, I. A., *J. Am. Chem. Soc.* **1998,** *120* (26), 6607-6608.

22. Crevier, T. J.; Mayer, J. M., *J. Am. Chem. Soc.* **1998,** *120* (22), 5595-5596.

23. Wai-Lun, M.; Y., L. W. W.; Hoi-Ki, K.; Shek-Man, Y.; Tai-Chu, L., *Angew. Chem. Int. Ed.* **2012,** *51* (36), 9101-9104.

24. Abbenseth, J.; Bete, S. C.; Finger, M.; Volkmann, C.; Würtele, C.; Schneider, S., *Organometallics* **2018,** *37* (5), 802-811.

25. Abbenseth, J.; Finger, M.; Wurtele, C.; Kasanmascheff, M.; Schneider, S., *Inorg. Chem. Front.* **2016,** *3* (4), 469-477.

26. Klopsch, I.; Kinauer, M.; Finger, M.; Würtele, C.; Schneider, S., *Angew. Chem. Int. Ed.* **2016,** *55* (15), 4786-4789.

27. Klopsch, I.; Finger, M.; Würtele, C.; Milde, B.; Werz, D. B.; Schneider, S., *J. Am. Chem. Soc.* **2014,** *136* (19), 6881-6883.

28. Klopsch, I.; Yuzik-Klimova, E. Y.; Schneider, S., Functionalization of N2 by Mid to Late Transition Metals via N–N Bond Cleavage. In *Nitrogen Fixation*, Nishibayashi, Y., Ed. Springer International Publishing: Cham, 2017; pp 71-112.

29. Schendzielorz, F. S.; Finger, M.; Volkmann, C.; Würtele, C.; Schneider, S., *Angew. Chem. Int. Ed.* **2016,** *55* (38), 11417-11420.

30. Scheibel, M. G.; Wu, Y.; Stückl, A. C.; Krause, L.; Carl, E.; Stalke, D.; de Bruin, B.; Schneider, S., *J. Am. Chem. Soc.* **2013,** *135* (47), 17719-17722.

31. Julia, S.; Yu., R. A.; Serena, D. G.; Peter, B., *Angew. Chem. Int. Ed.* **2009,** *48* (26), 4734-4738.

32. Vreeken, V.; Siegler, M. A.; de Bruin, B.; Reek, J. N. H.; Lutz, M.; van der Vlugt, J. I., *Angew. Chem. Int. Ed.* **2015,** *54* (24), 7055-7059.

33. Thompson, R.; Tran, B. L.; Ghosh, S.; Chen, C.-H.; Pink, M.; Gao, X.; Carroll, P. J.; Baik, M.-H.; Mindiola, D. J., *Inorg. Chem.* **2015,** *54* (6), 3068-3077.

34. Groves, J. T.; Takahashi, T., *J. Am. Chem. Soc.* **1983,** *105* (7), 2073-2074.

35. Bottomley, L. A.; Neely, F. L., *J. Am. Chem. Soc.* **1988,** *110* (20), 6748-6752.

36. Margulieux, G. W.; Bezdek, M. J.; Turner, Z. R.; Chirik, P. J., *J. Am. Chem. Soc.* **2017,** *139* (17), 6110-6113.

37. Semproni, S. P.; Chirik, P. J., *Angew. Chem. Int. Ed.* **2013,** *52* (49), 12965-12969.

38. Bendix, J.; Meyer, K.; Weyhermüller, T.; Bill, E.; Metzler-Nolte, N.; Wieghardt, K., *Inorg. Chem.* **1998,** *37* (8), 1767-1775.

39. Carola, V.; W., H. F.; Jörg, S.; Christian, A.; Karsten, M., *Angew. Chem. Int. Ed.* **2008,** *120* (14), 2721-2724.

40. Meyer, K.; Bendix, J.; Metzler-Nolte, N.; Weyhermüller, T.; Wieghardt, K., *J. Am. Chem. Soc.* **1998,** *120* (29), 7260-7270.

41. Meyer, K.; Bill, E.; Mienert, B.; Weyhermüller, T.; Wieghardt, K., *J. Am. Chem. Soc.* **1999,** *121* (20), 4859-4876.

42. Scepaniak, J. J.; Vogel, C. S.; Khusniyarov, M. M.; Heinemann, F. W.; Meyer, K.; Smith, J. M., *Science* **2011,** *331* (6020), 1049-1052.

43. Zolnhofer, E. M.; Käß, M.; Khusniyarov, M. M.; Heinemann, F. W.; Maron, L.; van Gastel, M.; Bill, E.; Meyer, K., *J. Am. Chem. Soc.* **2014,** *136* (42), 15072-15078.

44. Berry, J. F.; Bill, E.; Bothe, E.; George, S. D.; Mienert, B.; Neese, F.; Wieghardt, K., *Science* **2006,** *312* (5782), 1937-1941.

45. Núria, A. A.; Serena, D. G.; Bernd, M.; Eckhard, B.; Karl, W.; Frank, N., *Angew. Chem. Int. Ed.* **2005,** *44* (19), 2908-2912.

46. Curley, J. J.; Cook, T. R.; Reece, S. Y.; Müller, P.; Cummins, C. C., *J. Am. Chem. Soc.* **2008,** *130* (29), 9394-9405.

47. Betley, T. A.; Peters, J. C., *J. Am. Chem. Soc.* **2004,** *126* (20), 6252-6254.

48. Rohde, J.-U.; Betley, T. A.; Jackson, T. A.; Saouma, C. T.; Peters, J. C.; Que, L., *Inorg. Chem.* **2007,** *46* (14), 5720-5726.

49. Scheibel, M. G.; Askevold, B.; Heinemann, F. W.; Reijerse, E. J.; de Bruin, B.; Schneider, S., *Nat. Chem.* **2012,** *4*, 552.

50. Man, W.-L.; Lam, W. W. Y.; Yiu, S.-M.; Lau, T.-C.; Peng, S.-M., *J. Am. Chem. Soc.* **2004,** *126* (47), 15336-15337.

51. Xie, J.; Man, W.-L.; Wong, C.-Y.; Chang, X.; Che, C.-M.; Lau, T.-C., *J. Am. Chem. Soc.* **2016,** *138* (18), 5817-5820.

52. Du Bois, J.; Tomooka, C. S.; Hong, J.; Carreira, E. M., *Acc. Chem. Res.* **1997,** *30* (9), 364-372.

53. Minakata, S.; Ando, T.; Nishimura, M.; Ryu, I.; Komatsu, M., *Angew. Chem. Int. Ed.* **1999,** *37* (24), 3392-3394.

54. Nishimura, M.; Minakata, S.; Thongchant, S.; Ryu, I.; Komatsu, M., *Tetrahedron Lett.* **2000,** *41* (36), 7089-7092.

55. Svenstrup, N.; Bogevig, A.; G. Hazell, R.; Anker Jorgensen, K., *J. Chem. Soc., Perkin Trans. 1* **1999,** (11), 1559-1566.

56. Carreira, E. M.; Hong, J.; Du Bois, J.; Tomooka, C. S., *Pure Appl. Chem.* **1998,** *70* (5), 1097-1103.

57. Ho, C. M.; Lau, T. C.; Kwong, H. L.; Wong, W. T., *J. Chem. Soc., Dalton Trans.* **1999,** (15), 2411-2413.

58. Du Bois, J.; Tomooka, C. S.; Hong, J.; Carreira, E. M., *J. Am. Chem. Soc.* **1997,** *119* (13), 3179-3180.

59. Bois, J. D.; Tomooka Craig, S.; Hong, J.; Carreira Erick, M.; Day Michael, W., *Angew. Chem. Int. Ed.* **2003,** *36* (15), 1645-1647.

60. Du Bois, J.; Hong, J.; Carreira, E. M.; Day, M. W., *J. Am. Chem. Soc.* **1996,** *118* (4), 915-916.

61. Ley, S. V.; Dixon, D. J., *Chemtracts* **1999,** *12* (1), 27-33.

62. Chang, C. J.; Connick, W. B.; Low, D. W.; Day, M. W.; Gray, H. B., *Inorg. Chem.* **1998,** *37* (12), 3107-3110.

63. Sejr Jepsen, A.; Roberson, M.; G. Hazell, R., *Chem. Commun.* **1998,** (15), 1599-1600.

64. Golubkov, G.; Gross, Z., *J. Am. Chem. Soc.* **2005,** *127* (10), 3258-3259.

65. Hedegaard, E. D.; Schau-Magnussen, M.; Bendix, J., *Inorg. Chem. Commun.* **2011,** *14* (5), 719-721.

66. Bendix, J., *J. Am. Chem. Soc.* **2003,** *125* (44), 13348-13349.

67. Birk, T.; Bendix, J., *Inorg. Chem.* **2003,** *42* (23), 7608-7615.

68. Hill, C. L.; Hollander, F. J., *J. Am. Chem. Soc.* **1982,** *104* (25), 7318-7319.

69. Man, W.-L.; Tang, T.-M.; Wong, T.-W.; Lau, T.-C.; Peng, S.-M.; Wong, W.-T., *J. Am. Chem. Soc.* **2004,** *126* (2), 478-479.

70. Man, W.-L.; Kwong, H.-K.; Lam, W. W. Y.; Xiang, J.; Wong, T.-W.; Lam, W.-H.; Wong, W.-T.; Peng, S.-M.; Lau, T.-C., *Inorg. Chem.* **2008,** *47* (13), 5936-5944.

71. Man, W.-L.; Chen, G.; Yiu, S.-M.; Shek, L.; Wong, W.-Y.; Wong, W.-T.; Lau, T.-C., *Dalton Trans.* **2010,** *39* (46), 11163-11170.

72. Bailey, G. A.; Foscato, M.; Higman, C. S.; Day, C. S.; Jensen, V. R.; Fogg, D. E., *J. Am. Chem. Soc.* **2018,** *140* (22), 6931-6944.

73. Ho, C.-M.; Lau, T.-C.; Kwong, H.-L.; Wong, W.-T., *J. Chem. Soc., Dalton Trans.* **1999,** (15), 2411-2414.

74. Man, W.-L.; Lam, W. W. Y.; Kwong, H.-K.; Yiu, S.-M.; Lau, T.-C., *Angew. Chem. Int. Ed.* **2012,** *51* (36), 9101-9104.

75. Lafaye, K.; Bosset, C.; Nicolas, L.; Guérinot, A.; Cossy, J., *Beilstein J Org Chem* **2015,** *11*, 2223-2241.

76. Reath, A. H.; Ziller, J. W.; Tsay, C.; Ryan, A. J.; Yang, J. Y., *Inorg. Chem.* **2017,** *56* (6), 3713-3718.

77. Van Staveren, C. J.; Van Eerden, J.; Van Veggel, F. C. J. M.; Harkema, S.; Reinhoudt, D. N., *J. Am. Chem. Soc.* **1988,** *110* (15), 4994-5008.

78. Chantarojsiri, T.; Reath, A. H.; Yang, J. Y., *Angew. Chem. Int. Ed.* **2018,** *57* (43), 14037-14042.

79. Connelly, N. G.; Zanello, P., *Inorganic Electrochemistry: Theory, Practice and Application*. Royal Society of Chemistry: 2007.

80. Chantarojsiri, T.; Ziller, J. W.; Yang, J. Y., *Chem. Sci.* **2018,** *9* (9), 2567-2574.

81. Klein, J. E. M. N.; Dereli, B.; Que, L.; Cramer, C. J., *Chem. Commun.* **2016,** *52* (69), 10509-10512.

82. Yiu, S.-M.; Lam, W. W. Y.; Ho, C.-M.; Lau, T.-C., *J. Am. Chem. Soc.* **2007,** *129* (4), 803-809.

83. Kaljurand, I.; Kütt, A.; Sooväli, L.; Rodima, T.; Mäemets, V.; Leito, I.; Koppel, I. A., *J. Org. Chem.* **2005,** *70* (3), 1019-1028.

84. Edidin, R. T.; Sullivan, J. M.; Norton, J. R., *J. Am. Chem. Soc.* **1987,** *109* (13), 3945-3953.

85. Appel, A. M.; Lee, S.-J.; Franz, J. A.; DuBois, D. L.; Rakowski DuBois, M.; Twamley, B., *Organometallics* **2009,** *28* (3), 749-754.

86. Shannon, R., *Acta Crystallogr. A* **1976,** *32* (5), 751-767.

87. Schrodi, Y., Mechanisms of Olefin Metathesis Catalyst Decomposition and Methods of Catalyst Reactivation. In *Handbook of Metathesis*, R. H. Grubbs, A. G. W., D. J. O'Leary and E. Khosravi, Ed. 2015; pp 323-342.

88. Grinstaff, M.; Hill, M.; Labinger, J.; Gray, H., *Science* **1994,** *264* (5163), 1311-1313.

89. Böttcher, A.; Grinstaff, M. W.; Labinger, J. A.; Gray, H. B., *J. Mol. Catal. A: Chem.* **1996,** *113* (1), 191-200.

90. Böttcher, A.; Birnbaum, E. R.; Day, M. W.; Gray, H. B.; Grinstaff, M. W.; Labinger, J. A., *J. Mol. Catal. A: Chem.* **1997,** *117* (1), 229-242.

91. Schrock, R. R.; Copéret, C., *Organometallics* **2017,** *36* (10), 1884-1892.

92. Amoroso, D.; Yap, G. P. A.; Fogg, D. E., *Organometallics* **2002,** *21* (16), 3335-3343.

# APPENDIX A:

# SYNTHETIC EFFORTS TOWARDS THE DEVELOPMENT OF AN ASYMMETRIC HETEROBIMETALLIC LIGAND SCAFFOLD

## A.1. Motivation and Specific Aims

Prior to this effort, two types of salen-derived heterobimetallic scaffolds had previously been examined for applied to $CO_2$ reduction activity in the Yang Lab. The first (Figure A.1a), discussed in the main text of this work, a crown ether-containing salen motif that incorporates redox-inactive group I or II metal, discussed in other applications in the main text of this work. The second (Figure A.1b) is a symmetrical disalen framework that houses two transition metals in close proximity.

## A.2. Background

The NiFe carbon monoxide dehydrogenase (CODH) enzyme carries out the reversible anaerobic oxidation of CO to $CO_2$ in biological systems at -0.52 V vs. SHE, near the thermodynamic potential.[1] Structural characterization of the CODH enzyme revealed the presence of a cubane [$NiFe_4S_4$] active site, with a proximal Fe in close proximity to the catalytic $Ni^{2+}$ center, located only 2.8 Å away.[2] Further investigation of $CO_2$ reactivity led to structural characterization

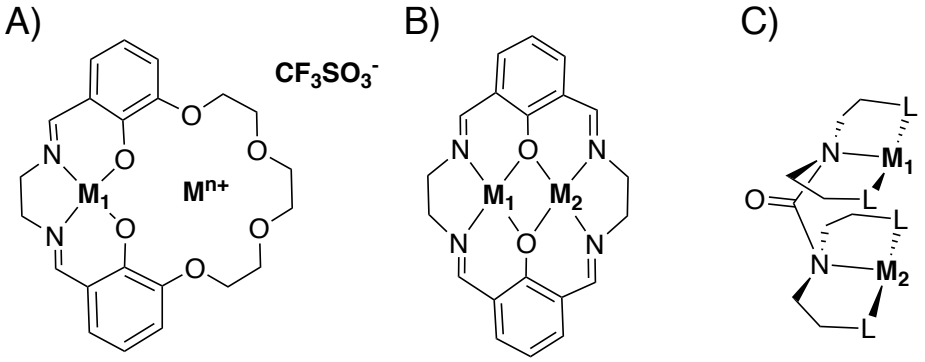


**Figure A.1:** A) Crown salen framework for heterobimetallic complexes containing a transition metal and a Lewis acid cation. B) Disalen framework for heterobimetallic transition metal complexes. C) Bis-pincer complexes described herein.

indicating a cooperative binding interaction between both of these metal sites and $CO_2$.[3] In addition to the close metal-metal distance, other notable structural features are the formation of a seven-membered ring upon $CO_2$ binding and the presence of open coordination sites on both metals.

In designing new ligand frameworks, structural inspiration is taken from the NiFe CODH enzyme. An existing synthetic system that serves as a good starting point is a bimetallic palladium complex by Dubois.[4-5] These complexes are supported by two triphosphine units linked by a methylene bridge. Compared to the monometallic species, the bimetallic complexes displayed a two order of magnitude increase in turnover frequency. Kinetic studies indicated that two palladium atoms and one $CO_2$ molecule were involved in the rate limiting step, demonstrating metal-metal cooperativity. However, very low turnover numbers resulted from irreversible metal-metal bond formation upon reduction to a Pd(I)-Pd(I) species. This bis-pincer ligand motif was the main source of inspiration for the compounds discussed in this report.

**A.3. Discussion**

The ligand design was carried out with several objectives in mind. The ligand framework must house two metal centers with open coordination sites for $CO_2$ coordination. A tridentate pincer-type ligand would be preferable in this sense because it can form square planar $CO_2$ adducts. Additionally, the two metal binding sites would ideally be electronically nonequivalent to infer Lewis acid/base cooperativity. Electronically nonequivalent sites would allow separate reduction potentials for each metal and prevent two-electron reduction and potential metal-metal bond formation. The urea backbone of the ligand framework was utilized to enforce a rigid, seven-

membered chelate upon $CO_2$ coordination as well as for synthetic practicality. Using reported methods for asymmetric urea preparations, the addition of each pincer moiety can be carried out stepwise to develop a scaffold with two different binding sites (See **A1** and **A2** in Scheme A.1). In nearly all of this exploratory synthesis, the diphenylphosphine PNP compound, bis(2-(diphenylphosphaneyl)ethyl)amine (**$PN^HP$-$Ph_2$**, Scheme A.1), was used due to its relative oxidative stability compared to other phosphines. If a feasible synthetic route had been developed, other derivatives would have been employed to reach the desired asymmetric ligands.

**Attempted Synthesis from Bis(4-nitrophenyl)carbonate:** This electron deficient carbonate is known to undergo substitution with secondary amines, forming a urea compound and the loss of two equivalents of nitrophenol[6] (Scheme A.1). One or two equivalents of a **$PN^HP$-$Ph_2$** was added to bis(4-nitrophenyl)carbonate to form the single- or double-substituted compound (**A1** and **A2** in Scheme A.1, respectively). $^{31}P$ NMR analysis of the resulting reaction solution showed several new species, indicating that clean conversion to the desired products did not occur. This route was eventually discarded in favor of the 4-nitrophenylchloroformate strategy described below.

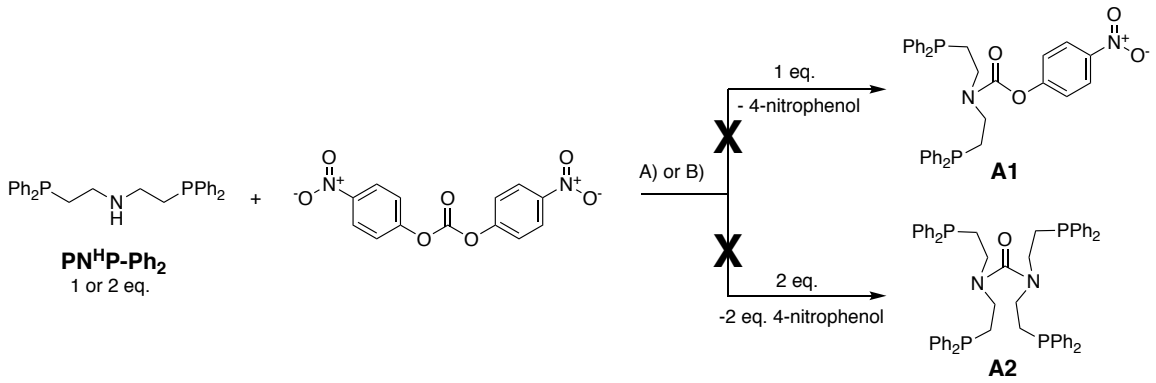


**Scheme A.1:** Proposed synthesis of **A1** and **A2** via bis(4-nitrophenyl)carbonate. A) toluene, 16 hr, B) $CHCl_3$, 16 hr.

**Synthesis of A1 from 4-nitrophenylchloroformate:** This synthesis[6] was a modification of the bis(4-nitrophenyl)carbonate route in which the coupling agent contained a very reactive acid chloride leaving group, and a relatively less reactive nitrophenolate group. The presence of inequivalent leaving groups generated less byproducts from the addition of one equivalent of pincer ligand to form **A1** (Scheme A.2). It was proposed that **A1** could undergo coupling with a second equivalent of a separate SNS or PNP equivalent to form an asymmetric bis-pincer ligand scaffold. Addition of **$PN^HP$-$Ph_2$** to 4-nitrophenylchloroformateunder a dinitrogen atmosphere followed by purification of the reaction mixture by column chromatography yielded **A1**, confirmed by $^{31}P$ NMR and mass spectrometry.

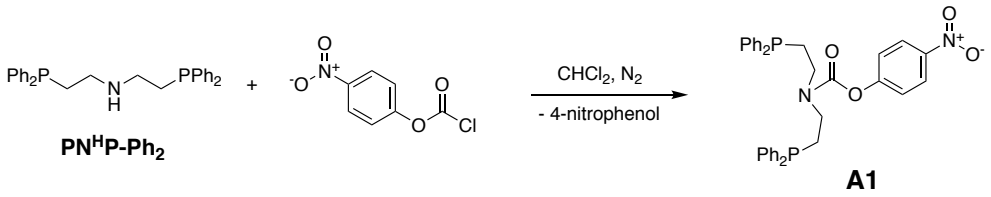


**$PN^HP$-$Ph_2$** **A1**

**Scheme A.2:** Synthesis of A1 with 4-nitrophenylchloroformate.

**Attempted $PN^HP$-$Ph_2$ Coupling with A1:** It was hoped that the isolation of **A1** would enable the synthesis of **A2** and asymmetric analogues via a substitution with a second equivalent of **$PN^HP$-$Ph_2$** or similar pincer compound, and a wide range of strategies were used in this effort (Scheme A.3). Initially, **$PN^HP$-$Ph_2$** was added to **A1** in refluxing $CH_2Cl_2$ and monitored for 24 hours. TLC analysis of the reaction mixture failed to show the formation of product or conversion of starting materials, which was confirmed by $^{31}P$ NMR. In order to increase the nucleophilicity of **$PN^HP$-$Ph_2$**, various bases were employed to deprotonate the secondary amine. The first attempts with triethylamine and potassium carbonate B and C in Scheme A.3) showed no noticeable conversion of starting materials; a stronger base may be required. The next set of reaction conditions utilized

KO*t*Bu, but it was shown that the butoxide was too nucleophilic and underwent rapid substitution with **A1** to form a *tert*-butyl ester. Finally, *n*-BuLi was used to deprotonate the amine prior to addition of **A1**, but these attempts yielded a wide range of products and likely involved significant decomposition of starting materials. Column chromatography of the resulting product mixture led to significant oxidation of the diphenylphosphine groups, which hindered further progress.

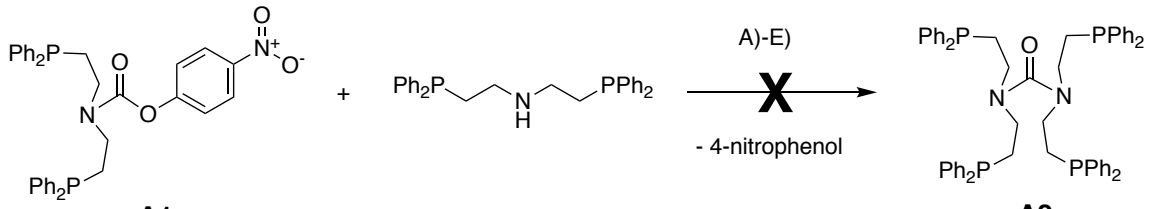


**A1** **A2**

**Scheme A.3:** Attempted synthetic route towards **A1** coupling with **PN$^{H}$P-Ph$_2$**. A) $CH_2Cl_2$, $N_2$, 24 hr., 40 °C, B) MeCN, $N_2$, $K_2CO_3$, 90 °C, 3 hr, C) THF, $N_2$, KO*t*Bu, 20 °C, 3 hr, D) THF, $N_2$, *n*-BuLi, 20 °C, 20 min, E) THF, $N_2$, n-BuLi, -108→20 °C.

**Synthesis from Carbonyl Diimidazole:** This reagent is widely used to synthesize urea and can be used in some cases to generate asymmetric urea compounds by sequential additions of amine equivalents.[7] Adding one equivalent of **PN$^{H}$P-Ph$_2$** (Scheme A.4, top) in attempts to isolate **A3** were unsuccessful due to the sensitivity of the carbonyl imidazole leaving group towards the silica gel matrix during column chromatography, and separation of products could not be achieved using basic alumina. In the attempted synthesis of **A2** (Scheme A.4, bottom), the reaction products underwent significant oxidation during column chromatography and clean isolation of the desired product could not be achieved.

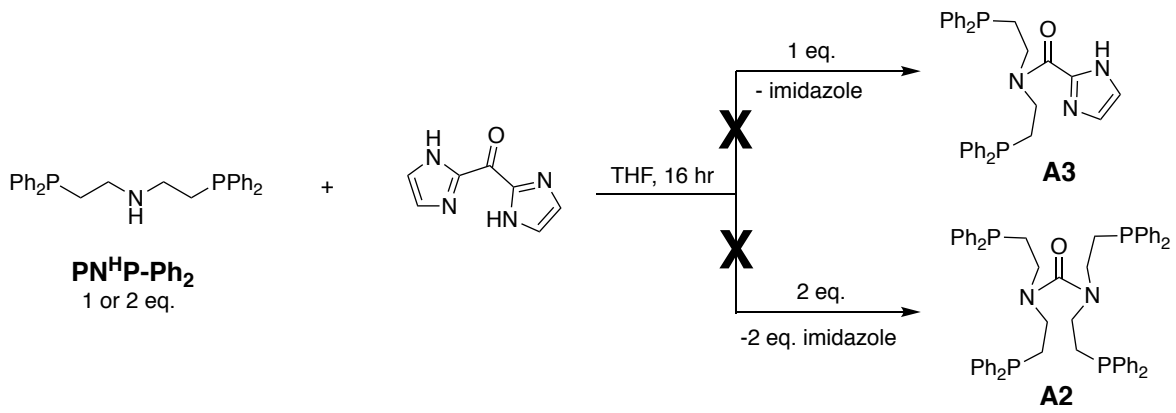


**Scheme A.4:** Proposed synthetic route to **A3** and **A2** using carbonyl diimidazole.

**Synthesis from Triphosgene:** The reaction of triphosgene with nucleophiles generates an equivalent of phosgene gas, a highly reactive electrophile that can undergo coupling with the amine groups to form the urea compounds.[8] The singly coupled **A4** intermediate (Scheme A.5) would be much more reactive than **A1**. Unfortunately, a wide distribution of products was observed by $^{31}P$ NMR. The distribution of products, as well as safety concerns regarding the use of phosgene, led us to discard this route as a viable synthetic possibility.

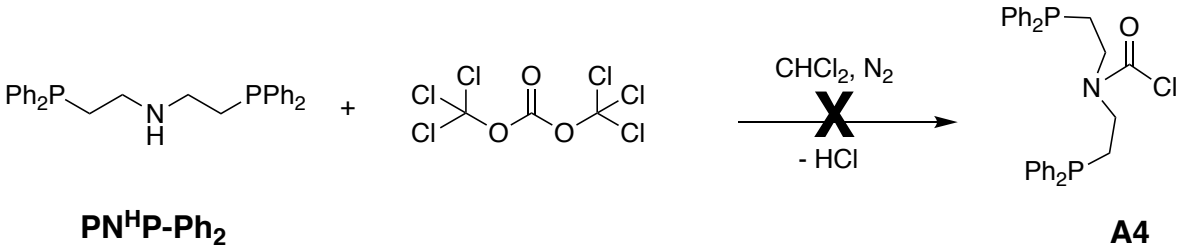


**Scheme A.5:** Proposed synthetic route to **A2** using triphosgene.

**Synthesis from Coupling Monometallic PNP Complexes:** Due to difficulties with product purification during attempts to isolate **A2**, the synthesis was carried out with the monometallic **Ni(PN$^{H}$P-Ph$_2$)(BF$_4$)$_2$** using carbonyldiimidazole as a coupling agent. The resulting bimetallic complex would subsequently be purified by crystallization. The reaction of two equivalents of Ni(PNP)(BF$_4$)$_2$ with CDI in THF resulted in no color change, but the UV-vis spectrum displayed a peak shifting 464 nm to 439 nm over the course of the reaction. Multiple crystallization attempts were carried out to purify and identify the product, but only monometallic nickel complexes were observed. Unfortunately, NMR analysis was not useful for product identification due to the paramagnetism of the nickel species, which has been observed previously in nickel pincer complexes.[9]

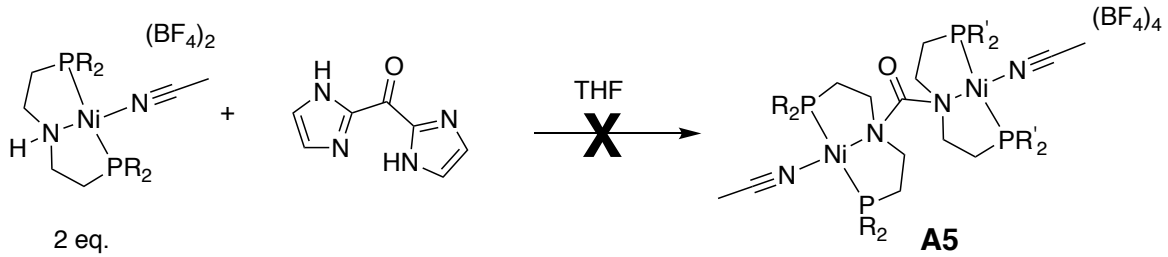


**Scheme A.6:** Proposed synthetic route to **A5** using CDI and **Ni(PN$^{H}$P-Ph$_2$)(BF$_4$)$_2$**

## A.4: Experimental Details

**General Considerations:** For synthesis containing air and moisture sensitive reagents or products, manipulations were carried out in a glovebox or using standard Schlenk techniques under an inert atmosphere of nitrogen. Unless otherwise noted, all experiments were carried out at room temperature (21-24 °C). Deuterated solvents were purchased from Cambridge Isotopes Laboratories, Inc. Reagents were purchased from commercial vendors and used without further

purification unless otherwise noted. **$PN^{H}P$-$Ph_2$** was purchased as a hydrochloride salt, and the neutral amine was prepared according to literature procedures.[10-11]

**Physical Methods:** NMR spectra were taken on a 600 MHz Bruker 600AVANCE ($^{1}H$ and $^{31}P$) at 20 °C. Electrospray ionization mass spectrometry was performed using an ESI LC-TOF Micromass LCT 3 mass spectrometer. UV-vis spectra were collected in acetonitrile solutions using an Agilent Technologies Cary 60 UV−vis.

**X-ray Crystallography.** X-ray diffraction studies were carried out at the UCI Department of Chemistry X-ray Crystallography Facility on a Bruker SMART APEX II diffractometer. Data was collected at 88 or 133 K using Mo Kα radiation (λ = 0.71073 Å). A full sphere of data was collected for each crystal structure. The APEX2[1] program suite was used to determine unit-cell parameters and to collect data. The raw frame data were processed and absorption corrected using the SAINT[2] and SADABS[3] or TWINABS [4] programs, respectively, to yield the reflection data files.

**Synthetic Procedures:**

**4-nitrophenyl bis(2-(diphenylphosphaneyl)ethyl)carbamate (A1):** 4-nitrophenylchloroformate (0.770 g, 1.18 mmol) was added to a Schlenk flask containing 15 mL degassed $CH_2Cl_2$ in an ice bath. A degassed solution of **$PN^{H}P$-$Ph_2$** was added dropwise in 15 mL $CH_2Cl_2$ via syringe. The reaction was stirred overnight under a dinitrogen atmosphere and allowed to warm to room

1. APEX2 Version 2014.11-0, Bruker AXS, Inc.; Madison, WI 2014.
2. SAINT Version 8.34a, Bruker AXS, Inc.; Madison, WI 2013.
3. Sheldrick, G. M. SADABS, Version 2014/5, Bruker AXS, Inc.; Madison, WI 2014.
4. Sheldrick, G. M. TWINABS, Version 2012/1, Bruker AXS, Inc.; Madison,

temperature. Solvent was then reduced to 15 mL $CH_2Cl_2$ *en vacuo*, and a solution of pH 6.3 phosphate buffer (10 mL, 0.5 M) was then added to the flask and stirred for 15 minutes. The mixture was transferred to a separatory funnel and organic layer removed, and then the aqueous layer was washed twice with $CH_2Cl_2$. The combined organic layers were then dried over $MgSO_4$ and solvent was removed *en vacuo* to yield a yellow oil. Column chromatography was performed with 25:75 EtAc:Hexanes to yield the purified product (360 mg, 0.590 mmol, 50.3%). $^{31}P$ NMR (600 MHz, $CDCl_3$) δ -18.52, -20.86. $^{1}H$ NMR (600 MHz, $CDCl_3$) δ 8.22 (d, 4H), 7.20-7.5 (m, 20H) 4.12 (dd, 2H), 1.26 (t, 2H).

**Ni(PN$^{H}$P-Ph$_2$)(BF$_4$)$_2$**: This compound was synthesized from a modified literature procedure.[12] A solution **PN$^{H}$P-Ph$_2$** (340 mg, .772 mmol) was prepared by dissolving the neutral amine as an oil in THF (10 mL). To this solution was added $Ni(BF_4)_2(MeCN)_6$. The resulting red solution was stirred for 16 hours and dried to a red powder. Crystals suitable for diffraction were formed by the vapor diffusion of diethyl ether into a solution of the crude product in acetonitrile. The solid state structure of this complex displays a 5-coordinate, square pyramidal Ni(II) center with both an axially bound MeCN and equatorially bound THF ligand.

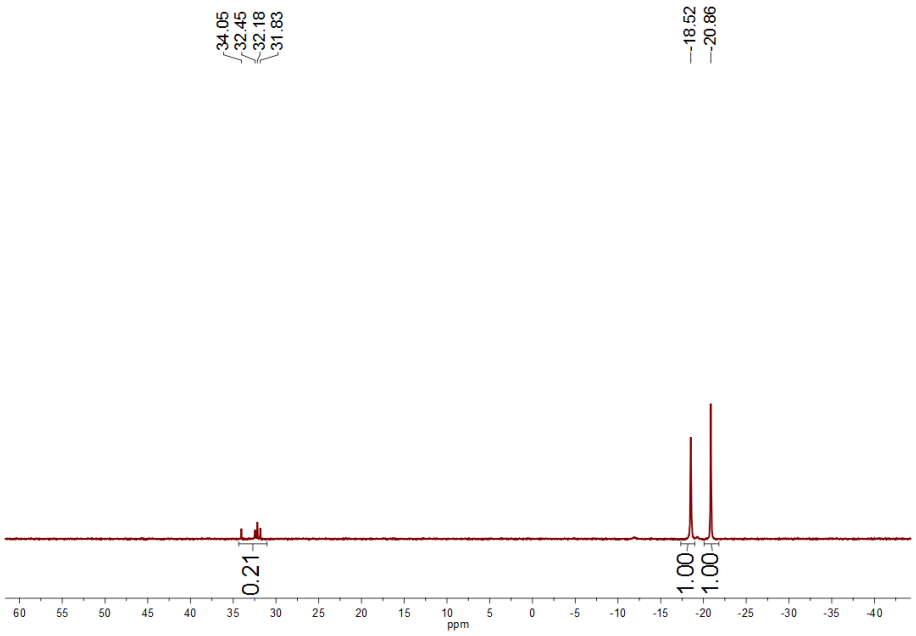


**Figure A.2:** $^{31}P$ NMR spectrum of **A1** in $CDCl_3$

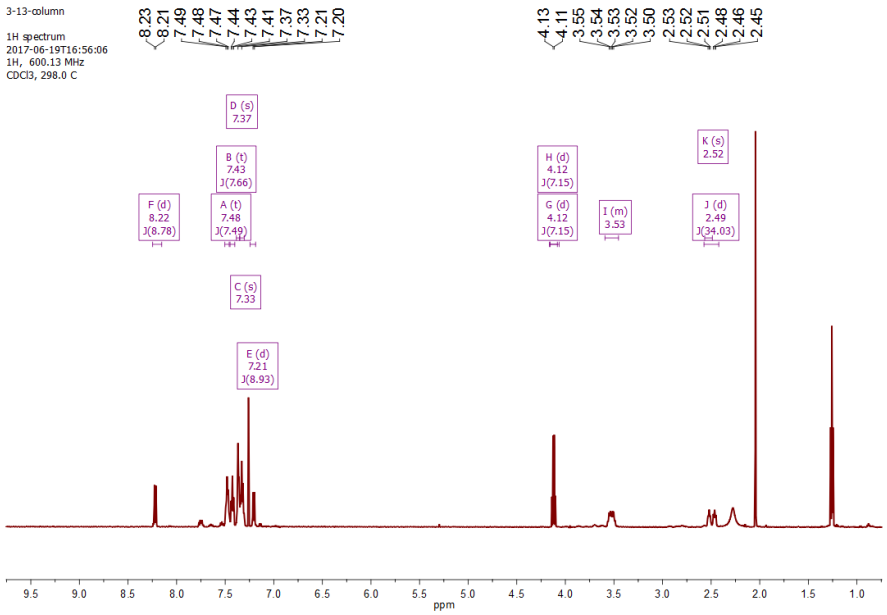


**Figure A.3:** $^{1}H$ NMR spectrum of **A1** in $CDCl_3$.

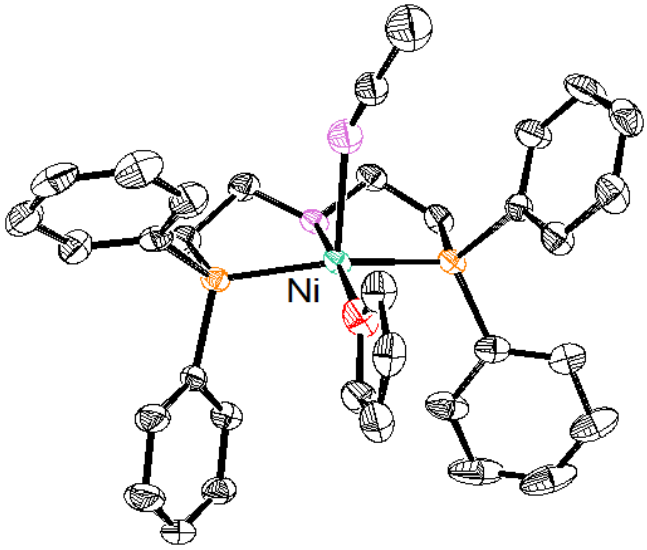


**Figure A.4:** Solid state structures of **Ni(PN$^{H}$P-Ph$_2$)(BF$_4$)$_2$**. Thermal ellipsoids are drawn to 50% probability. Hydrogen atoms and outersphere anions and solvent molecules have been omitted for clarity. The major position of the disordered acetonitrile ligand has been displayed.

## A.5: References


1. Feng, J.; Lindahl, P. A., *Biochem.* **2004,** *43* (6), 1552-1559.

2. Dobbek, H.; Svetlitchnyi, V.; Gremer, L.; Huber, R.; Meyer, O., *Science* **2001,** *293* (5533), 1281-1285.

3. Jeoung, J.-H.; Dobbek, H., *Science* **2007,** *318* (5855), 1461-1464.

4. Steffey, B. D.; Curtis, C. J.; DuBois, D. L., *Organometallics* **1995,** *14* (10), 4937-4943.

5. Raebiger, J. W.; Turner, J. W.; Noll, B. C.; Curtis, C. J.; Miedaner, A.; Cox, B.; DuBois, D. L., *Organometallics* **2006,** *25* (14), 3345-3351.

6. Turoczi, M.-C.; Simon, M.; Badea, V.; Csunderlik, C., *Molecules* **2008,** *13* (12).

7. Zheng, C.; Combs, A. P., *J. Comb. Chem.* **2002,** *4* (1), 38-43.

8. Majer, P.; Randad, R. S., *J. Org. Chem.* **1994,** *59* (7), 1937-1938.

9. Ghannam, J.; Al Assil, T.; Pankratz, T. C.; Lord, R. L.; Zeller, M.; Lee, W.-T., *Inorg. Chem.* **2018,** *57* (14), 8307-8316.

10. Nuzzo, R. G.; Haynie, S. L.; Wilson, M. E.; Whitesides, G. M., *J. Org. Chem.* **1981,** *46* (14), 2861-2867.

11. Wilson, M. E.; Nuzzo, R. G.; Whitesides, G. M., *J. Am. Chem. Soc.* **1978,** *100* (7), 2269-2270.

12. Rozenel, S. S.; Kerr, J. B.; Arnold, J., *Dalton Trans.* **2011,** *40* (40), 10397-10405.

# APPENDIX B:

# DIOXYGEN BINDING AND REDUCTION STUDIES USING HETEROBIMETALLIC COBALT SCHIFF BASE COMPLEXES WITH ENCAPSULATED CATIONS.

## B.1. Motivation and Specific Aims

Chapter 1 described how electrostatic interactions modify the reduction potentials and electronic structure of **2Co$^{II}$M$^{n+}$**. This appendix describes an attempt at characterizing the reactivity of these complexes towards dioxygen, a substrate that has been shown previously to undergo reversible binding and reduction with cobalt Schiff base compounds. The aim was to determine the influence of electrostatic fields on small molecule reactivity.

## B.2. Background

Co$^{II}$(salen) is well known as a reversible dioxygen carrier,[1-5] which prompted an investigation of how electrostatic interactions affect $O_2$ uptake. Co(salen) complexes are reactive with $O_2$ in the +2 oxidation state of cobalt, so the Co$^{III}$(salen) species were synthesized and reduced electrochemically in the presence of $O_2$ in an attempt to extrapolate kinetic information using cyclic voltammetry.

Co(salen) complexes have also been found to reduce dioxygen to hydrogen peroxide in the presence of protons.[6] Additionally, it was recently demonstrated that a linear free energy relationship exists between the Co$^{III/II}$ reduction potential and turnover frequency.[7] There is a potential opportunity to use this established relationship to compare how the **2Co$^{II}$M$^{n+}$** complexes function as catalysts relative to traditional substituted Schiff base compounds. The oxygen reduction reaction is of fundamental importance to certain fuel cell designs. Therefore it would be impactful if traditional scaling relationships (Linear free energy relationship for rate of

oxygen reduction on reduction potential) for this reaction can be broken using electrostatic interactions.

### B.3. Discussion

#### Oxidation of $2Co^{II}M^{n+}$ Complexes

In order to conduct electrochemical studies on the kinetics of $O_2$ binding, the oxidized $\mathbf{2Co^{III}M^{n+}}$ complexes were required. These octahedral $d^6$ complexes are air stable, and can subsequently be electrochemically reduced to the reactive $Co^{II}$ compounds in $O_2$ saturated solutions. Initial chemical oxidations were carried out with *p*-toluenesulfonic acid for its literature precedent as a $Co^{II}$ Schiff base oxidant.[8] However, this reagent (along with $Ag(BF_4)$, which was used in subsequent attempts) was not sufficiently oxidizing to cleanly convert the $Co^{II}$ starting material, likely caused by the positive shift in reduction potentials of the $\mathbf{2Co^{III}M^{n+}}$ complexes due to the presence of the encapsulated cations. Nitrosonium tetrafluoroborate is a sufficiently strong oxidant for $Co^{II}$ oxidation,[9] but UV-Vis spectroscopy indicated that $NO^+$ coordination was persistent (Figure B.2). Thianthrenium oxidants were eventually found to be an adequate reagent for the $Co^{II}$ oxidation, and led to the successful isolation of $\mathbf{2Co^{III}Sr(OTf)_3}$ and $\mathbf{2Co^{III}Ba(OTf)_3}$.

#### Electrochemical $O_2$ Binding Studies

Electrochemical reduction of the $\mathbf{2Co^{III}M^{n+}}$ in the presence of dioxygen was used to attempt to resolve the rate of $O_2$ binding to the $Co^{II}$ species. Unfortunately, the slow kinetics of the $Co^{III/II}$ couple at the electrode was a significant problem. At scan rates sufficiently slow to garner kinetic information on $O_2$ binding, the peak potentials of the $Co^{III/II}$ were separated by approximately 500 mV (Figure B.1). Additional complications were encountered in finding am

internal reference for potential measurements, all of which interfered with the broad window required to observe the $Co^{III/II}$ redox event of the analyte complexes.

**Electrochemical $O_2$ Reduction to $H_2O_2$**

Cyclic voltammetry was used to gain a preliminary understanding of how the CoM(18-crown-6-salen) complexes behave under the reported catalytic conditions. The studies were conducted in 1 mM solutions of analyte in MeOH with 100 mM $TBAPF_6$. The $Co^{III/II}$ redox couple exhibits slow electron transfer kinetics (Figure B.3, black trace). After the addition of $O_2$, there is immediate marked increase in current indicative of catalysis, possibly $O_2$ reduction enabled by methanol as a proton source. The addition of acetic acid (AcOH) shows that catalysis is greatly enhanced by the addition of a stronger acid source (Figure 7, maroon trace). Unfortunately, internal references were irreversible , and potentials had to be referenced to an $Ag/Ag^+$ pseudoreference. Consequently, potentials in these experiments cannot be accurately measured.

**Discussion of Non-ideal Electrochemical Behavior**

The sluggish behavior of the $Co^{III/II}$ couple was a significant issue in the electrochemical studies described above. Additional problems, such as the inability to find a suitable internal reference, created further complications in determining accurate measurements through electrochemical means. During the course of this work, a publication by Mayer and Stahl[7] noted similar issues while investigating electrocatalytic $O_2$ reduction with Co(salen) complexes. In this work, catalytic turnover frequencies were determined using chemical oxidation and monitored by UV-Vis spectroscopy and $O_2$ binding was quantified using a Clark electrode.

## B.4: Experimental Details

### General Considerations:

For synthesis containing air and moisture sensitive reagents or products, manipulations were carried out in a glovebox or using standard Schlenk techniques under an inert atmosphere of nitrogen. Unless otherwise noted, all experiments were carried out at room temperature (21-24 °C). All solvents used were degassed by sparging with argon and dried by passing through columns of neutral alumina or molecular sieves. Reagents were purchased from commercial vendors and used without further purification unless otherwise noted. The synthesis of all **2Co$^{II}$M$^{n+}$** compounds were carried out as described in Chapter 1 of this work. Thianthrenium oxidants were prepared according to literature procedures.[10]

### Physical Methods:

### Synthetic Procedures

**Attempted Oxidation of Co$^{II}$(OMe-Salen) with p-Toluenesulfonic acid:** Adopted from a similar literature procedure to generate a Co$^{III}$Cl(salen) species.[8] Co$^{II}$(OMe-Salen) (59 mg, .152 mmol) was dissolved in $CH_2Cl_2$ to form a red suspension. PTSA-$H_2O$ (29 mg, .152 mmol) was then added as a solid, and the reaction mixture was stirred for one hour. The brown reaction mixture did not match the reported green product due to insufficient oxidation.

**Attempted Oxidation of Co$^{II}$(OMe-Salen) with Ag(BF$_4$):** Co(OMe-Salen) (34.5 mg, .089 mmol) was dissolved in MeCN, and Ag($BF_4$) (10.2 mg, .107 mmol, 1.2 eq.) was added as a solid in one portion. The solution was stirred for three hours, and solvent was removed *en vacuo* to yield a brown solid. Crystallization attempts to purify the product returned only starting material from the incomplete conversion to the Co$^{III}$ product.

**Attempted Oxidation of $Co^{II}$(OMe-Salen) and $Co^{II}M$(18-crown-6-salen) complexes with $NOBF_4$:** The Co(salen) complex was dissolved in MeCN and cooled to -35°C. To this solution, $NOBF_4$ was titrated into the reaction dropwise. At one equivalent, a brown solution formed similar to that observed with the $Ag(BF_4)$ oxidation. After several more drops were added to the solution, a deep green color formed in solution.

**Oxidation of $Co^{II}$(OMe-Salen) and $Co^{II}M$(18-crown-6-salen) complexes with thianthrenium salts ($Th^+BF_4$ or $Th^+SbF_6$):** The $Co^{II}$(OMe-Salen) or $Co^{II}M$(18-crown-6-salen) starting material was dissolved in MeCN, and cooled to -35°C. $Th(SbF_6)$ was then added as a MeCN solution in one portion, and the inky purple solution slowly turned green over approximately ten minutes. Removal of solvent left a green solid that could be recrystallized from vapor diffusion of diethyl ether into acetonitrile, yielding crystals suitable for X-ray diffraction.

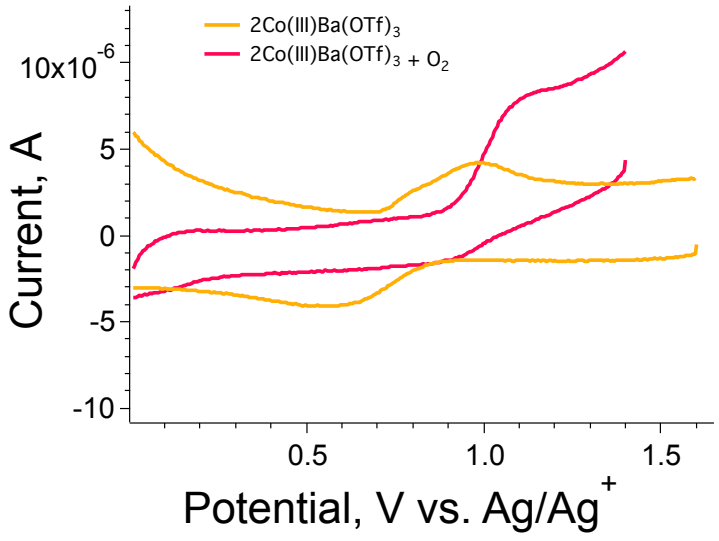


**Figure B.1:** Cyclic Voltammetry of **$2Co^{III}Ba(OTf)_3$** under an $N_2$ atmosphere (orange), followed by exposure to $O_2$ (red). CVs are referenced to $Ag/Ag^+$ psuedoreference due to incompatibilities with internal standards.

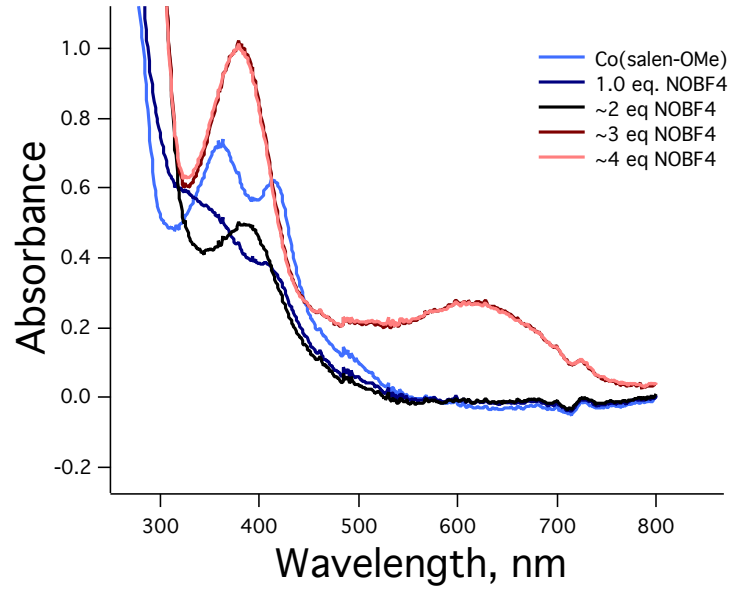


**Figure B.2:** UV-Vis spectrum of the titration of $NO(BF_4)$ into a solution of Co(salen-OMe) in acetonitrile.

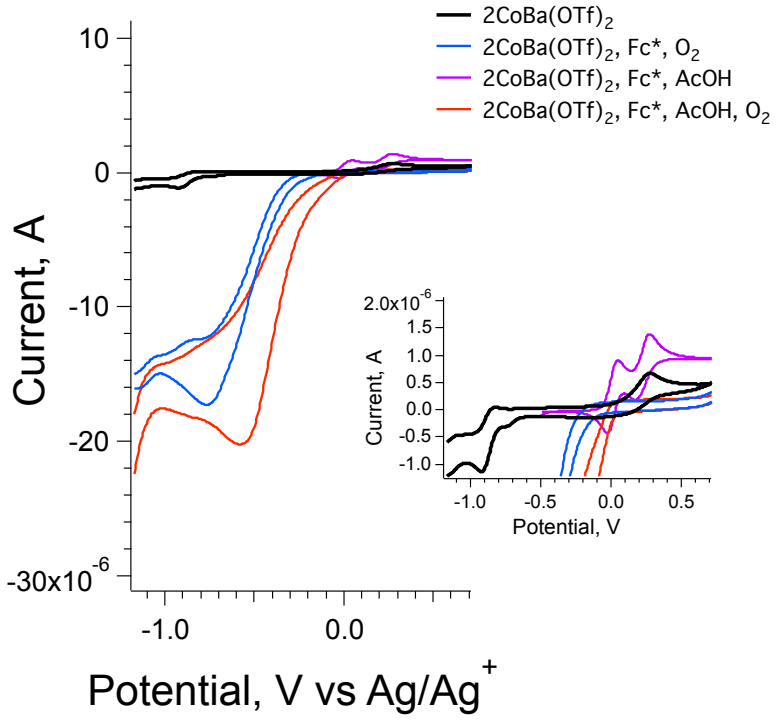


**Figure B.3:** Cyclic voltammetry data from $O_2$ reduction studies taken at 10 mV/s in methanol, $Fc^*$ = decamethylferrocene. Subwindow shows magnified current for clarity.

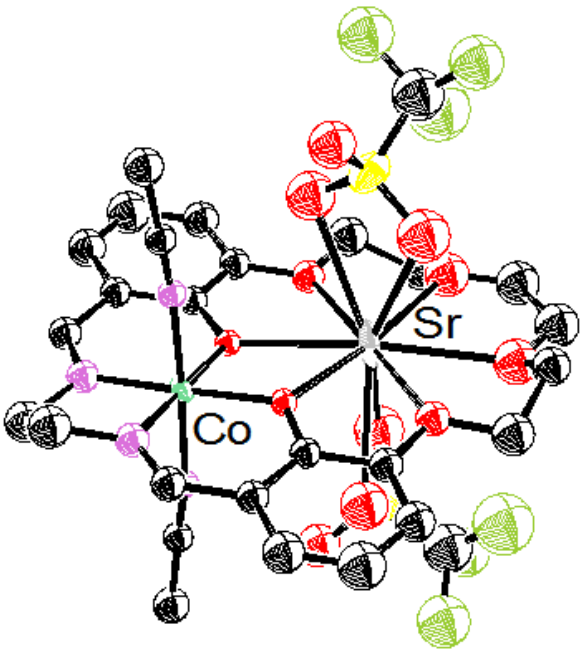


**Figure B.4:** Unfinalized solid state structure of **2Co$^{III}$Sr(OTf)$_3$**. An outersphere triflate has been removed for clarity. One of two disordered positions of two carbon atoms in the crown ether ring have been shown.

## B.5: References

1. Ortiz, B.; Park, S.-M., *Bull. Korean Chem. Soc.* **2000,** *21* (4), 405-411.

2. Jones, R. D.; Summerville, D. A.; Basolo, F., *Chem. Rev* **1979,** *79* (2), 139-179.

3. Basolo, F.; Hoffman, B. M.; Ibers, J. A., *Acc. Chem. Res.* **1975,** *8* (11), 384-392.

4. Calvin, M.; Bailes, R. H.; Wilmarth, W. K., *J. Am. Chem. Soc.* **1946,** *68* (11), 2254-2256.

5. McLendon, G.; Martell, A. E., *Coord. Chem. Rev.* **1976,** *19* (1), 1-39.

6. Jäger, E.-G.; Knaudt, J.; Rudolph, M.; Rost, M., *Chemische Berichte* **1996,** *129* (9), 1041-1047.

7. Wang, Y.-H.; Pegis, M. L.; Mayer, J. M.; Stahl, S. S., *J. Am. Chem. Soc.* **2017,** *139* (46), 16458-16461.

8. Ford, D. D.; Nielsen, L. P. C.; Zuend, S. J.; Musgrave, C. B.; Jacobsen, E. N., *J. Am. Chem. Soc.* **2013,** *135* (41), 15595-15608.

9. Connelly, N. G.; Geiger, W. E., *Chem. Rev.* **1996,** *96* (2), 877-910.

10. Boduszek, B.; Shine, H. J., *J. Org. Chem.* **1988,** *53* (21), 5142-5143.